XFEL.EU TR-2011-002

## CONCEPTUAL DESIGN REPORT

# X-Ray Optics and Beam Transport

April 2011

*H. Sinn, J. Gaudin, L. Samoylova, A. Trapp, and G. Galasso*
*for X-ray Optics and Beam Transport (WP73)*
*at the European XFEL*

**European X-Ray Free-Electron Laser Facility GmbH**
Albert-Einstein-Ring 19
22761 Hamburg
Germany

# Contents

# 1 Introduction

The task of the X-ray beam transport systems at the European XFEL is to deliver X-ray radiation from undulators to experiments. Located in underground tunnels, the up to 1 km long X-ray transport systems have to separate the X-ray free-electron laser (FEL) beam from its high energetic radiation background, bring it to a usable size, and—for some of the experiments—limit its bandwidth by monochromators. A general layout of the photon beam systems of the European XFEL is shown in Figure 1. Acronyms for buildings and experiments are explained in Appendix F, “Abbreviations and acronyms”.

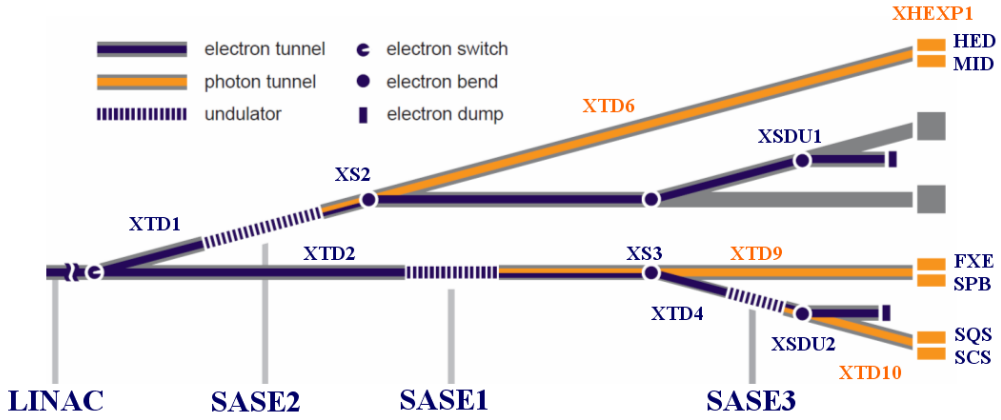


***Figure 1:*** *Layout of photon beam systems at the European XFEL. The X-ray beam transport systems are located in the parts of the facility marked in orange.*

X-ray laser beams consist of extremely intense pulses of femtosecond duration. A single FEL pulse can melt the surface of copper or tungsten in the upstream end of the beam transport systems within a few picoseconds. Therefore, all parts of the X-ray optics that can be exposed directly to the FEL beam have to be made out of lightweight and high-melting materials like diamond and boron carbide. Exceptions may be metal-coated X-ray mirrors that can work under grazing incidence geometry in the experiment stations or—under restricted operational conditions—in the beam transport system.

The capability that sets the European XFEL facility apart from all other hard X-ray lasers is the megahertz repetition rate of FEL pulses in trains of up to 2 700 pulses. For the X-ray optics, this means up to several 10 kW heat load per $mm^2$ on some optical elements for the duration of a pulse train. The average heat load is, on the other hand, comparable or lower than that at the third generation synchrotron sources. For some X-ray optics, like crystal monochromators or X-ray lenses, this leads to a maximum number of allowed pulses per pulse train before the monochromators gets detuned or a lens gets too hot and thermal damage might occur. For mirrors, time-resolved finite element calculations are used to predict the change of optical properties during a pulse train.

X-ray laser beams are highly coherent and—similar to light from optical lasers—the beam can interfere with itself over the entire cross section. This leads to an extreme sensitivity to profile errors of mirrors and cut-off effects from apertures. These effects were simulated and optimized by wavefront propagation simulations.

This document is organized as follows: In the first three chapters, the requirements, conceptual design, and expected performance of each beamline are presented in an overview. Then the *SASE beam properties* that are important to X-ray transport are discussed in detail because the performance and operational limits of beamline components depend crucially on assumptions made here.

In Chapter 6, “Beamline components”, the concepts and limitations of crucial parts of the beam transport systems are explained, like the mirror-based beam offset and distribution system, monochromators, and focusing elements.

Wavefront simulations for selected cases are presented in Chapter 7 and criteria for surface profile quality of mirrors are given.

Finally, in Chapter 8 some concluding remarks are given on the conceptual design presented here also in connections with possible future operation modes of the facility, for example seeding at the hard X-ray undulators or the after-burner concept with circularly polarized X-rays for SASE3.

The appendices provide supplemental information on how damage calculations and FEA simulations were performed, the suppression of higher harmonics by the beamline optics, and the expected long-term stability due to vibrations and ground diffusion effects.

# 2 Requirements for X-ray transport

Requirements for the photon beam transport systems were discussed in several workshops (organized by the European XFEL in 2008-2010) and then defined by the responsible experiment scientists and scientific directors [1]. Table 1 shows a summary of the most important key parameters.

***Table 1:*** *Requirements to the photon beam transport systems*

| | SASE 1 | | SASE2 | | SASE3 | | |
|---|---|---|---|---|---|---|---|
| **Experiment** | SPB | FXE | MID | HED | SQS | SQS2 | SCS |
| **FEL photon energies [keV]** | 3–16 | 3–20 | 5–20 | 3–16 | 0.28–3 | 0.28–3 | 0.28–3 |
| **HHR and SR [keV]** | — | — | 25–36+ | 25–36 | — | — | — |
| **Pink beam (no monochromator)** | Yes | | | | | | |
| **Bandwidth mono 1 [dE/E]** | $10^{-4}$ | $10^{-4}$ | $10^{-4}$ | $<10^{-4}$ | opt. | — | $10^{-4}$ |
| **Bandwidth mono 2 [dE/E]** | — | $10^{-5}$ | $10^{-5}$ | — | — | — | — |
| **Beam size [µm]** | 0.1–10 | 1–100 | 1–100 | 1–100 | 1–100 | Open | 1–100 |

Apart from the requirements shown in the table, all beam transport systems should transmit the maximum possible number of photons per pulse and the maximum number of pulses per pulse train. Preservation of wavefronts should be achieved by employing the best available mirrors and by clear apertures of 4 σ or larger.

Since the beam transport systems are located in underground tunnels, all hardware has to perform with extreme reliability, since access during operation will be very limited. Also, changes of beam conditions that require re-adjustments (like major changes of energy or switching of experiments)

should be able to be performed quickly by either an operator or user by using suitable macros.

Moreover, safe operation, resistance to damage and heat load, and radiation safety have to be fulfilled.

These generic requirements are summarized as follows:

- Maximum possible transmission for individual pulses and number of pulses within a pulse train.
- Minimum possible distortion of wavefronts by beamline optics. For SASE1 and SASE2, 4σ or larger apertures should be achieved above 5 keV; for SASE3, above 0.45 keV.
- High reliability of all mechanical and electrical components. Extensive and possibly redundant monitoring of the system status (motor encoders, temperatures, bending radius of mirrors, and so on).
- Safe operation with regards to single-pulse damage and heat-load damage during the pulse trains. If damage cannot be excluded by the design, administrative limitations on bunch charge or pulse numbers per train for certain operation conditions must be implemented into the equipment protection and control system.
- Fast change in between experiments (few minutes to less than one hour for more advanced changes).
- Reliable and fast change of photon energy tuning of the mirror system (few minutes to less than 30 minutes).
- Operational by staff or users with suitable macros.
- Stability of beam positions and transmitted energy at monochromators.
- Radiation protection has to be fulfilled: With closed shutters in the shaft buildings XS2 and XS3, safe working conditions in the photon tunnels XTD6 and XTD9 should be achieved. High-energy Bremsstrahlung has to be blocked from entering the experiment hall by a suitable beam offset and beam stoppers. Closing shutters in front of the individual stations in the experiment hall should permit safe working in the experiment stations while other experiments can take beam.

# 3 Conceptual design

The photon beamlines of the European XFEL span up to 1 km distance between FEL source point and the experiments. This length enables a beam distribution system based on total reflecting mirrors with a lateral separation of experiments in the experiment hall. Furthermore, the expansion of the X-ray beam due to its natural divergence leads to the feasibility of crystal-based monochromators at the end of the photon tunnels.

Conversely, relatively large beam sizes on the order of mm pose a challenge for the X-ray optical design: The nearly diffraction limited X-ray beams change their divergences proportional to their wavelength, leading to variation of spot sizes with energy of about a factor of 10 in all three SASE beamlines. With an expected technological limit in mirror length of 800 mm, this leads to the requirement of variable incidence angles at the offset mirrors. By positioning the offset mirrors as close as feasible to the undulators, the need for re-tuning of incidence angles is minimized to 2–4 positions over the energy working range of a beamline while transmitting almost the full beam (> 4σ of largest expected beam size).

For the beam distribution mirrors, tuning of the incidence angle is not practical and therefore the beam has to be focused onto these mirrors by dynamical bending of the second offset mirror. For the hard X-ray beamlines, the distance between offset and distribution mirror can be chosen such that bending the distribution mirror is not required to deliver the natural beam size at the end of the photon tunnels. At the soft X-ray beamline, a focusing of the second offset mirror is used to reduce the footprint on the grating of the plane grating monochromator (PGM).

All mirror reflections are in the horizontal plane. The main reason for this is that the mounting of the 800 mm long mirrors and also the metrology are more feasible in this orientation. Because focusing by the second offset mirror is used to reduce the footprint on the distribution mirrors and the grating

monochromators, all these mirror deflections have to be in the same plane. This leads at all beamlines to a vertical beam size that corresponds to the natural divergence and to a beam that will be almost free of wavefront distortions in the vertical plane. In the horizontal plane, the beam size can be tuned by controlling the bending radii of offset or distribution mirrors.

The hard X-ray monochromators are placed at the end of the photon tunnels to minimize the heat-load effect during pulse trains. Even then, a full pulse train with maximum pulse energy will be impossible to transmit. However, for 250 pC bunch charge and below, pulse trains of up to 1000 pulses can be transported through the monochromators.

For the soft X-ray monochromator, a PGM design was chosen in order to have a maximum transmission over a wide energy range. However, for some wavelengths, pulse energies above 2 mJ could lead to damage on optical elements of this monochromator. Therefore, operational limits will have to be implemented on this device.

Focusing at the hard X-ray beamlines is foreseen after the monochromator, either with 0.8 m long KB mirrors in front of the sample or with a two-stage focusing concept based on compound refractive lenses (CRLs). For pink-beam operation of the hard X-ray beamlines, the beam can also be collimated with CRLs in front of the offset mirrors. This would facilitate in particular the sub-micron focusing in the vertical direction at the experiments.

In the following the concepts for each beamline are explained in more detail.

# SASE1

The main components of the beam transport are shown in Figure 2. The source point is assumed to be in the middle of the third-to-last undulator module. The separation of electron and photon beam is about 150 m behind the source point. Following that is a diagnostics section with intensity monitors (XGMDs) and two beam position monitors (XBPMs) that will allow shot-to-shot analysis of the beam coming from the undulator (see also the

sequence of components in Figure 3). An adjustable beam aperture (SRA) and a solid attenuator will allow a first conditioning of the beam. A CRL assembly at 230 m can be used to pre-focus the beam in pink-beam mode to the experiment stations. The K monochromator is designed to analyse spontaneous radiation of the undulator during commissioning. At 270 m distance follows the 800 mm long first offset mirror. This mirror will absorb most of the spontaneous radiation power passing through the upstream apertures. The average heat load of less than 10 W will be removed by water cooling. The second offset mirror absorbs only a heat load smaller than 3 W and will be water cooled and bendable with radii larger than 50 km. This adjustment capability is required to correct for static heat load bending of the first mirror and to control the beam size after the offset mirrors. The beam after the offset mirror can be sent directly to the centre experiment station. To deflect the beam to one of the two side stations, a distribution mirror at 370 m (or 380 m, respectively) has to be moved into the beam path. Its position is defined by the critical angle for the maximum desired photon energy and the lateral space available at the tunnel exit. If the second offset mirror focuses to 430 m, the deflection mirror will reflect the full cross section of the beam. It turns out that, in this geometry, a flat distribution mirror will produce equal horizontal and vertical beam sizes at the experimental area. At 850 m, 50 m before the experiment hall, a cryogenically cooled silicon (111) monochromator is placed. A higher resolution monochromator could be positioned behind this monochromator. All focusing should be done after this monochromator; otherwise, the number of transmitted pulses will decrease. Optionally, a diamond monochromator could be used instead, which would provide better energy resolution than the silicon (111) monochromator by about a factor of two.

Be CRLs directly after the monochromator are an interesting focusing option for spot sizes of around 50 microns at the sample location or for pre-focusing for a nano-focusing optics. At the experiment, micro-or nano-focusing can be achieved by CRL or KB mirror optic, as illustrated in the Chapter 6, “Beamline components”.

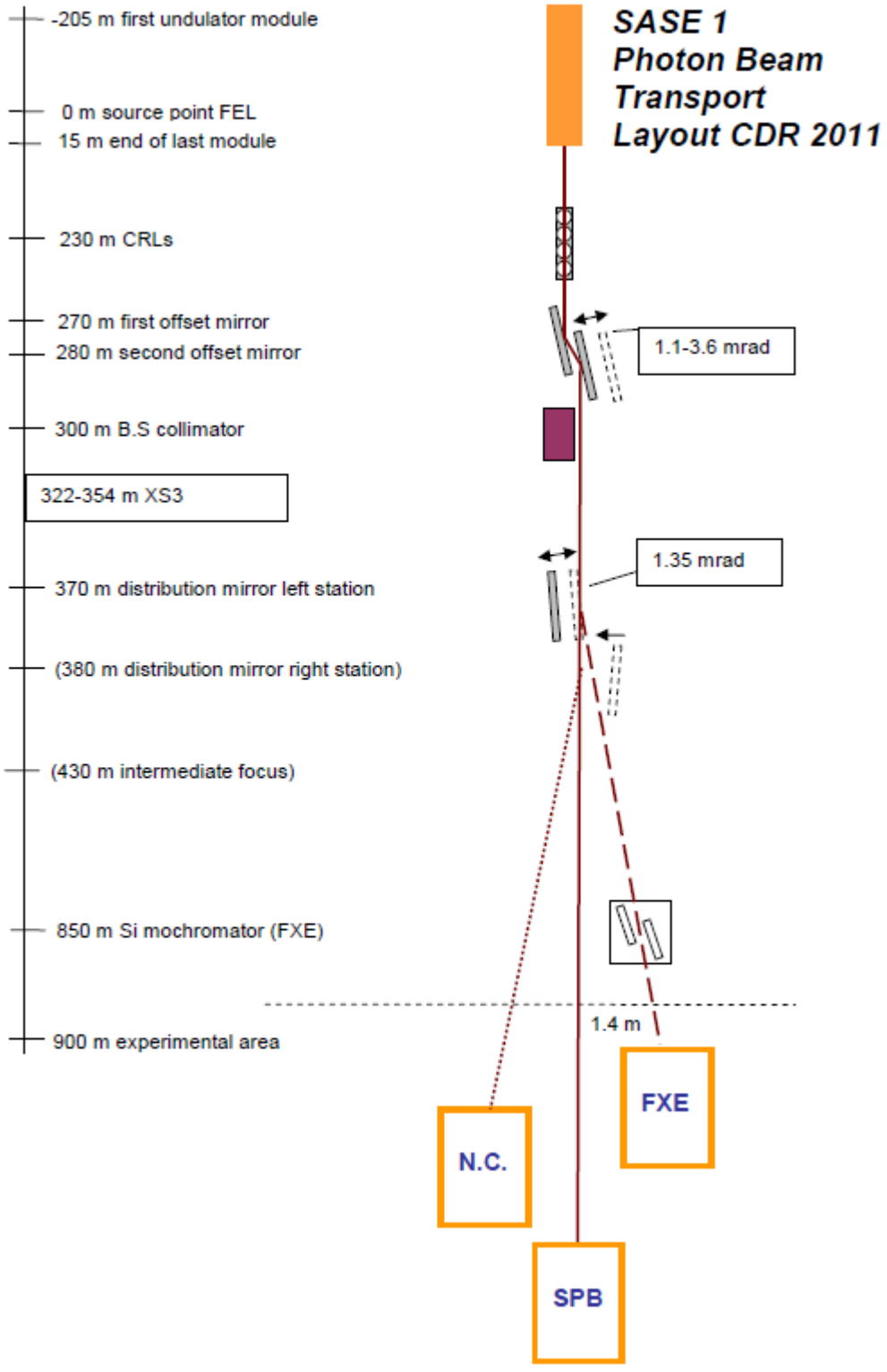


***Figure 2:*** *Conceptual design of the SASE1 beam transport system*

The sequence of components installed for the photon beam transport system SASE1 is shown in Figure 3. Diagnostics tools are shown in green.

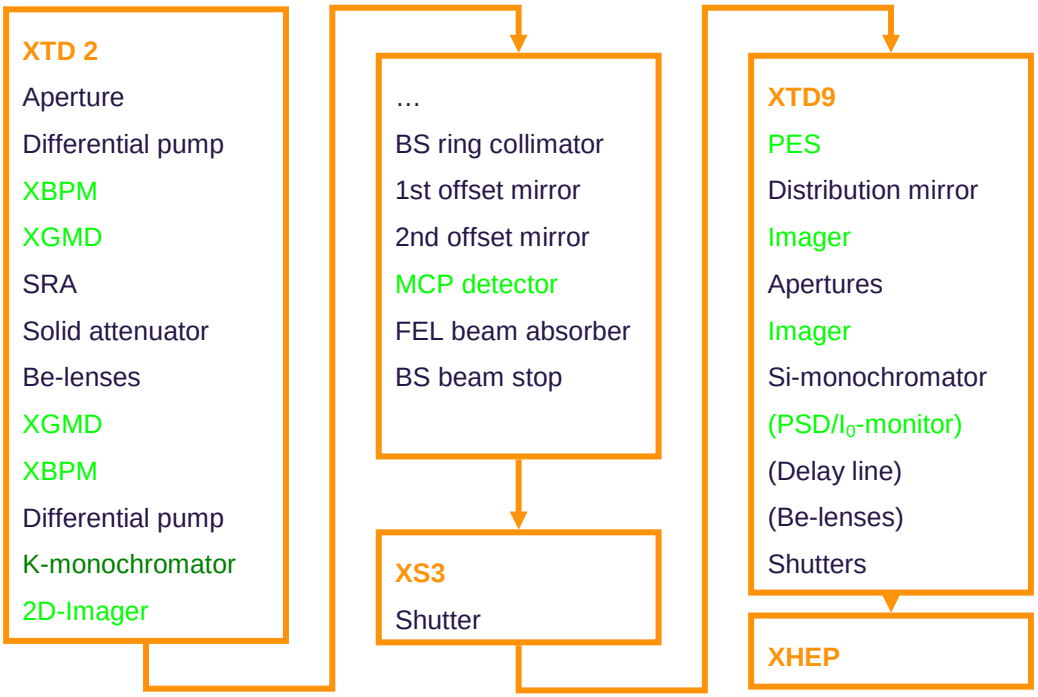


***Figure 3:*** *X-ray components in the SASE1 beam transport system. The components in green will be provided by the X-ray Photon Diagnostics group, WP74. Components shown in brackets indicate placeholders for options. Acronyms are explained at the end of this document.*

# SASE2

The concept of the SASE2 beam transport is analogous to SASE1 and is shown in Figure 4.

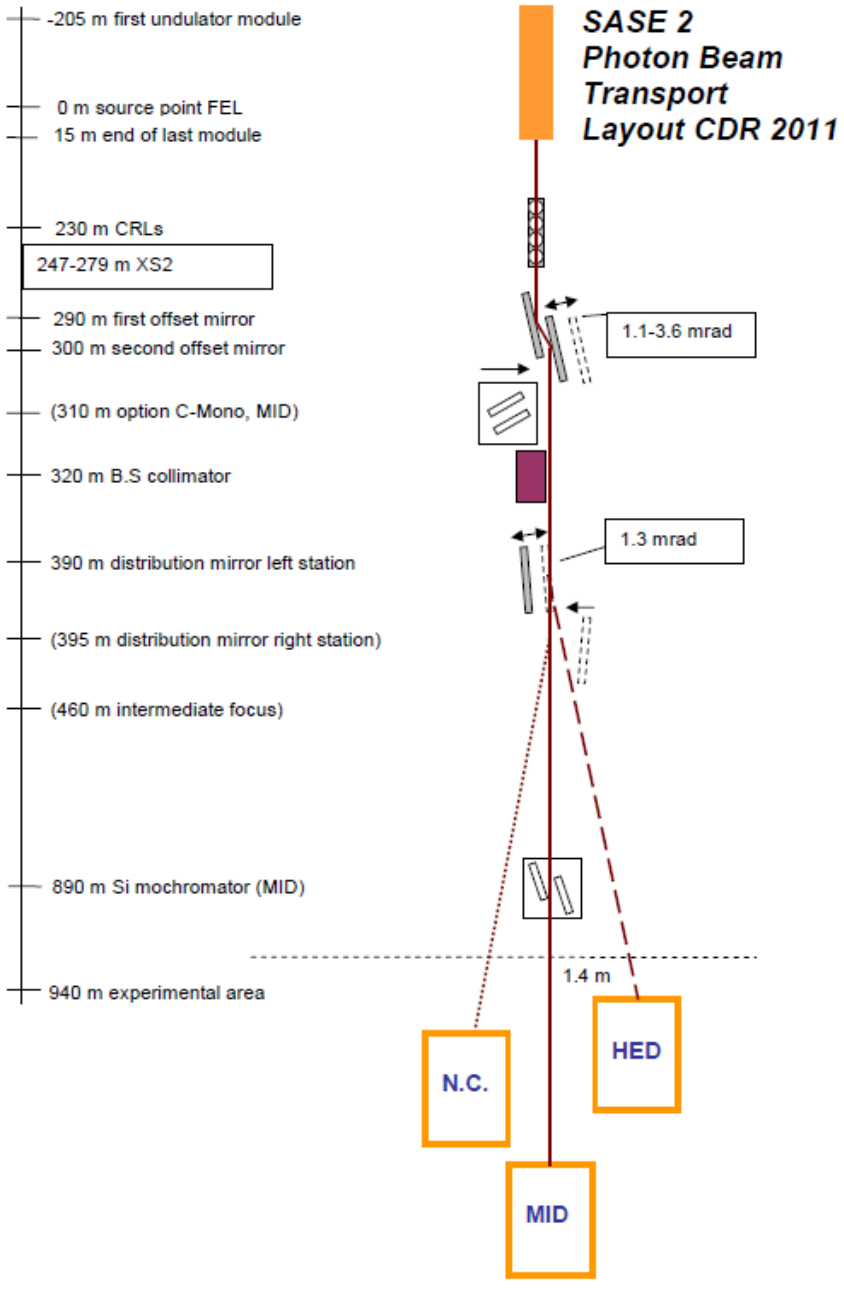


***Figure 4:*** *Conceptual design of the SASE2 beam transport system*

The main differences from SASE1 come from the different location of the shaft building and the length of the photon tunnel XTD6: Due to the earlier

location of the shaft building, the offset mirrors can be placed in the photon tunnel without compromising the beam quality. In contrast to SASE1, the direct undulator beam will therefore enter the photon tunnel. The longer XTD6 tunnel enables slightly higher cut-off energies at the branch beamlines because the distribution mirror angle can be reduced from 1.35 mrad to 1.30 mrad. As an additional option, a diamond Laue monochromator can be placed in front of the BS beam stop to bypass high-energy X-rays of 80 keV to the MID experiment.

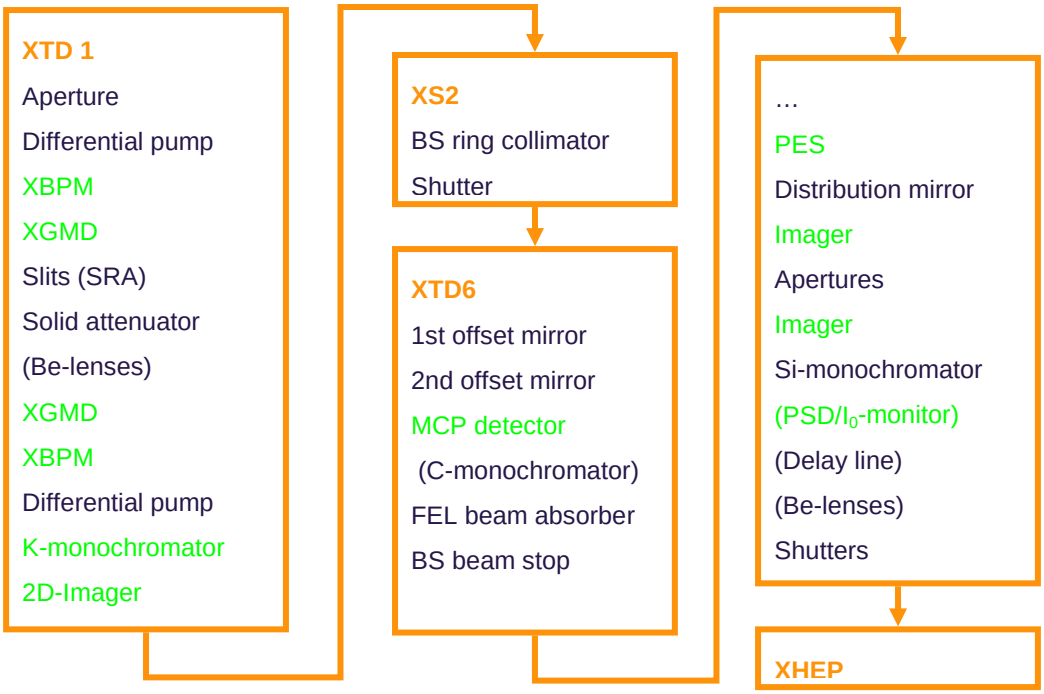


***Figure 5:*** *X-ray components in the SASE2 beam transport system*

# SASE3

The schematic of the SASE3 beam transport is shown in Figure 6 and its components are listed in Figure 7.

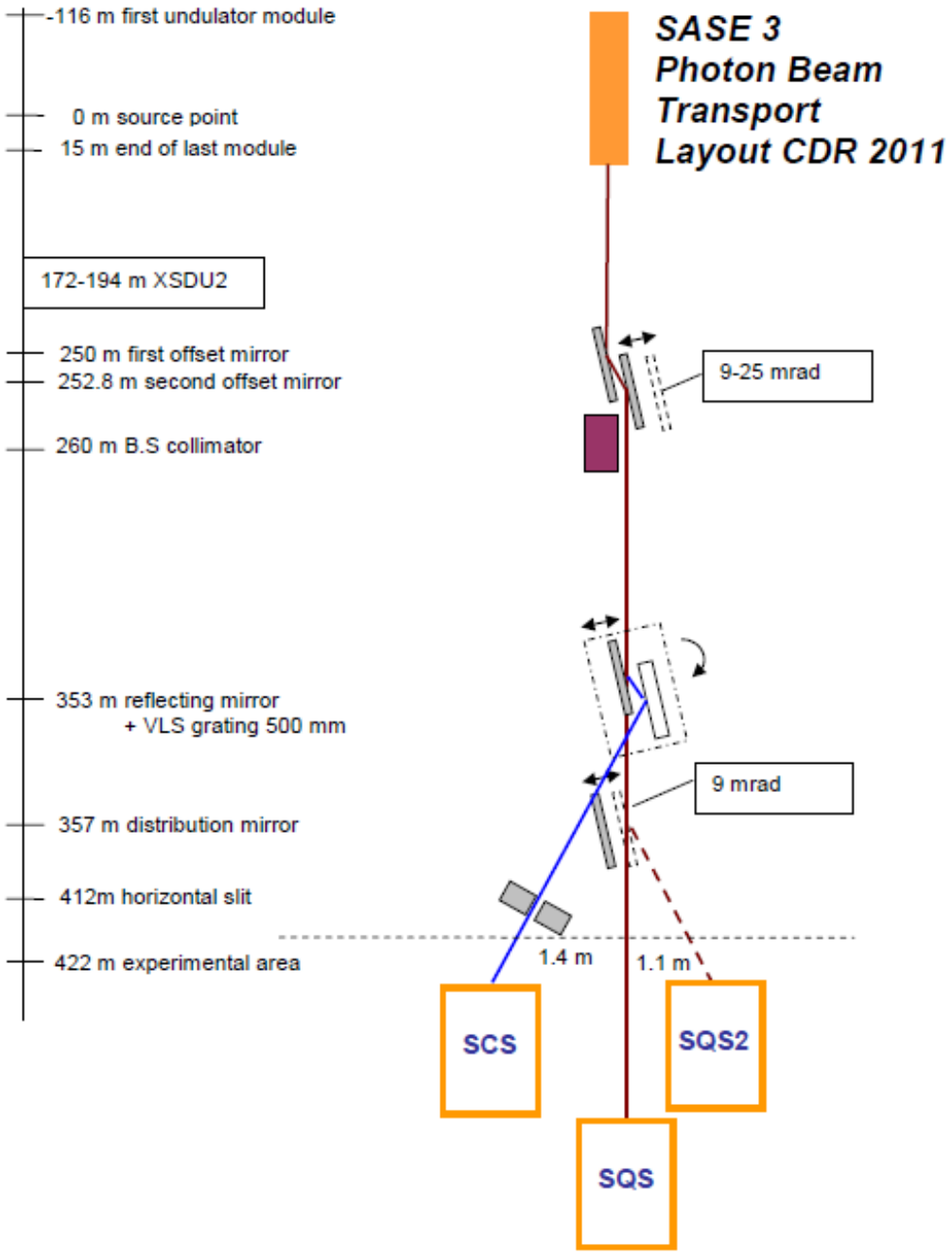


***Figure 6:*** *Conceptual design of the SASE3 beam transport system*

The upstream diagnostics and beam conditioning are similar to SASE1 and SASE2. However, instead of a solid attenuator, a gas attenuator system will be installed. The double mirror system (each mirror is 800 mm long) for beam offset can be adjusted between 9–25 mrad incidence angle. The second offset mirror will provide adjustable bending between 7.5 km and flat. The beam from the offset mirrors can be passed directly to the SQS station. A distribution mirror at 357 m can be used to deflect this pink beam to the station SQS2. The PGM optical layout consists of a reflecting plane mirror, a 460 mm long grating at 353 m, and the exit slit at 412 m. When operating in monochromatic mode, the second offset mirror focuses the beam onto the exit slit. The grating is placed in the converging beam such that the footprint on the grating satisfies the 4σ condition for the beam aperture. To compensate refocusing effects from the grating, the line spacing along the beam footprint needs to vary (VLS-type grating). The exit angle of the PGM is 1.2° in order to increase the reflectivity on the reflecting mirror. To cover the entire energy range, two gratings with different line spacings will be used. The resolution of the PGM is expected to be $10^{-4}$ or better, depending on the feasible grating length. The monochromator will be sensitive to single-shot damage. The maximum tolerable energy per pulse will be limited here to about 2 mJ at certain energy ranges.

Optionally, the PGM could be operated with 200 mm long gratings, if 500 mm gratings are not available. In this case, one would increase the monochromator exit angle to about 1.6° to reduce damage and increase the efficiency. Still, the shorter grating would lead to poorer resolution and almost half-tolerable energy per pulse.

With the distribution mirror placed directly after the PGM grating, it could be optionally used to reflect the monochromatic beam into the SQS station. In that case, a second exit slit for the SQS station would be required. The feasibility of this option will be studied in the technical design phase. The positioning of the distribution mirror after the monochromator limits the separation between SQS and SQS2 to 1.1 m in the current design. The performance of the monochromatic beam at SQS would be less than at SCS due to the additional optical element and possibly different angles at the

reflecting mirror, in particular if the shorter grating will be employed. Details of the PGM design and possible optimisations are provided in Chapter 6, “Beamline components”.

In contrast to the hard X-ray beamlines, all beamline transport components at SASE3 are physically in the same building as the undulator system. The electron-beam dump hall XSDU2 has no access from above ground and provides also no separation between the undulator tunnel XTD4 and the photon tunnel XTD10.

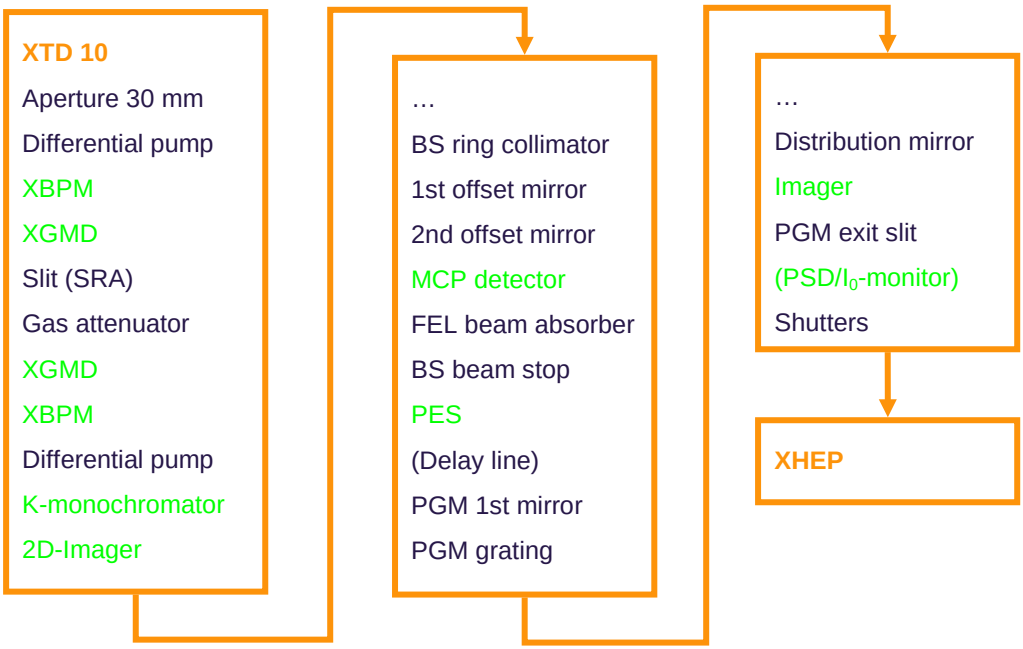


***Figure 7:*** *X-ray components in the SASE3 beam transport system*

# 4 Expected performance

This chapter provides an overview of the expected performance of the beam transport systems. More detailed analyses of specific beamline optical components are provided in the Chapter 6, “Beamline components”. The values given here were calculated with the angles and distances above from Chapter 3, “Conceptual design”, and are based on several assumptions about technical improvements over the current state of the art, in particular on mirrors and gratings.

The focusing schemes in the experiment hall and, to some extent, the selection of monochromators are part of the design choices of the scientific instrument. More information on these optics concepts can be found in the CDRs for the scientific instruments. Here we discuss focusing only in connection with the baseline-design components of the photon beam transport systems.

# SASE1

***Table 2:*** *SASE1 beam transport performance parameters*

| **SASE1** | **SPB** | **FXE** |
|---|---|---|
| Lowest transmitted photon energy | 3 keV limited by source | |
| ... with ≥ 4σ cut-off at 20 pC operation, 800 mm mirrors | 3.1 keV | |
| Lowest energy cut-off of offset mirrors | 7.5 keV | |
| Highest transmitted energy (carbon coated mirrors) | 24 keV | 20 keV |
| Mirror length relative to beam size at critical angle at 7.5 keV | 7.8 σ | |
| ... at 20 keV | 6.1 σ | |
| Tunability $E_{max}/E_{min}$ with $E_{max}$= 7.5 keV | 2.4 | |
| ... with $E_{max}$= 20 keV | 1.75 | |
| Pulses transmitted in pink beam operation | Not limited by optics | |
| Reflectivity of mirrors combined at 3 keV, 1nm roughness | 0.96 | 0.95 |
| ... at 20 keV, 1.1 mrad offset mirror, 1.35 mrad distr. mirror | 0.90 | 0.83 |
| Pulses transmitted in mono beam with 250 pC and 12 keV | —* | >1000 |
| ... 500 pC | —* | 500 |
| ... 1 nC | —* | 80 |

* A monochromator for the SPB instrument is currently considered as an option and would have the same performance as the FXE monochromator.

***Table 3:*** *SASE1 beam sizes, divergences, and angles in the experiment hall*

| Photon-energy [keV] | $FWHM_{upper}$ [mm] | $FWHM_{lower}$ [mm] | Divergence [µrad]* | FXE horizontal divergence [µrad]* | Horizontal beam angle [µrad]** |
|---|---|---|---|---|---|
| 3 | 5.57 | 3.10 | 6.18 | 11.7 | 94 |
| 5 | 3.80 | 2.01 | 4.22 | 8.07 | 51 |
| 8 | 2.67 | 1.34 | 2.96 | 5.64 | 24 |
| 10 | 2.26 | 1.11 | 2.51 | 4.77 | 14 |
| 12 | 1.97 | 0.95 | 2.19 | 4.16 | 7.3 |
| 15 | 1.66 | 0.79 | 1.85 | 3.52 | 0 |
| 18 | 1.45 | 0.67 | 1.61 | 3.08 | 0 |
| 20 | 1.34 | 0.62 | 1.49 | 2.83 | 0 |
| 24 | 1.17 | 0.53 | 1.30 | — | 0 |

* Divergences are calculated as FWHM for the lowest bunch charge.

** Horizontal beam angle based on 25 mm minimum offset at the BS beam stop and 4σ beam coverage where possible.

**Horizontal focusing with the offset mirror:** With the second horizontal offset mirror, it is in principle also possible to focus into the experiment hall. The horizontal source size in the undulator would then appear 2.2 times geometrically magnified. With a combined slope error of the offset mirror of e.g. 50 nrad rms, the horizontal focused spot size could be possibly as small as 300 µm. For FXE, bending of the second offset mirror is utilized to match the focus to the distribution mirror. However, a similar focusing effect can be achieved by bending the distribution mirror.

**Focusing with upstream CRLs:** The CRLs in front of the offset mirrors should also be able to image the source in a similar way to the experiment hall, however in two dimensions. In this case, the damage of downstream beamline components has to be closely monitored, which might lead to limitations in permissible pulses per pulse trains. Further limitations come from the chromaticity, the reduced transmission at low energies, and the heat-load limitations of the CRLs themselves in the 1nC operation mode.

# SASE2

***Table 4:*** *SASE2 beam transport performance parameters*

| SASE2 | MID | HED |
|---|---|---|
| Lowest transmitted photon energy | 3 keV limited by source | |
| ... with ≥ 4σ cut-off at 20 pC operation, 800 mm mirrors | 3.4keV | |
| Lowest energy cut-off of offset mirrors | 7.5 keV | |
| Highest transmitted energy (carbon coated mirrors) | 24 keV | 20.7 keV |
| Highest transmitted energy (Pd coated mirrors) | 50 keV | 42 keV |
| Highest transmitted energy (Pt coated mirrors) | 67 keV | 57 keV |
| Mirror length relative to beam size at critical angle at 7.5 keV | 7.3 σ | |
| ... at 20 keV | 5.7σ | |
| Tunability $E_{max}/E_{min}$ with $E_{max}$= 7.5 keV | 2.2 | |
| ... with $E_{max}$= 20 keV | 1.60 | |
| Pulses transmitted in pink beam operation | Not limited by optics | |
| Reflectivity of mirrors combined at 3 keV, 1nm roughness | 0.96 | 0.95 |
| ... at 20 keV, 1.1 mrad offset mirrors, 1.3 mrad distr. mirror | 0.90 | 0.84 |
| Pulses transmitted in mono beam with 250 pC and 12 keV | >1000 | —* |
| ... 500 pC | 500 | —* |
| ... 1 nC | 80 | —* |

* A monochromator for the HED instrument is currently considered as an option and would have the same performance as the MID monochromator.

***Table 5:*** *SASE2 beam parameters in the experiment hall*

| Photon-energy [keV] | $FWHM_{upper}$ [mm] | $FWHM_{lower}$ [mm] | Divergence [µrad]* | HED horizontal divergence [µrad]* | Horizontal beam angle [µrad]** |
|---|---|---|---|---|---|
| 3 | 5.81 | 3.23 | 6.18 | 11.9 | 101 |
| 5 | 3.96 | 2.09 | 4.21 | 8.17 | 56.3 |
| 8 | 2.78 | 1.40 | 2.96 | 5.74 | 28.0 |
| 10 | 2.35 | 1.16 | 2.51 | 4.85 | 17.6 |
| 12 | 2.05 | 1.00 | 2.18 | 4.23 | 10.4 |
| 15 | 1.73 | 0.82 | 1.84 | 3.58 | 2.79 |
| 18 | 1.51 | 0.71 | 1.61 | 3.12 | 0 |
| 20 | 1.40 | 0.65 | 1.49 | 2.89 | 0 |
| 24 | 1.22 | 0.55 | 1.30 | 2.51 | 0 |

* Divergences are calculated as FWHM for the lowest bunch charge.

** Horizontal beam angle based on 25 mm minimum offset at the BS beam stop and 4σ beam coverage where possible.

**Focusing with the offset mirror and upstream Be-CRLs:** The situation is analogous to SASE1. However, if the distribution mirror is used with the metal coating, damage on this mirror due to the focused beam could occur earlier than at SASE1.

# SASE3

***Table 6:*** *SASE3 beam transport performance parameters*

| SASE3 | SCS | SQS | SQS2 |
|---|---|---|---|
| Lowest transmitted photon energy | 0.26 keV limited by source | | |
| ... with ≥ 4σ cut-off at 20 pC operation, 800 mm mirrors | 203 eV | | |
| Lowest energy cut-off of offset mirrors | 1 keV | | |
| Highest transmitted energy (carbon coated mirrors) | 3 keV | | |
| Mirror length relative to beam size at critical angle at 1 keV | 13.2 σ | | |
| ... at 3 keV | 10.8 σ | | |
| Tunability $E_{max}/E_{min}$ with $E_{max}$= 1 keV | 4.9 | | |
| ... with $E_{max}$= 3 keV | 3.7 | | |
| Pulses transmitted in pink beam operation | Not limited by optics | | |
| Max. acceptable energy per pulse (30 meV/C-atom) | ≈ 2 mJ | ≈ 10 mJ | |
| Reflectivity of mirrors combined at 0.26 keV 1nm roughness, offset mirrors at 21 mrad (4σ) | 0.84(*) | 0.93 | 0.91 |
| ... at 0.5 keV, offset mirrors at 12.7 mrad (4σ) | 0.55 | 0.76 | 0.70 |
| ... at 1keV, offset mirrors at 9 mrad (4σ) | 0.74 | 0.87 | 0.81 |
| ... at 2 keV | 0.69 | 0.86 | 0.80 |
| ... at 3 keV | 0.65 | 0.78 | 0.69 |

(*) For the SCS monochromatic beamlines, the zero order reflectivity of the grating was used. The grating efficiency in the first order is shown in the “Soft X-ray monochromator” section and is in the order of 1–4%.

***Table 7:*** *SASE3 beam parameters in the experiment hall*

| Photon-energy [keV] | $FWHM_{upper}$ [mm] | $FWHM_{lower}$ [mm] | Divergence [µrad]* | SCS horizontal divergence [µrad]* | Horizontal beam angle [µrad]** |
|---|---|---|---|---|---|
| 0.26 | 16.3 | 11.6 | 38.7 | 61.5 | 271 |
| 0.5 | 10.0 | 6.66 | 23.7 | 37.6 | 86 |
| 0.8 | 7.03 | 4.47 | 16.6 | 26.4 | 0 |
| 1.0 | 5.95 | 3.70 | 14.1 | 22.4 | 0 |
| 1.5 | 4.39 | 2.61 | 10.4 | 16.5 | 0 |
| 1.7 | 4.00 | 2.35 | 9.47 | 15.0 | 0 |
| 2.0 | 3.53 | 2.05 | 8.38 | 13.3 | 0 |
| 2.5 | 3.00 | 1.70 | 7.09 | 11.2 | 0 |
| 3.0 | 2.61 | 1.45 | 6.19 | 9.82 | 0 |

* Divergences are calculated as FWHM for the lowest bunch charge.

** Horizontal beam angle based on 35 mm minimum offset at the BS beam stop and 4σ beam coverage where possible.

# 5 SASE beam properties

A comprehensive set of FEL beam properties for different operation conditions was calculated recently by M. Yurkov and colleagues [2]. An important parameter for the beam transport is the divergence of the radiation. The blue circles in Figure 8 represent calculations for SASE1 and SASE2 undulators (40 mm period) and the red circles for SASE3 (68 mm period). Calculations were done for different bunch charges (20pC to 1nC) and accelerator energies (10.5, 14, and 17.5 GeV).

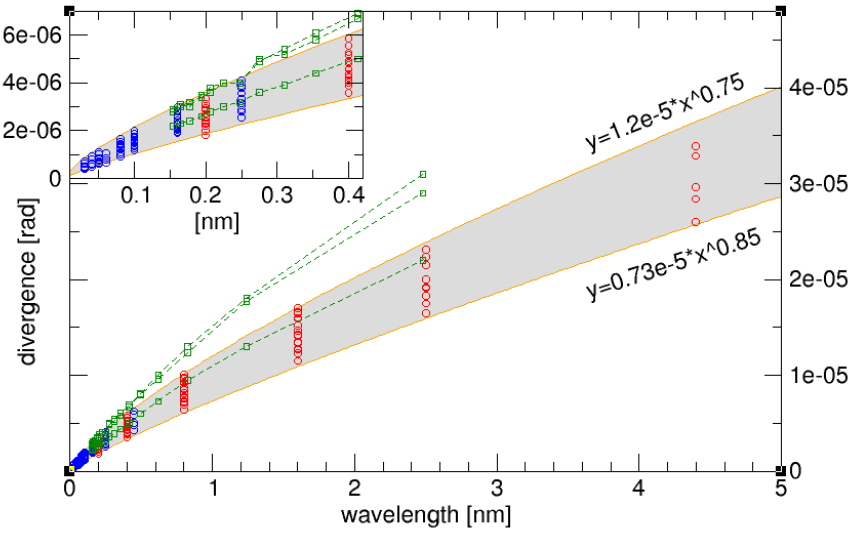


***Figure 8:*** *Calculated divergences (FWHM) for 10.5–17.5 GeV and 20pC–1nC. Blue circles are calculations for SASE1 and SASE2, red circles for SASE3. The green dots are calculations for the LCLS (from the LCLS website) for 20, 40, and 250 pC bunch charge.*

The highest divergences at a particular wavelength correspond to the lowest charge mode (20 pC) and the highest accelerator energy (17.5 GeV); the lowest points correspond to 1 nC and 10.5 GeV. For optimization of beamline components, it is convenient to describe the calculated data by empirical fit

functions. The calculated divergences fall between the two boundaries (upper and lower; orange lines in Figure 8):

$$\delta\theta_{fwhm}\left[rad\right]_{upper} = 1.2\times10^{-5}\times\lambda^{0.75}\left[nm\right];$$

$$\delta\theta_{fwhm}\left[rad\right]_{lower} = 0.73\times10^{-5}\times\lambda^{0.85}\left[nm\right]$$

In dependence of photon energy, the upper equations become:

$$\delta\theta_{fwhm}\left[\mu rad\right]_{upper} = \frac{14.1}{E^{0.75}\left[keV\right]}; \qquad \delta\theta_{fwhm}\left[\mu rad\right]_{lower} = \frac{8.76}{E^{0.85}\left[keV\right]} \tag{1}$$

The corresponding pulse energies per pulse at saturation are shown in Figure 9.

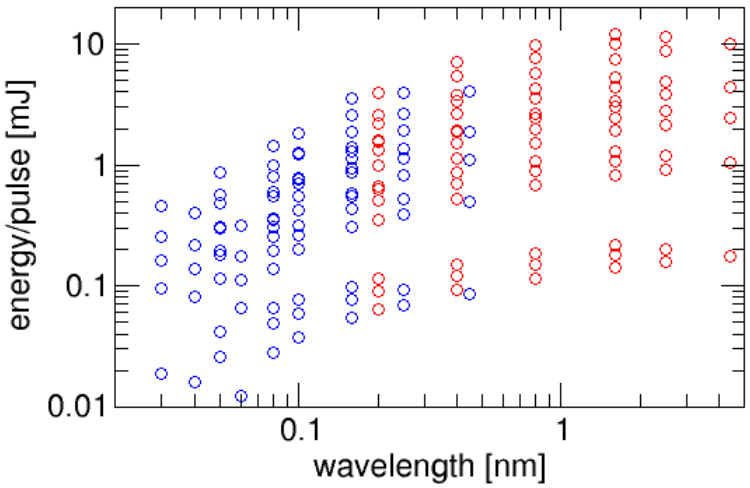


***Figure 9:*** *Energy per pulse for different operation conditions. Red circles are for the SASE3 undulator, blue circles for the SASE1 and SASE2 undulators.*

The photon beam source size in the undulator is shown in Figure 10.

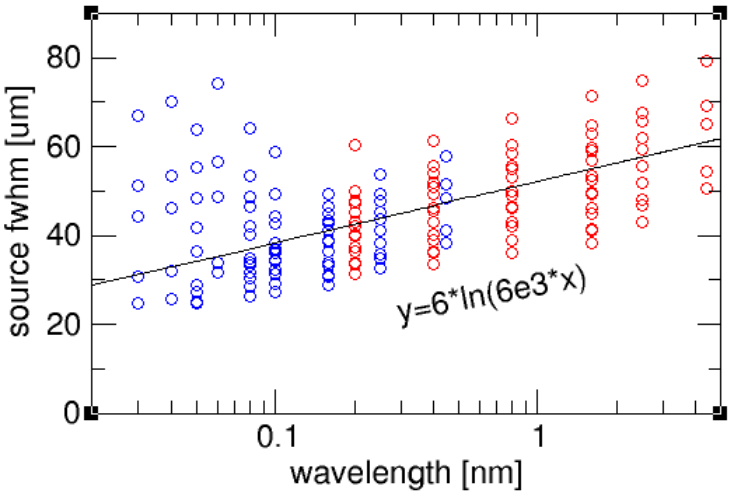


***Figure 10:*** *Size of the photon source in the undulator. Red and blue circles as in Figure 9.*

Variations are large, in particular at wavelengths below 1 Angstrom. An average trend through the source sizes (black line) can be described as:

$$s_{fwhm}[\mu m] = 6\ln(6000\,\lambda[nm]) = 6\ln(7.4e3/E[keV]) \quad (2)$$

The time duration of the photon pulses is in good approximation linear to the electron bunch charge (Figure 11).

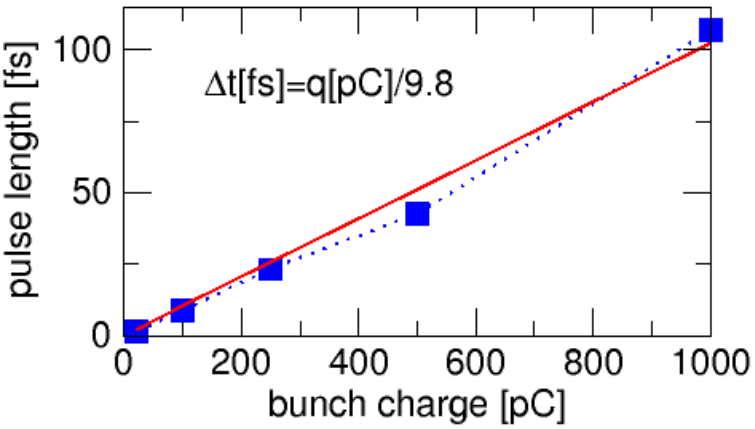


***Figure 11:*** *Pulse length in dependence of bunch charges*

## Hard X-ray range

For a more detailed analysis of the performance of the hard X-ray monochromators, the divergence and pulse power of a subset of the data (14 GeV, SASE1, and SASE2) was fitted in dependence of the bunch charge. Results are shown in Figure 12 and Figure 13**.**

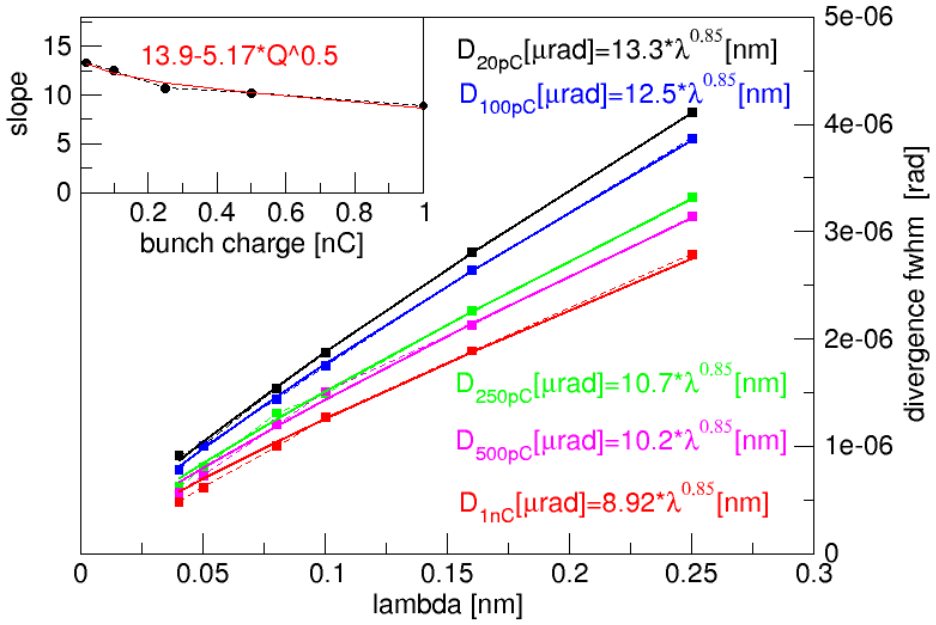


***Figure 12:*** *Photon beam divergence for hard X-rays in dependence on photon wavelength and bunch charge*

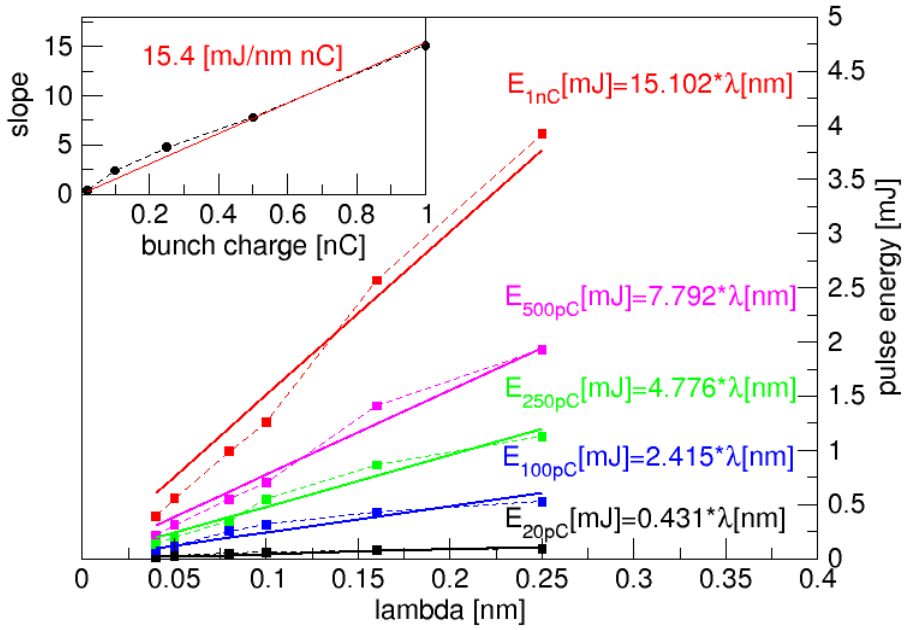


***Figure 13:*** *Pulse energies in the hard X-ray range in dependence on photon wavelength and bunch charge*

The parameterized fit curves for pulse energies are described by:

$$E_{pulse}[mJ] = 15.4 \times Q[nC] \times \lambda[nm]$$

or

$$E_{pulse}[mJ] = \frac{19\ Q[nC]}{E_{photon}[keV]} \tag{3}$$

for $E_{photon}$ = 5 keV .. 40 keV, with $Q$ being the bunch charge.

The divergences can then described by:

$$\delta\theta_{fwhm}[\mu rad] = \left(13.9 - 5.17\sqrt{Q[nC]}\right)\lambda^{0.85}$$

or

$$\delta\theta_{fwhm}[\mu rad] = \frac{\left(17.2 - 6.4\sqrt{Q[nC]}\right)}{E[keV]^{085}} \tag{4}$$

One important question is how reliable the predictions on the beam parameters will be. During the commission phase of the LCLS, observed divergences were more than twice as large as previous theoretical predictions. This was in part due to the smaller bunch slice emittance that could be achieved because of the excellent performance of the electron gun and the electron beam transport in the accelerator. The smaller source point in the undulator section leads for the diffraction-limited FEL beam to a larger divergence. Also, a non-perfect alignment of the electron beam trajectory can lead to increased photon beam divergence. These effects have to be taken into account in the dimensioning of beam optics in particular for the lengths and grazing angles of the mirrors.

Figure 14 shows measurements of beam divergences that were taken during the commissioning phase of LCLS in 2009 [3]. The brown circles are averages over many beam size measurements taken at the LCLS ST0 station and in the FEE under different conditions. The lowest divergence of 2 µrad at 8.3 keV was obtained at the lowest charge mode (20pC) after careful alignment of the electron beam trajectory. With higher bunch charges observed divergences were in the 3–4 µrad range.

Since at 8.3 keV photon energy the accelerator energy of LCLS is comparable to the European XFEL in the 14 GeV operation mode, one can expect similar divergences. The grey area shows to simulation of European XFEL beam divergences discussed above. It turns out that the upper boundary of calculated divergences at 20 pC comes close to measured divergences at higher bunch charges. For the calculation of beamline apertures, the upper boundary of the calculated divergences was considered for all bunch charges. For damage calculations, the 1nC mode is the most relevant case and therefore the lower divergences have been assumed as a “worst case” scenario. For calculations of transmissions through hard X-ray monochromators, different bunch charges, with their corresponding pulse energies and divergences, were assumed.

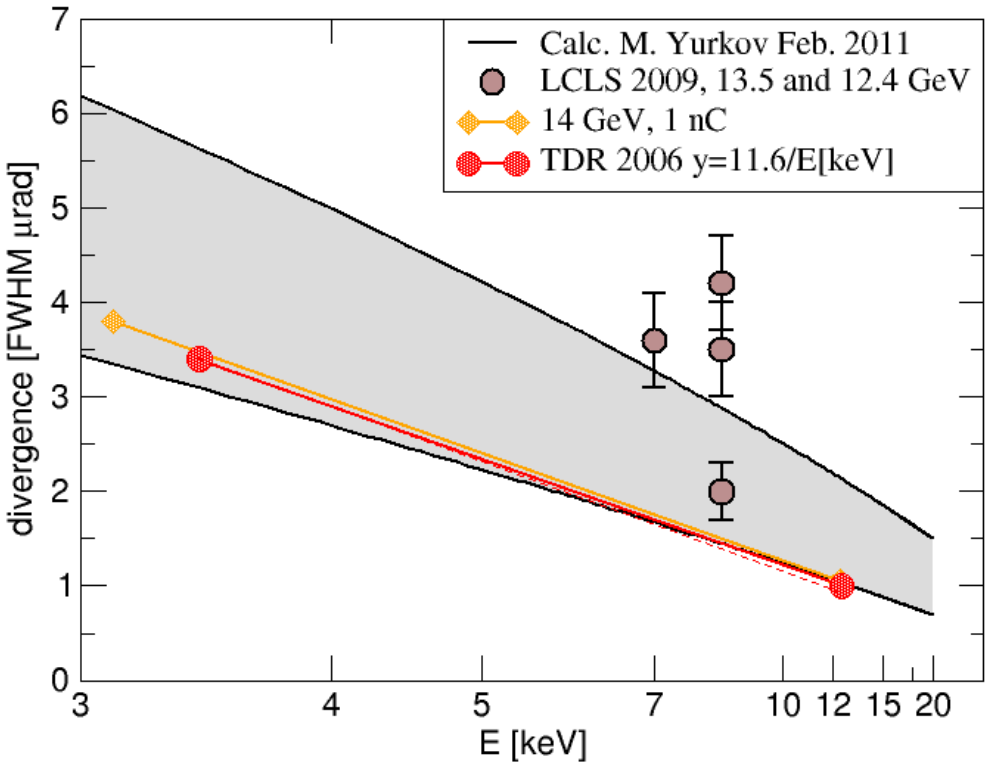


***Figure 14:*** *Comparison of calculations for European XFEL (grey area) with measurements (brown dots) from LCLS. The red and the orange line are calculations with a maximum bunch charge of 1 nC.*

# 6 Beamline components

## Bremsstrahlung collimator

The purpose of the Bremsstrahlung (BS) collimator is to absorb the high-energy spontaneous radiation generated by undulators during normal operation and Bremsstrahlung that could occur if the electron beam would hit accidentally onto a target in the undulator section. For the beam distribution concept, it is crucial to minimize the smallest offset at the offset mirrors. The reason is that all necessary motions when changing the incidence angles scale with the minimum required offset. For example, a 50 mm required minimum offset at SASE1 and SASE2 leads to (3.6 mrad – 1.1 mrad) / 1.1 mrad × 50 mm = 114 mm lateral motion and for SASE3 to (25 mrad – 9 mrad) / 9mrad × 50mm = 88 mm lateral beam motion of the second offset mirror. These relatively large translations lead to difficulties in the mechanical design for the mirror chambers and also for the downstream diagnostics, which has to follow this beam motion. Therefore, in order to minimize the required offset, a two-step collimator design is chosen, where the beam aperture is cut before the offset mirrors by a *ring collimator* to the minimum diameter required for the SASE beam at all energies. After the mirrors, an offset slightly larger than this diameter is introduced at the *beam stop*, so that there is no direct line of sight between the source and the experiment area. Both parts of this collimator consist of about 30 cm thick tungsten to absorb sufficiently the highest possible X-ray energies.

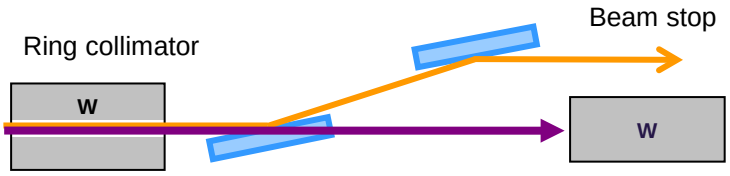


***Figure 15:*** *Bremsstrahlung collimator*

The Bremsstrahlung collimator dimensions are deduced from the maximum expected beam sizes (SASE 1 and SASE2) with a safety factor of 1.5, or the maximum aperture of the offset mirrors (SASE3). For beam size calculations, equation (1), the higher beam divergences was used.

In Table 8, the minimum offset is estimated to be 17 mm at SASE1 and SASE2 and 27 mm at SASE3. In this CDR, we assume minimum offset values of 25 mm and 35 mm for hard and soft X-ray beamlines. These values have to be confirmed by calculations of the radiation safety group. Currently, the minimum required offset is 50 mm for all beamlines according to the TDR2006 [4]. For this document, all optics considerations are also valid for a 50 mm offset, however, horizontal beam angles in Table 3, Table 5, and Table 7 would have to be enlarged in proportion to the beam offset.

***Table 8:*** *Calculation of ring collimator apertures and beam offsets*

| | SASE 1 | SASE 2 | SASE 3 |
|---|---|---|---|
| Distance of ring collimator to source point | 260 m | 280 m | 240 m |
| Lowest photon energy considered | 3 keV | 3 keV | 0.50 keV |
| Beam divergence δθ (FWHM) | 6.2 µrad | 6.2 µrad | 23.7 µrad |
| FWHM of largest beam considered | 1.61 mm | 1.73 mm | 5.69 mm |
| Largest beam diameter 6 σ | **4.10 mm** | **4.41 mm** | (14.50 mm) |
| Largest offset mirror angle | 3.6 mrad | 3.6 mrad | 25 mrad |
| Largest mirror aperture (800 mm mirrors) | (2.88 mm) | (2.88 mm) | **20 mm** |
| Multiplied by safety factor 1.5 | 6.15 mm | 6.61 mm | -- |
| Including alignment tolerance ±1.5 mm | 9.15 mm | 9.61 mm | 23 mm |
| Chosen diameter of ring collimator | **15 mm** | **15 mm** | **25 mm** |
| Distance of beam stop to source point | 300 m | 320 m | 260 |
| Projected ring collimator size | 17.3 mm | 17.1 mm | 27.1 mm |
| Minimum offset possible | 17.1mm | 17.1 mm | 27.1 mm |
| Chosen minimum beam offset | **25 mm** | **25 mm** | **35 mm** |

# Beam stops and slits

For the hard X-ray beamlines, the unfocused FEL beam can be stopped with a water-cooled block of $B_4C$ or graphite in normal incidence geometry. Before the first mirror, it is also necessary to aperture the hard X-ray spontaneous radiation background, which is achieved by a tungsten block after the $B_4C$ block (Figure 16).

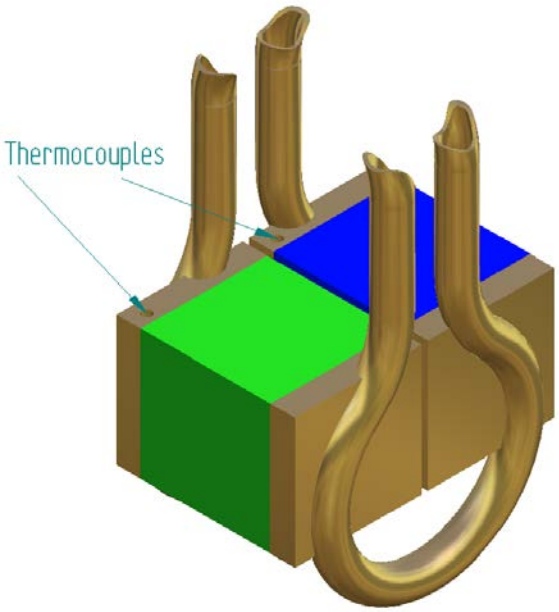


***Figure 16:*** *One blade of a spontaneous radiation aperture. A $B_4C$ block is marked in green colour, a tungsten block to stop the spontaneous radiation in blue. The incident beam comes from the front left corner.*

The number of pulses that can be absorbed in this assembly is shown in Figure 17. For SASE3, it will be necessary to use grazing incidence geometry in the region where the slit can interact with the full pulse train. The precise geometry is the subject of current FEA studies.

A description of a planed prototype slit and thermal calculations can be found at:

http://edmsdirect.desy.de/edmsdirect/file.jsp?edmsid=2022671
http://edmsdirect.desy.de/edmsdirect/file.jsp?edmsid=2004661

Beams focused in one dimension (~ 100 µm) can be apertured in grazing incidence geometry for example by mirrors. For two-dimensionally focused beams in the micron range (for example, around the sample) there is currently no concept for aperturing the beam.

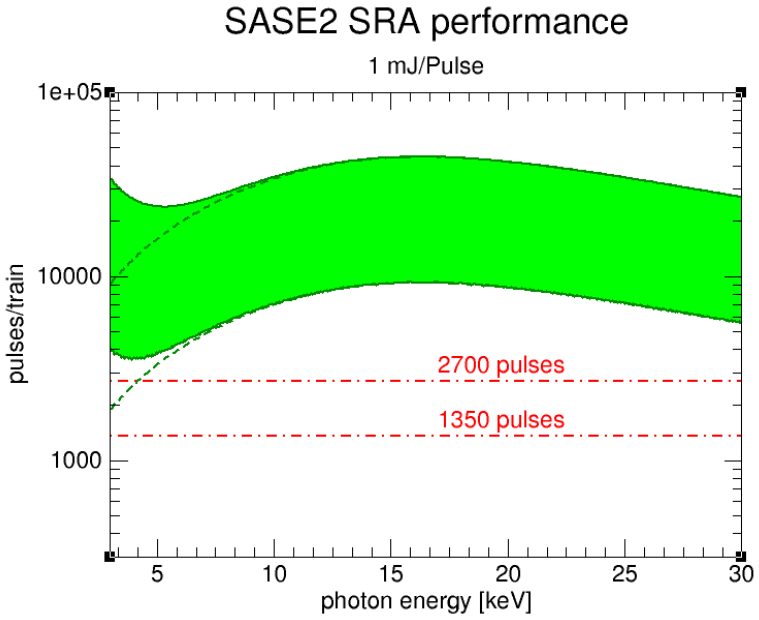


***Figure 17**: Number of pulses in a SRA blade for SASE2 in front of the first mirror*

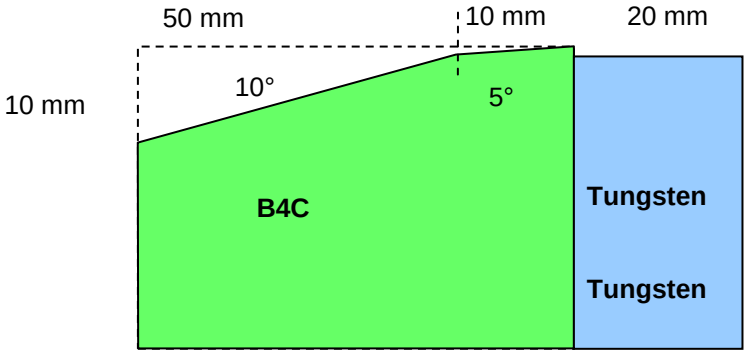


***Figure 18:** Possible slit assembly for SASE3 beam conditions. The beam direction is from the left.*

# Offset and distribution mirrors

When coherent beams are deflected by non-perfect mirrors, phase errors are introduced to the wavefront. After some propagation distance, the phase errors will start to smoothen; however, intensity variations in the beam profile will arise instead. This will lead to vertical stripes in the beam profile in the experiment stations, a phenomenon also known from first experiments at LCLS. These stripes can be extremely disturbing, in particular for experiments with non-linear cross sections. To minimize this effect, the best possible mirror technology has to be applied for offset and distribution mirrors. Currently, the best figure errors of mirrors of 400–500 mm length are in the range of 2 nm peak to valley (PV). After consultation with several mirror manufactures and experts in metrology, we believe that this limit can be pushed to 800 mm long mirrors with a figure error of 2 nm PV. This is a baseline assumption of the conceptual design presented here. As shown in Chapter 7, “Wavefront simulations”, there will still be significant beam inhomogeneities, which are typically in the order of distortions that are introduced by a 4σ aperture. Therefore, the beam should be cut by mirrors by not more than 4σ; otherwise, those cut-off effects would dominate the inhomogeneities in the beam profile.

Another possible way to reduce the effect of profile errors would be a clean-up slit in a focus behind the mirrors. Such an intermediate focus is part of the distribution mirror concept for the hard X-ray branch beamlines, and could be easily generated for the centre beamlines as well. In the current baseline design, such slits are not foreseen, but can be added later, if desired.

In this section, the position and focusing requirements on offset and distribution mirrors are discussed. An overview of required beam motions that occur with the chosen concept is also provided in [5].

## Position of the offset mirror and energy tunability

The offset mirrors are placed as close as possible to the source in order to reduce wavefront distortions: Since the phase error, introduced to the wavefronts, scale with the sine of the incidence angle, this angle should be as

shallow as possible. On the other hand, to maximize the transmitted beam cross section, the mirrors should be as close as possible to the source (at SASE 3, the single shot damage limitation has to be taken into account as well). However, if 4σ transmission of the beam is targeted and the critical angle is the *upper* possible reflection angle, a minimum required mirror length can be calculated for given photon energy and source–mirror distance. Since the critical angle increases linearly with wavelength (see Figure 55), but the divergence increase is less than linear (see Figure 8), the minimum required mirror length will be the largest at the highest energies. The values for the minimum mirror lengths for the actual positions in the beamlines are around 500 mm for the hard X-ray beamlines and 300 mm for the soft X-ray beamline (Table 9). These lengths would be in principle enough to fulfil the 4σ-requirement over the entire photon energy range; however, as soon as the photon energy is changed, the angles of the offset mirrors would have to be re-adjusted. This can be achieved by moving the second mirror laterally and steering the beam back to the sample location with the angle of the second offset mirror (Figure 19). The additional length of 800 mm long mirrors can be used to obtain tunability ($E_{max}/E_{min}$) over a photon energy range, where no adjustments are required, or to minimize wavefront distortions at a particular energy by setting the offset mirrors at shallow as possible without cutting the beam.

***Table 9:*** *Minimum required offset mirror lengths and tunability at highest photon energies.*

| | **SASE1** | **SASE2** | **SASE3** |
|---|---|---|---|
| Distance | 270 | 290 | 250 |
| $E_{max}$ | 24 keV | 24 keV | 3 keV |
| $\alpha^*(E_{max})$ | 1.1 mrad | 1.1 mrad | 9 mrad |
| divergence (FWHM) | 1.1 µrad | 1.1 µrad | 6.2 µrad |
| $l_{mim}$ (4σ, $E_{max}$) | 456 mm | 490 mm | 291 mm |
| $l_{mirror}$(800mm)/$l_{min}$ | 1.75 | 1.63 | 2.75 |
| $E_{max}/E_{min}$** | 1.93 | 1.78 | 3.85 |

* Critical angle for carbon coated mirrors

** $E_{max}/E_{min} > l_{mirror}/l_{min}$ because of non-linear behaviour of divergence/E. Tunability increases for lower energies.


***Figure 19:*** *Changing the incidence angle of the offset mirrors will require moving the second offset mirror horizontally. The beam displacement is compensated by beam steering with the second offset mirror.*

## Positions of distribution mirrors

The position of the distribution mirrors is, in principle, defined by the critical angle of the highest photon energy required and the lateral space available in the tunnel. Another constraint comes from requirement that the beam size for the lower photon energies has to be reduced in front of the distribution mirror because its aperture cannot be adjusted by tuning the incidence angle. If the second offset mirror is used to focus the beam onto the distribution mirror, the distance between them should be at least 50 m to avoid too tight bending

radii and possible damage by accidentally focusing onto the distribution mirror.

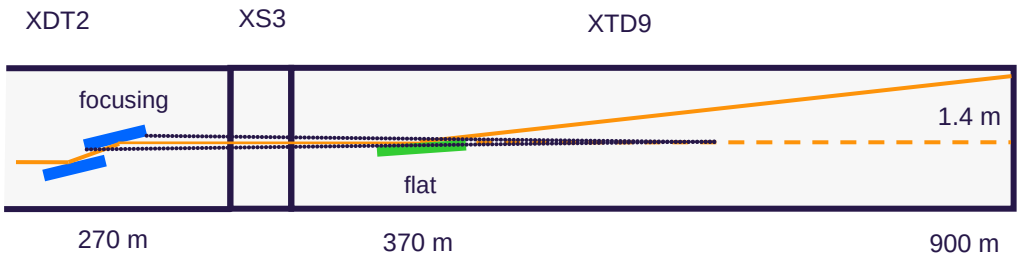


***Figure 20:*** *Distribution mirror concept with intermediate focus*

For SASE1 and SASE2, the tunnel geometry allows a positioning of the distribution mirrors and intermediate foci such that the distribution mirror can be flat and the horizontal beam size matches the vertical beam size at the experiment. This setting has the advantage that a relatively fast beam switching between the two experiments could be achieved by a slight angular motion of the second offset mirrors only, without changing any bending radii. This geometry is shown in Figure 21**.**

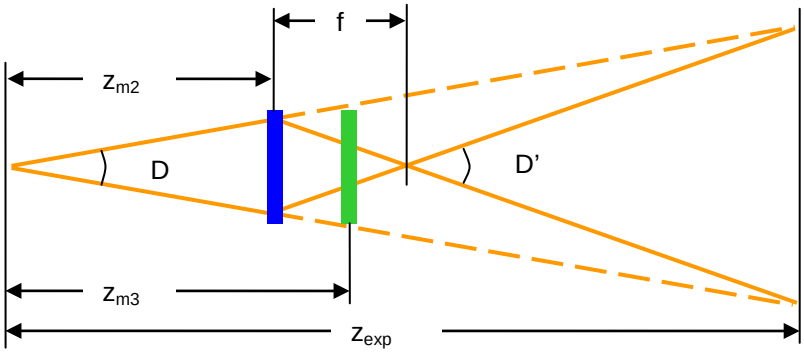


***Figure 21:*** *Intermediate focus concept with a flat distribution mirror*

From the figure follows for SASE1 and SASE2

$$D \times z_{m2} = D' \times f \qquad (5)$$
$$D \times z_{\exp} = D' \times \left(z_{\exp} - z_{m2} - f\right)$$

and

$$f = z_{m2}\frac{z_{\exp} - z_{m2}}{z_{\exp} + z_{m2}} \qquad (6)$$

$$D' = D\frac{z_{\exp} + z_{m2}}{z_{\exp} - z_{m2}}$$

To obtain, at the steepest possible angle of the second offset mirror $\alpha_{\max}^{m2}$, the equivalent footprint at the distribution mirror, one has to set (for equally long mirrors)

$$z_{m3} = z_{m2} + f\left(1 - \frac{\alpha^{m3}}{\alpha_{\max}^{m2}}\right) \qquad (7)$$

The bending radius of the second distribution mirror can be calculated as

$$\frac{2}{R_{m2}\sin\alpha^{m2}} = \frac{1}{z_{m2}} + \frac{1}{f} \qquad (8)$$

To obtain the natural beam size at the experiment, the distribution mirror can remain flat in the settings above. This is, for example, useful if a monochromator is used and a maximum number of transmitted pulses is desired. However, for certain experiments, one might want to use the possibility of focusing the beam horizontal with the offset or distribution mirror. For focusing to the experiment at the branch beamline, the distribution mirror has to be bent concave:

$$\frac{2}{R_{m3}\sin\alpha^{m3}} = \frac{1}{z_{\exp} - z_{m3}} - \frac{1}{z_{m2} + f - z_{m3}} \qquad (9)$$

For the central beamline, the second offset mirror could be used to focus onto the sample.

The required radius would be

$$\frac{2}{R_{m2}\sin\alpha^{m2}} = \frac{1}{z_{m2}} + \frac{1}{z_{\exp} - z_{m2}} \qquad (10)$$

The magnification of the source in the latter case is

$$M_{\max}^{central} = \frac{z_{\exp} - z_{m2}}{z_{m2}} \tag{11}$$

For the branch beamline, the magnification is

$$M_{\max}^{branch} = \frac{f}{z_{m2}} \frac{z_{\exp} - z_{m3}}{z_{m2} + f - z_{m3}} \tag{12}$$

For SASE3, there are two different branch beamlines. For the monochromatic beamline (SCS experiment) the horizontal deflection angle is related to the efficiency of the monochromator and is discussed in “Soft X-ray monochromator”. The position of the distribution mirror for the other branch beamline (SQS2) is planned directly behind the monochromator. In this way the distribution could be also used to reflect monochromatic beam into the SQS experiment. With the position of the distribution mirror fixed, the intermediate focus is then defined by Equation (7) the required bending radius of the second offset mirror by Equation (8) and bending of the distribution mirror the focusing condition by Equation (9). To obtain a round beam in the experiment station SQS2, the distribution mirror has to have a strong convex bending of -3.5 km. This case could be interesting for SQS2 if long pulse trains with maximum bunch charges are desired. As shown in “KB mirrors”, a pre-focused beam would limit the maximum energy per pulse to about 1 mJ if a KB system is used for micro-focusing. Another option to mitigate this problem would be to place the intermediate focus in front of the distribution mirror, which would lead to a natural beam size in the station with a flat distribution mirror. In that case, the requirements on bending of the second offset mirror increase to a minimum required bending radius of 5 km. Table 10 summarizes the required bending radii for SASE1, SASE2, and SASE3 with the intermediate focus after the distribution mirror.

***Table 10:*** *Mirror distances, intermediate foci, bending radii, and magnification ratios of the source in focusing condition at the lowest X-ray energies*

| | $z_{m2}$ | $z_{m3}$ | $z_{exp}$ | $f$ | $R_{m2}$ | $R_{m3}$ *round* | $R_{m3}$ *focus* | *M central* | *M branch* |
|---|---|---|---|---|---|---|---|---|---|
| SASE1 | 280 | 370 | 900 | 150 | 54 km | flat | -100 km | 2.2 | 4.7 |
| SASE2 | 300 | 390 | 940 | 160 | 58 km | flat | -123 km | 2.1 | 4.2 |
| SASE3 | 252.8 | 357 | 422 | 162 | 7.9 km | -3.5 km | -116 km | 0.67 | 0.72 |

## Control of bending radii

As can be seen in Table 10, it is crucial to control the bending radii with high accuracy. For example, the distribution mirrors are typically 60 m in front of the intermediate focus to get a 4σ footprint of the converging beam. A change of focus by 6 m would then lead to a noticeable 10% change of the footprint. At SASE1, a change of *f* from 150 m to 145 m is related to a change of bending radius $R_{m2}$ from 54.2 km to 53.0 km at 3.6 mrad incidence angles and from 177.4 km to 173.6 km at 1.1 mrad incidence angles at the offset mirrors.

The bending radius can be also expressed as a height difference *h* in nm in the centre of the mirror:

$$h[nm] = \frac{l_{mirr}^2[mm]}{8\,R[km]} \tag{13}$$

Equation (13) gives a height difference of 33 nm at 3.6 mrad and 10 nm for the 1.1 mrad case.

Similarly, for the distribution mirror, the difference between flat and a convex radius of -100 km lead to a difference between a round beam (5.57 mm FWHM for 3 keV) and focused beam (4.7 × 46.6 µm = 220 µm). If the beam size has to be controlled to an accuracy of 10% of the focused beam (20 µm), this leads to 3 nm stability of curvature of the distribution mirror. On the other hand, the tolerance that leads to 10% size variation of a round beam at 12 keV is around 30 nm.

For SASE3, similar criteria lead to required precisions of 87 nm for the offset mirrors and 30 nm for the distribution mirror for a focused beam.

In conclusion, changes of the bending profiles of offset and distribution mirrors in the range of 10–30 nm will lead to noticeable change of the beam size in the experimental stations. For extremely demanding situations (for example focusing to a few hundred microns over many hundreds of meters), requirements to mirror profile stability increase to a few nanometres.

As shown in Appendix B, “FEA on first offset mirror”, the maximum expected profile deformations during a pulse train at SASE1 and SASE2 are in the range of 2–3 nm, compatible with the criteria for stability above.

It should be noticed that it is *not* necessary to achieve an absolute calibration of the bending radius to this precision (for example by offline metrology). Instead, reference points for bending radii can be obtained more easily by comparing horizontal and vertical beam sizes in the experiment stations. On the other hand, bending mechanisms should be stable enough to keep the mirror profile stable within at least 10 nm over several days under measurement conditions. Moreover, fast and reliable methods should be established to re-calibrate bending radii around the working points.

### Heat load on mirrors

All mirrors will experience some heat load from the FEL beam in the range of a few watts and need to be water-cooled. The first mirrors sees in addition also heat load from spontaneous radiation, which is higher than the heat load from the FEL beam, because it is almost fully absorbed in the mirror. In that case, also Compton scattering inside the mirror has to be taken into account. This case is studied in more detail in Appendix B, “FEA on first offset mirror”. For all other mirrors, it is assumed that 13 500 pulses per second based on 1 nC bunch charge are reflected by the mirror for the most critical photon energy setting. The reflectivity is based on calculations with the program XOP, assuming a roughness of 1 nm rms. The estimated heat loads are shown in Table 11.

***Table 11:*** *Maximum expected heat load on mirrors with 13 500 pulses per second, 1 nC per electron bunch, and 17.5 GeV operation. For FEL radiation, the photon energy and the assumed reflectivity are given in brackets.*

| | **SASE1** | **SASE2** | **SASE3** |
|---|---|---|---|
| First offset mirror spontaneous radiation | 4.5 W (closed gap) | 4.5 W (closed gap) | 100 W (closed gap) |
| First offset mirror FEL radiation | 2.5 W (3 keV, 97%) | 2.5 W (3 keV, 97%) | 40 W* (0.5 keV, 70%) |
| Second offset mirror FEL radiation | 2.5 W (3 keV, 97%) | 2.5 W (3 keV, 97%) | 40 W* (0.5 keV, 70%) |
| Distribution mirror | 1.2 W (20 keV, 91%) | 1.2 W (20keV, 91%) | 10 W (3 keV, 88%) |

* At the carbon edge (284 eV), the reflectivity would go to zero, and the absorbed power would increase to 135 W. However, this scenario is not very realistic, since no photons would be transmitted to the experiment.

## Transmission and single shot damage

Transmissions of the offset mirrors for different angular settings are shown in Figure 22 and Figure 23. Single shot damage is shown in Figure 61 and Figure 66 in “KB mirrors”.

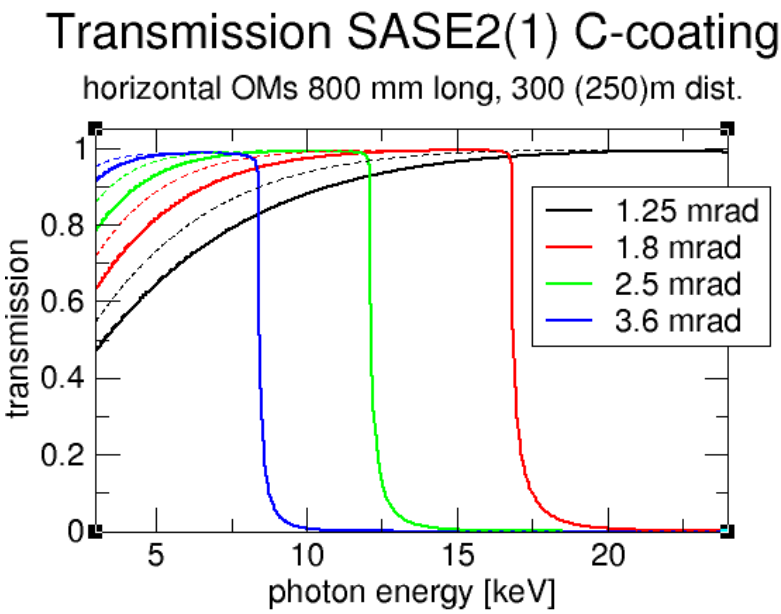


***Figure 22:*** *Transmission of SASE1 and SASE2 offset mirrors for three different incidence angles. The dashed lines are for a position 50 m closer to the source.*

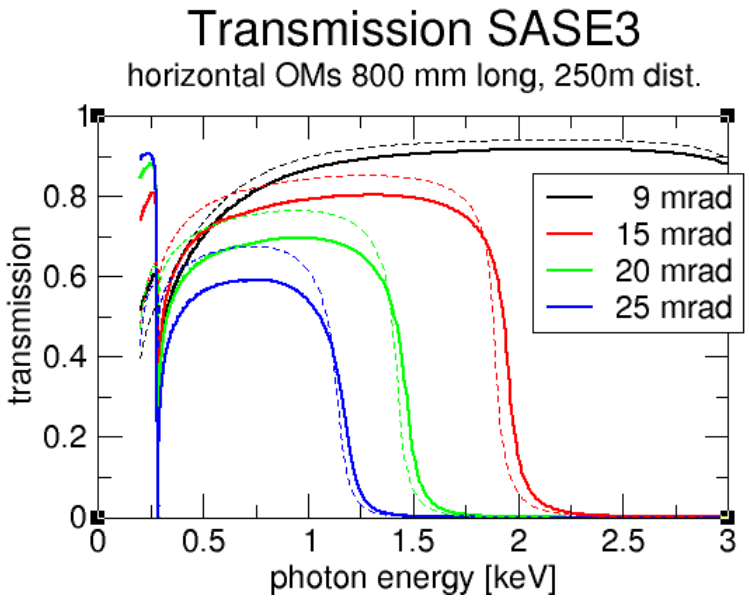


***Figure 23:*** *Transmission of SASE3 distribution mirrors for different incidence angles. Solid lines are for carbon coating, dashed lines for B4C coating.*

## Wavefront propagation

A general description of wavefront calculations and estimates for required mirror perfections are presented in Chapter 7. In this section, we show specific simulations for each beamline and assuming mirror specification derived in Chapter 7. Imperfections of mirrors surfaces were simulated with three model height error profiles shown in Figure 24. For SASE1 and SASE2 beamlines, grazing incidence angles for offset mirrors were taken to provide a 4.5 σ rms beam footprint. For SASE3 beamlines, two fixed incident angles for offset mirrors, 9 and 15 mrad, were used in calculations, for hard and soft photon energy ranges, respectively. For every photon energy, the Gaussian beam with far field angular divergence corresponding to simulations by M. Yurkov et al. [2] for 20 pC electron bunch charge models a source.

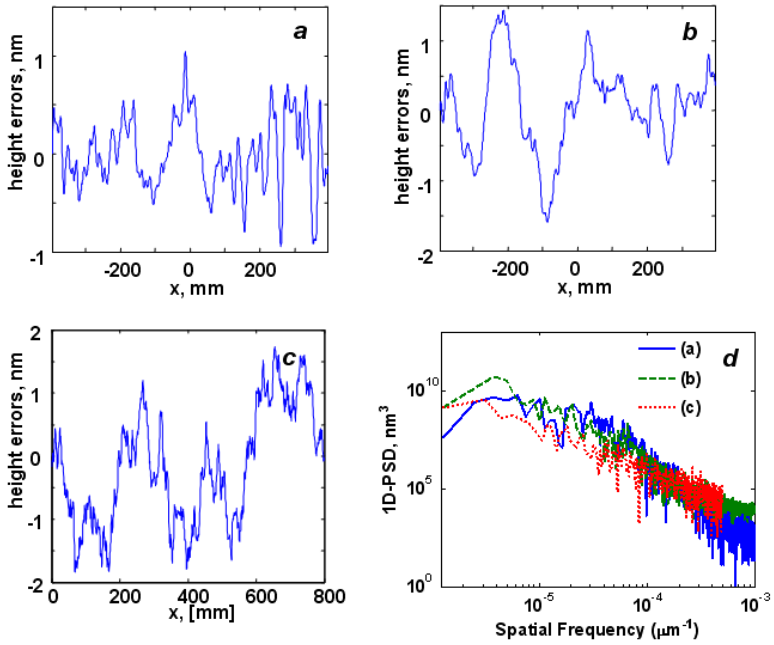


***Figure 24*****:** *Height error profiles a) and b) were used for the first and the second offset mirrors, profile c) was used for distribution mirrors. The PSD curves corresponding to the profiles are shown in the lower-right panel (d).*

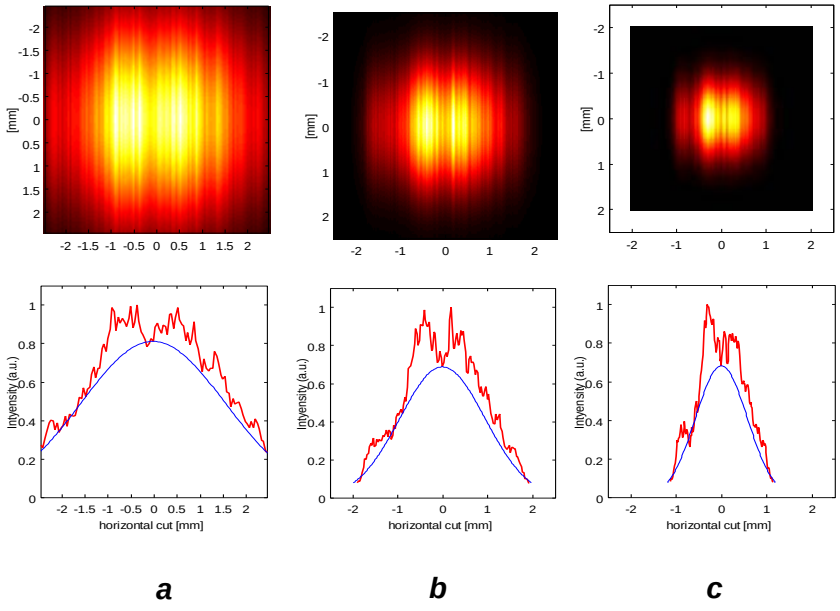


***Figure 25:*** *Wavefront propagation calculations for SPB, the centre beamline of SASE1, photon energy 5 keV (a), 10 keV (b), and 15.5 keV (c).The beam angular divergences correspond to the electron bunch charge 20 pC. The height error profiles for the 800 mm offset mirrors have less than 2 nm PV. Incident angles are 2.6, 1.6, and 0.97 mrad.*

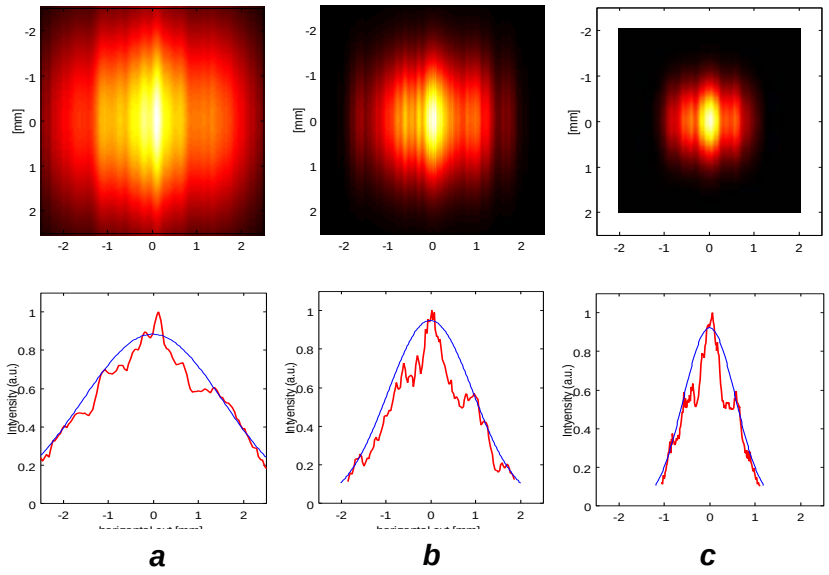


***Figure 26:*** *Wavefront propagation calculations for FXE, the branch beamline of SASE1, photon energy 5 keV (a), 10 keV (b), and 15.5 keV (c). The height error profiles for the 800 mm offset and distribution mirrors have less than 2 nm PV. All other parameters are the same as in Figure 25.*

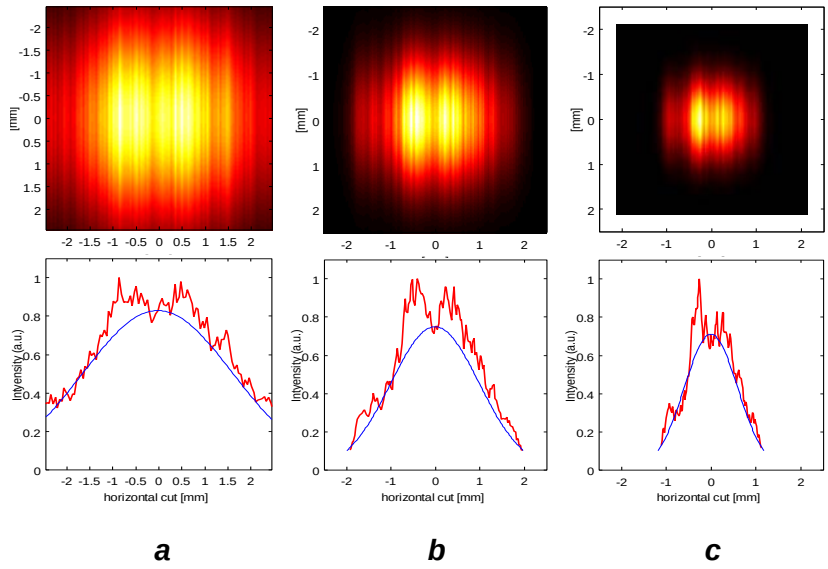


***Figure 27:*** *Wavefront propagation calculations for MID, the centre beamline of SASE2, photon energy 5 keV (a), 10 keV (b), and 15.5 keV (c). Incident angles (2.8, 1.7, and 1.4 mrad) are chosen to provide 4.5 σ rms beam footprint. All other parameters are the same as in Figure 25.*

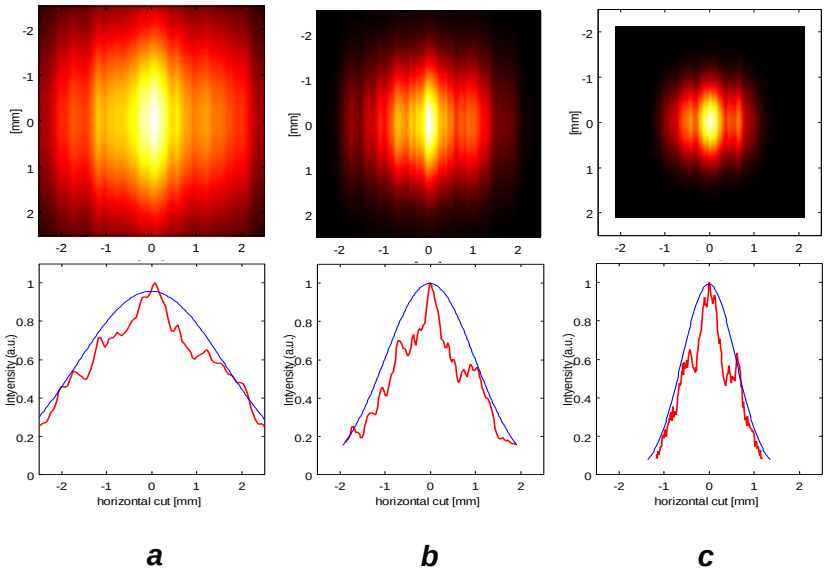


***Figure 28:*** *Wavefront propagation calculations for HED, the branch beamline of SASE2, photon energy 5 keV (a), 10 keV (b), and 15.5 keV (c). All other parameters are the same as in Figure 26*

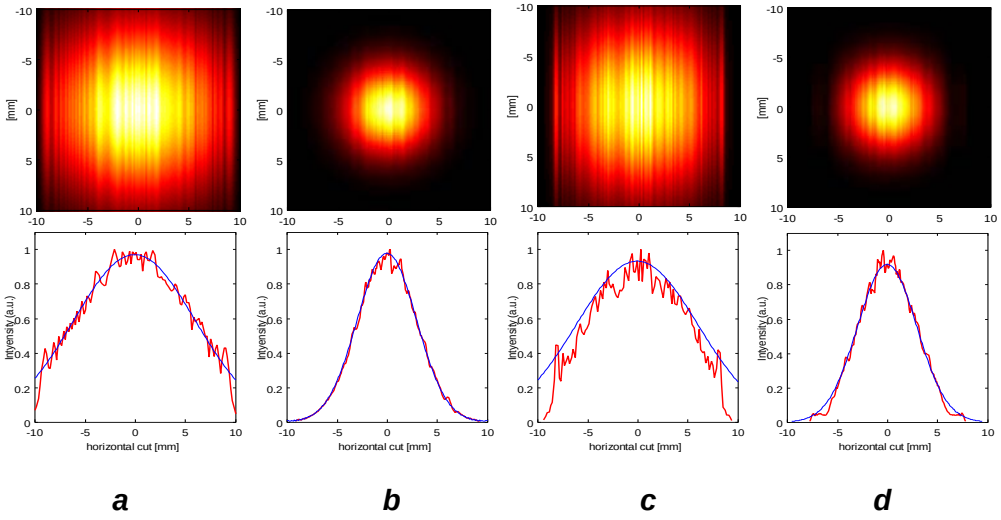


***Figure 29:*** *Wavefront propagation calculations for SQS (a, b) and SQS2 (c, d), the centre and branch beamlines of SASE3, photon energy 300 eV (a, c), and 800 eV (b, d). Incidence angle of the offset mirrors is 15 mrad, for the distribution mirror, 9 mrad***.**

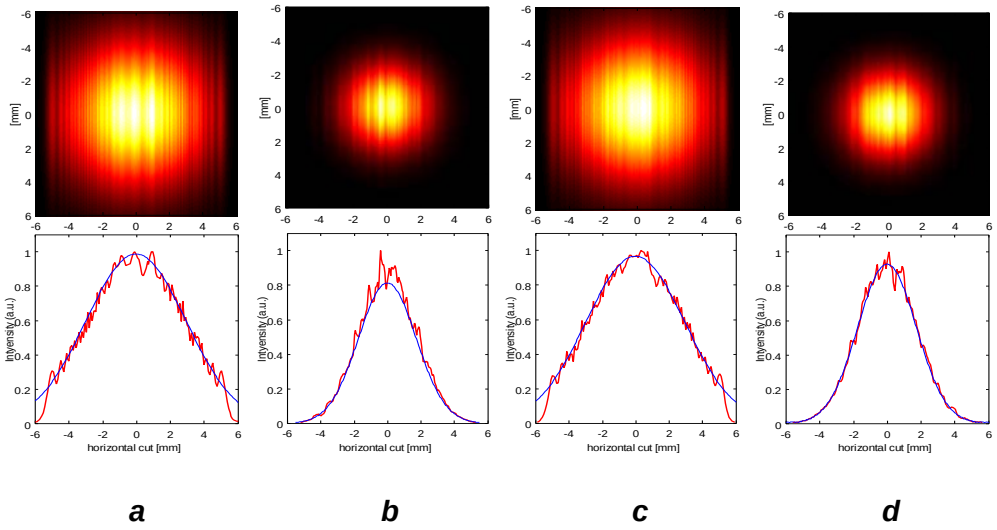


***Figure 30:*** *Wavefront propagation calculations for SQS (a, b) and SQS2 (c, d), the centre and branch beamlines of SASE3, photon energy 800 eV (a, c), and 1.5 keV (b, d). Incidence angles for all the mirrors are 9 mrad.*

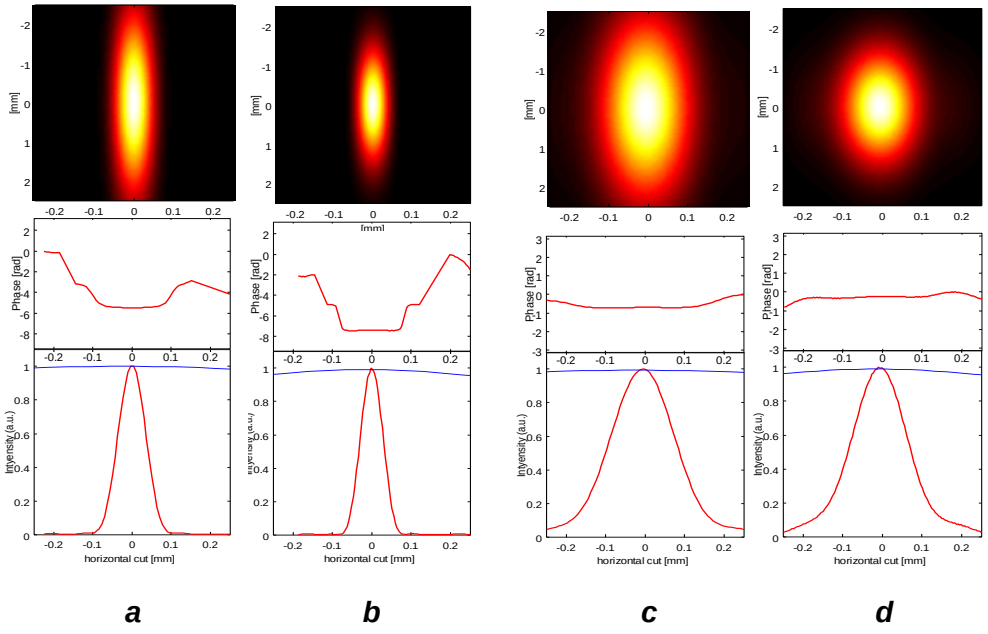


***Figure 31:*** *Wavefront propagation calculations of focusing layout for SPB (a, b) and FXE (c, d) beamlines, SASE1, photon energy 5 keV (a, c), 10 keV (b, d). Offset mirror radii $R_{m2}$: 150 km (a), 245 km (b), 72 km (c), and 120 km (d). Defocusing distribution mirrors radii are $R_{m3}$: -50 km (c) and -80 km (d).*

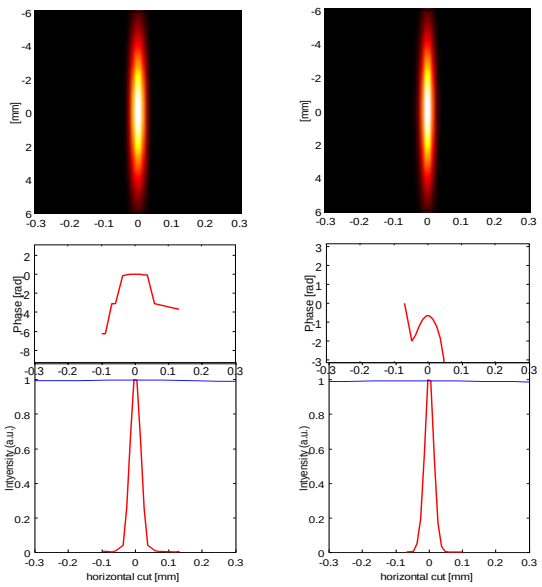


**Figure *32*:** *Wavefront propagation calculations of focusing layout for SQS, SASE3, 800 eV, grazing incidence angle 9 (a) and 15 (b) mrad. Offset mirror radius $R_{m2}$: 223.7 (a)* and *213.5 (b) km.*

## Conclusion

The possibility of adjusting incidence angles at the offset mirrors is crucial to adjust to varying beam sizes at different photon energies. However, it also complicates operations, because frequent re-adjustments of the entire mirror systems are required and the beam moves horizontally within the beam transport systems in the order of 10 cm at the location of the second offset mirror.

With 800 mm long offset mirrors at the current distances to the source in practice, three working points for SASE1 and SASE2 and two at SASE3 are sufficient to cover the entire photon energy range. However, this will depend also on the actual beam divergences delivered by the undulators. If the divergences are larger than the largest calculated divergences today (for example, by 50%), operation would be still possible with almost the same performance; however, more working points for the offset mirror angles would be required.

With the chosen positions for the distribution mirrors, one could operate the branch beamlines with intermediate foci before or after the distribution mirrors without changing their radius of curvature.

Special attention has to be paid to mechanical stability of the mirror chambers and holders and the stability of adjustable mirror bending within 10 nm or better. In the current layout, the first mirror can be passive since deformations can be adjusted with the bendable second mirror. This could be an advantage for the technical design since the first mirror will be exposed to a high radiation background, which will make the implementation of a bending mechanism more difficult. The offset mirrors have to be bendable as well, at least one has to be able to adjust their flatness initially, since fabrication and mounting tolerances on bending radii are larger than the tolerances required here. A full in-situ control of the distribution mirror bending would add control over horizontal beam sizes at the branch beamlines and would enable shifting the position of the intermediate focus for optimization of wavefront properties.

Single-shot damage can be a problem for the SASE3 mirrors and metal-coated mirrors at SASE1 and SASE2. However, operation in pink beam mode at the highest bunch charge seems to be feasible for offset and distribution mirrors with the current beam parameters. Heat-load effects become noticeable when with closed gap undulators in high bunch-charge mode. The Finite Element analysis in Appendix B shows that with water-cooled mirrors the resulting deformations are still acceptable.

# Soft X-ray monochromator

The requirements from the user community are to achieve a resolving power (RP) greater than $10^4$ over a wide energy range and the possibility to work with the zeroth order. The soft X-ray monochromator is based on the variable-included-angle scheme using a plane variable line spacing (VLS) grating. This is a variant of the well-established SX-700 monochromator type originally planned to be used for the SASE3 beamline (see TDR 2006 [4]). In this scheme, a plane pre-mirror is used to provide the variable-included-angle capability. A second mirror after the grating is needed to achieve real focusing on the exit slit. On the other hand, variable line spacing gratings have been shown to work efficiently in the soft X-ray region.The scheme we propose is based on the use of a VLS grating hence eliminating the refocusing mirror. This solution was first proposed by R. Reininger and R. de Castro [6] and provides good results at different existing beamlines. Due to damage issues the use of long grating is the preferable option. It is a challenging solution that will provide unique feature in terms of RP to the beamline.

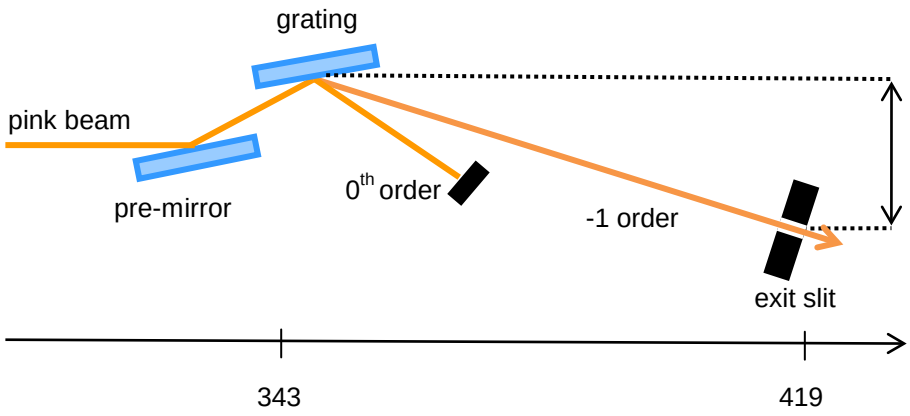


***Figure 33:*** *Monochromator layout (top view)*

The general principle of the beamline can be described as follows: The beam is focused in the horizontal direction with the bendable offset mirror. The focus is located behind the grating, hence being virtual, and at a fixed distance $R_a$. The VLS grating will image the focus of the mirror on the slit such that the distance from the grating to the slit (noted $R_b$) equals $R_a$. As the first focus is virtual, it is $R_b$=-$R_a$. In the vertical direction, the beam propagates without modification up to the focusing optics of the experiment station.

The two critical parameters to be determined are the $C_{ff}$ parameter and $E_{ref.}$ The choice of these parameters will entail the general performance of the monochromator: mainly RP and the photon flux. $C_{ff}$ is equal to $C_{ff}$ = sin(β) / sin(α) where α and β are the incidence and exit angles on the grating with respect to the surface. The RP is varying with the value of $C_{ff}$ and, as in our design, this value has to be kept constant; hence, $C_{ff}$ has to be carefully selected. The value of $E_{ref}$ is the photon energy for which the defocus, coma, and spherical aberration will reach exactly zero, hence providing the polynomial coefficients for the VLS design. For other photon energies, the aberration will not vanish but, as will be demonstrated later, the effects will be nevertheless minor due to the specific geometry (long exit arm) and can be compensated for the defocus term.

It should be also noted that this scheme is flexible enough to be usable if future options, like after-burner for polarization control, are installed.

## Design criteria and resolving power

As stated above, the main goal of the monochromator is to achieve RP > $10^4$ on the full energy range. Considering the fact that the energy range is very broad, the use of two different gratings is needed: one for the low-energy range (0.25 to 1.2 keV), the other one for the high-energy range (1 to 3 keV). The values of 600 and 1200 l/mm were chosen, but can be optimized later on. In order to choose the proper $C_{ff}$ value, the RP can be evaluated by taking into account the contribution of the different optical elements as well as the influence of the FEL source size.

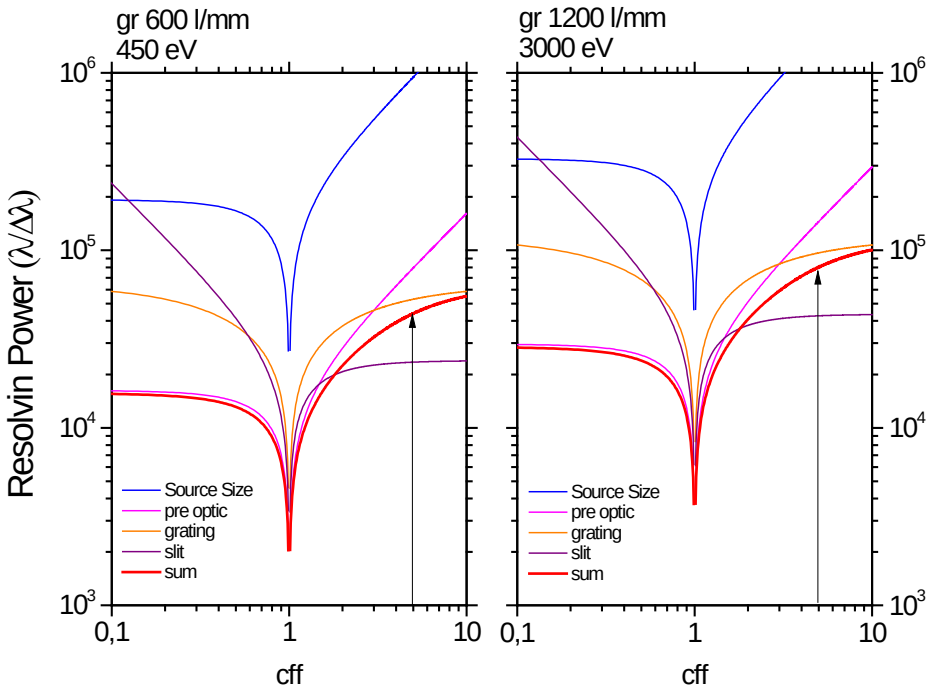


***Figure 34:*** *Contribution of the different elements to the resolving power as a function $C_{ff}$ value for two gratings and at the low and high limit of the photon energy range. The sum is plotted in red.*

Figure 34 shows the achievable RP for 450 and 3000 eV, which are used as two reference points of SASE3 energy range. A large $C_{ff}$ value corresponds to high RP but low transmission. As can be seen, choosing a value of $C_{ff} = 5$ enables a RP > $10^4$ for both photon energies. This estimation does not take into account slope error from the offset mirrors or the heat load induced deformation on the monochromators optics. Hence, the value of 5 should enable keeping RP greater than $10^4$.

Once the $C_{ff}$ value is fixed, the correct angles on the grating can be calculated. The exit angle of the monochromator with respect to the incoming beam is fixed and equal to 21 mrad (1.2°). This enables, firstly, ensuring the separation of the SCS and SQS beamlines and, secondly, decreasing the incidence angle on the pre-mirror, hence increasing the reflectivity.

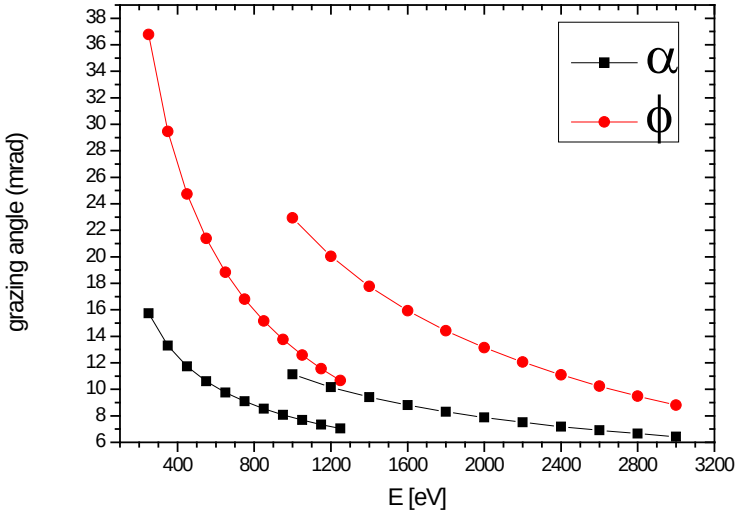


***Figure 35:*** *Grazing angle on the pre-mirror (Φ) and the grating (α) for 600 and 1 200 l/mm grating*

The exact location of the monochromator along the beamline is fixed by the two following criteria:

- The length of the grating is limited to 460 mm. Given the grazing angle α, the size of the footprint (4 σ) on the grating should be smaller than the grating length, for all the photon energy.
- The maximum deviation in the horizontal direction (noted D in the layout figure) allowed by the tunnel is here assumed to be 1.6 m.

According to these two boundary conditions, the monochromator is located 343 m from the source point, corresponding to $R_b$=76m.

## VLS grating

The scheme we propose makes use of a VLS grating instead of a refocusing mirror. This offers the possibility to suppress one optical component, and VLS gratings are known to work better with a focused incoming beam, as in our case.

The groove position (noted n(*w*)) in the grating can be expressed as a function of the position *w* along the grating:

$$n(w) = k.( w + b2.w^2 + b3.w^3 + b4.w4 + \ldots)$$

For a plane grating, the Fresnel optical path function can be written as a power series of the form:

$F(w) = \text{const} + M10.\ w + M20(Ra,b2)\ w^2 + M30(Ra,b3)\ w^3 + M40(Ra,b4)\ w4$

where $M_{20}$, $M_{30,}$ $M_{40}$ are related to the defocus, coma, and spherical aberrations. The different terms are zeroed for the specific photon energy ($E_{ref}$) that allows calculating the VLS polynomial coefficients.

As the coefficients are calculated for single photon energy, the terms of the Fresnel optical path do not exactly vanish leading to a decrease of the RP. This will be illustrated in the next paragraph, using ray tracing.

## Ray tracing

The full beamline has been modelled using the ray-tracing software SHADOW. The ray tracing is performed with the source parameters (divergence, source size) obtained from M. Yurkov et al. [2]. An example of the results is shown in Figure 36.

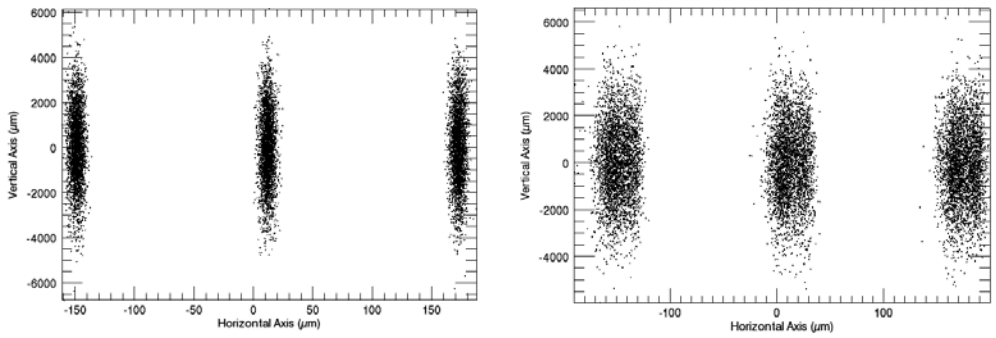


***Figure 36:*** *Ray tracing results for three different photon energies (1 598.4, 1 600, and 1 601.6 eV). This corresponds to RP=$10^4$.* Left: *Perfect optics.* Right: *With slope error included for the pre-mirror and the grating.*

From these results the RP can be evaluated using the following formula:

$$RP = \frac{E}{2.688\sigma_z \, {\Delta E}/{\Delta z}}$$

where $\sigma_z$ is the rms value of the central spot fitted as a Gaussian distribution, and $\Delta E/\Delta z$ is the dispersion obtained from the location of the side spots. The resulting RP is plotted in Figure 37. The RP is higher than $10^4$. In order to investigate the effect of slope error, the surface of the pre-mirror and the grating were modeled by non-ideal mirror surfaces. The surfaces were obtained by fitting a real mirror profile measured with a long trace profiler. The slope error was then 1.8 µrad for the pre-mirror and 1.48 µrad for the grating. The RP with non-ideal optics is shown as the black curve in the figure below. As can be seen, for the full energy range, the RP is still higher than $10^4$. Nevertheless, as FEL beam is highly coherent, a more accurate evaluation of effect of the slope error should be provided by wavefront simulations. This work is currently ongoing.

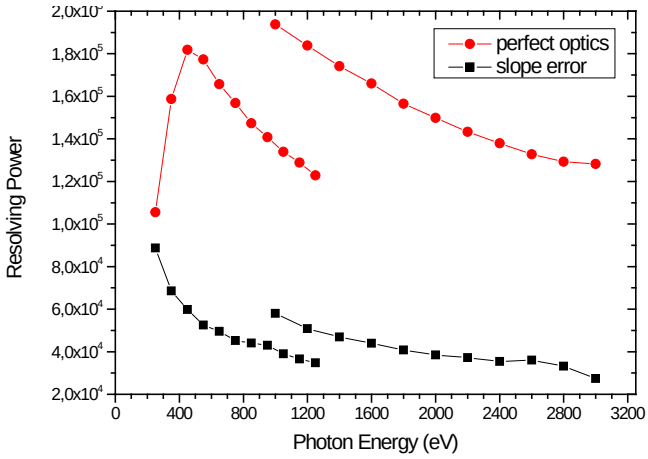


***Figure 37**: Resolving power obtained from ray tracing. The red curve is for perfect optics (no slope error), the black curve include slope errors on the pre-mirror and the grating*

As stated previously, the coefficients for the VLS are calculated for $E_{ref}$. In case $E \neq E_{ref}$, the different terms of the Fresnel optical path do not become zero (especially the defocu term). This leads to a shift of the focus, as can be seen in Figure 38. The position "0" is where the focus of the VLS is located, in this particular case for $E_{ref}$ = 650 eV. This can be compensated by fine-tuning the bending of the second offset mirror. This should allow enhancing the RP for the different photon energies different from $E_{ref}$ and improve the focusing in the experimental chamber.

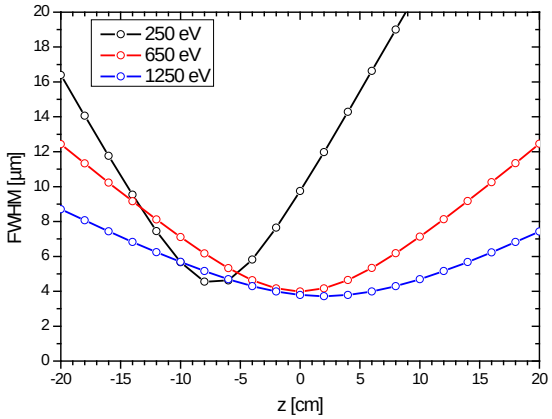


***Figure 38**: Caustic of the beams for three different photon energies: 250 eV, 650 eV (=$E_{ref}$), and 1 250 eV*

## Efficiency

The transmission of the monochromator (pre-mirror and grating) was estimated using REFLEC and assuming a 40 nm thick carbon coating. The diffraction efficiency is fixed by two main parameters: the duty ratio and the groove depth of the grating. These two parameters will have to be optimized later on. For our estimate, we have considered a standard laminar grating with constant duty ratio. The value given in Figure 39 should then be considered as the minimum achievable values. As can be seen, the total transmission ranges from 4% to less than 1%.

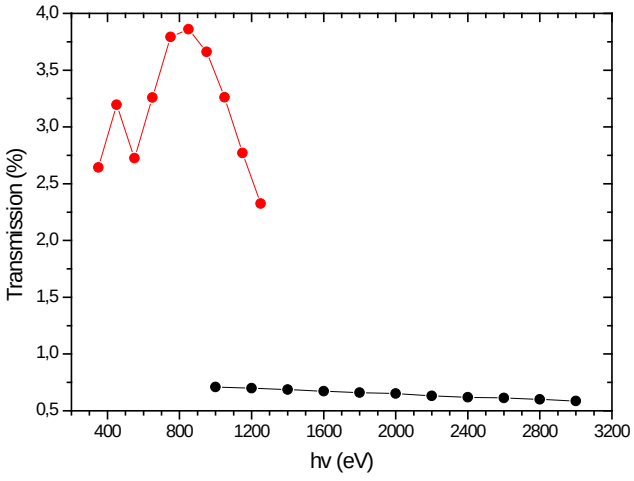


***Figure 39**: Total transmission of the monochromator, pre-mirror reflectivity is included in this calculation*

## Temporal broadening

Since the XFEL will provide ultrashort pulses, one has to be aware that a high resolving power will lead to a temporal broadening of the pulse.

For an estimation of the total broadening, we used the following formula:

$$\Delta t = 2.35\,\sigma\,N.\frac{\lambda}{c}$$

where $\sigma$ is the rms value of the beam footprint on the grating in the horizontal direction, and $N$ the line density. Figure 40 shows the temporal broadening obtained in the case of the most divergent beam (that is, the lowest bunch charge). The σ value is obtained from the ray-tracing.

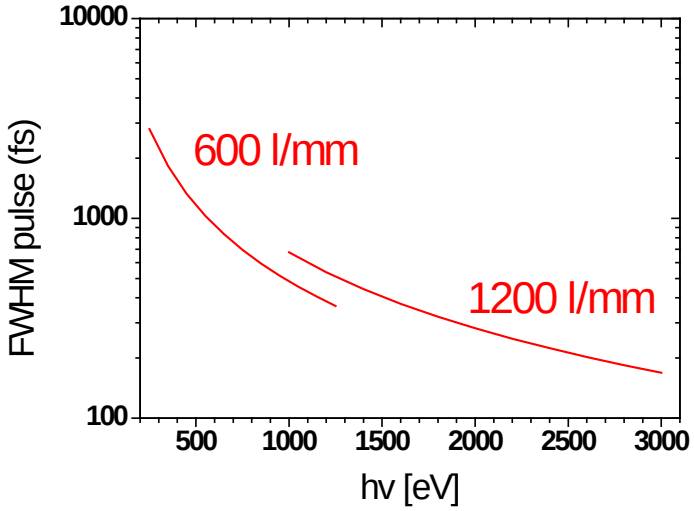


***Figure 40:*** *Temporal broadening from the grating*

This effect can be reduced by decreasing the number of illuminated lines (aperturing of the beam). This will of course lower the transmission and the RP and a trade-off will then have to be found for each particular experiment.

## Single shot damage

The single shot damage is one of the most critical issues of the monochromator design. Due to the limited length of the grating, it has to be placed in a convergent beam. The absorbed dose in the pre-mirror and the grating can then be evaluated, taking into account the source parameters and

the reflectivity of the mirror and the grating. The results are shown in Figure 41 for 1 mJ of incident pulse energy. The most critical element is the pre-mirror, due to the steep angle. The damage threshold of amorphous carbon has been measured to be 100 meV per atom at 830 eV at normal incidence. Considering fatigue effects this threshold could be lowered to about 30 meV per atom, which would limit the acceptable pulse energy to about 2 mJ at 1200 eV. On the other hand, for the pre-mirror, the electron transport effect could become important, enhancing the damage threshold. The case of the grating is more difficult to evaluate as at the edge of the laminar grating structure the incidence angle is almost perpendicular.

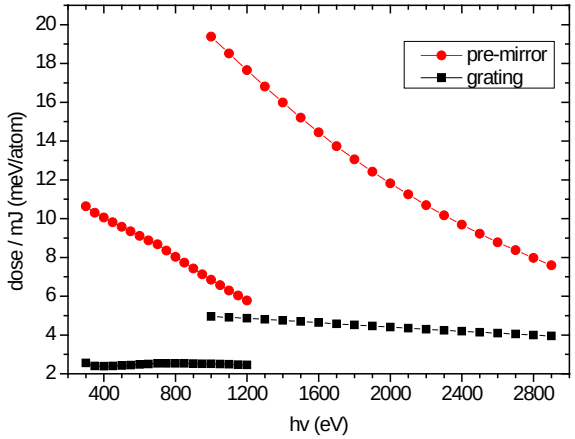


***Figure 41:*** *Dose on the pre-mirror and the grating as a function of photon energy and for 1 mJ / pulse*

Investigations of damage on the specific grating structure are under way and should provide valuable data.

## Heat load

The heat load can be evaluated by considering the absorbed power on the pre-mirror and the grating, and the footprint deduced from ray tracing. In Table 12, we consider the 1 nC beam case, as it is the most critical one with the lowest divergence and highest pulse energy. The results presented here correspond to the case of an impinging train of 2 700 FEL pulses of 1 mJ at photon energy of 450 eV and 1 600 eV. The power is averaged over the 600 µs of the pulse train, which is the most extreme approximation.

***Table 12**: Heat load on pre-mirror and grating*

| Element | Photon energy (eV) | Incident power (KW) | Footprint: (4σ cm x cm) | Absorbed power (W) | Power density (W / mm²) |
|---|---|---|---|---|---|
| Pre-mirror | 450 | 4.5 | 1.04 x 14.74 | 900 | 2.16 |
| | 1600 | 4.5 | 0.37 x 8.13 | 720 | 8.83 |
| Grating | 450 | 3.6 | 1.04 x 30.99 | 500 | 0.57 |
| | 1600 | 3.78 | 0.37 x 14.69 | 189 | 1.28 |

The pre-mirror is the most critical element. At synchrotron sources, similar power densities have been reported and are handled with the use of cryogenic cooling.

We are currently investigating the deformation induced by this type of heat load using FEM simulations. In the worst case, the number of pulses will have to be limited as for crystal hard x-ray monochromator.

## Conclusion

The presented concept for the SASE3 monochromator fulfils and should even exceed the expectation of users. The advantages can be summarized by the following points:

- RP > $10^4$ on the full energy range, with $0^{th}$ order available
- Minimum number of optical elements
- Flexible design enabling us to cope with future upgrades (after-burner for polarization control)

# Hard X-ray monochromators

In this section, silicon and diamond-based monochromators at a distance of 850 m from the source are investigated. The spot size is assumed to be the natural spot size that would occur without distribution mirrors. The horizontal beam size can be changed by bending of the second offset or the distribution mirror at the branch beamline, which would consequently change the number of transmitted pulses through the monochromator. However, for both hard X-ray beamlines, the optics should be able to deliver at any energy the natural spot size at the location of the monochromator, even though the divergence might be different (on the scale of a few microradians) in the horizontal direction at the branch beamline. The location at 850 m is 60 m before the experiment hall, which would give opportunity to pre-collimate the beam with small divergences towards the experiments. If no pre-collimation is required, the monochromator could be also closer to the experiment with no significant changes to the results of this report. A monochromator position before the offset mirrors around 250 m after the sample would reduce the number of transmitted pulses significantly and would also expose the monochromator to the spontaneous background radiation, which is not considered here in the heat-load calculations. The beam size at 850 m is shown in Figure 42.

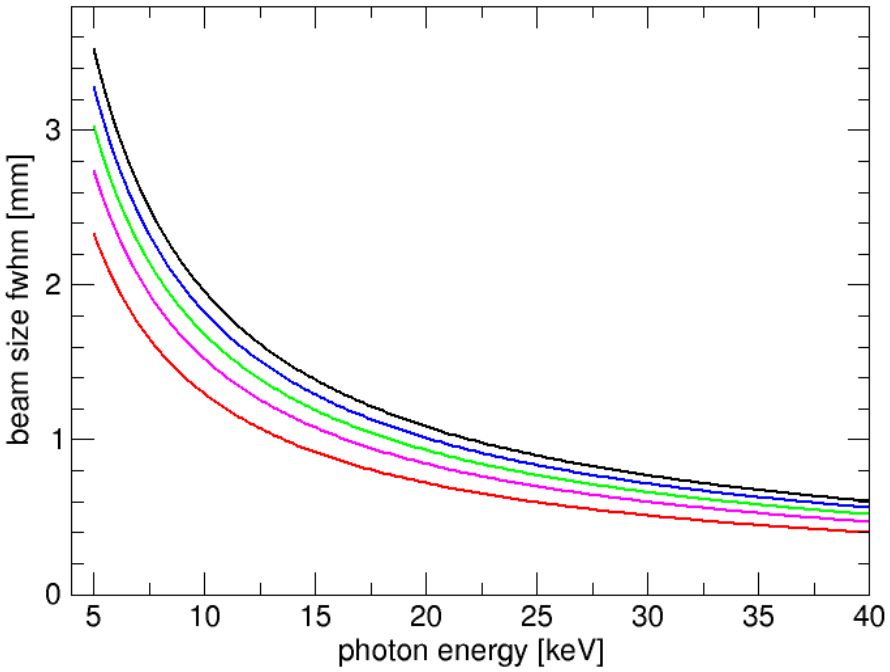


***Figure 42:*** *Beam size at the locations of the monochromator at 14 GeV. The red curve represents calculation for 1nC, the other colours lower bunch charges (see colours in Figure 12).*

## Bandwidth of the monochromator

The energy widths (Darwin width) of a Si (111) reflection are shown in Figure 43. At 10 keV the relative bandwidth of a single reflection is 1.37E-4 and it varies very little with temperature and energy. The acceptable drift of the first crystal with respect to the second one should be of the same order, if one accepts a drift through the fwhm. Here, we assume 1.4E-4 as tolerable drift, which would mean an intensity variation of about a factor of two during a pulse train. For diamond (111) the relative bandwidth is 6.5E-5.

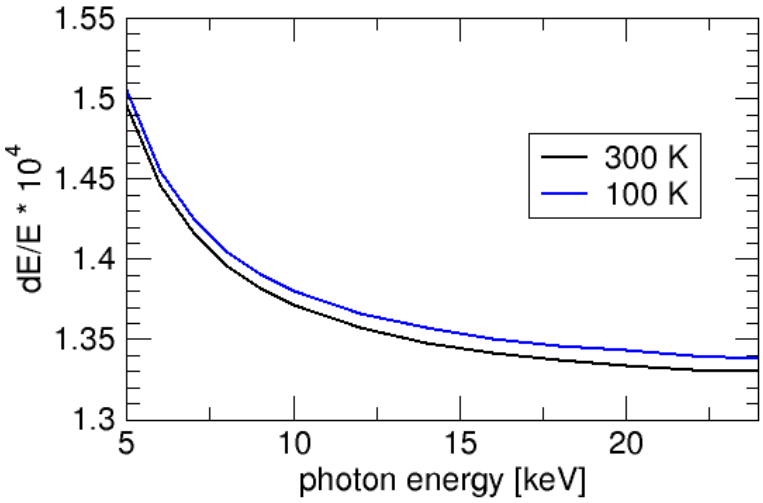


***Figure 43:*** *Darwin width of Si (111) reflection for two different temperatures. Calculations were done with the program XOP.*

To get an estimate on the allowable temperature drift, one has to integrate over the thermal expansion coefficient *α(T)*:

$$\frac{dE}{E} = \alpha(T)\,dT$$

$$1.4\times10^{-4} = \int_{T_0}^{T_0+\Delta T} \alpha(T)\,dT \quad , \tag{14}$$

which gives $\Delta T$ = 50K in the case of $T_0$ = 300K silicon. The amount of heat *W* that leads to this temperature increase can be obtained by integrating over the specific heat $c_p$:

$$W_{\max} = \int_{T_0}^{T_0+\Delta T} c_p(T)\,dT \tag{15}$$

Results are summarized in Table 13.

***Table 13:*** *Maximum temperature drifts for silicon and diamond monochromators*

| | Temperature [K] | Tolerable relative drift [$10^{-4}$\| | Max. ΔT | $W_{max}$ /grams | $W_{max}$ /atom | $W_{damage}$ /atom |
|---|---|---|---|---|---|---|
| Si (111) | 300 | 1.4 | 50 K | 36.3 J/g | 10.5 meV | 0.4 eV |
| Si (111) | 100 | 1.4 | 144 K | 64.3 J/g | 18.7 meV | 0.4 eV |
| C (111) | 300 | 0.65 | 52 K | 31.4 J/g | 3.9 meV | 1 eV |
| C (111) | 100 | 0.65 | 168 K | 29.0 J/g | 3.6 meV | 1 eV |

**Estimation of thermal drift of the first crystal:** Calculations were done under the assumption that the full SASE pulse energy is absorbed in the first crystal. Since the reflected bandwidth will be less than 10% of the SASE bandwidth, the beam reflection was not considered. The second crystal will see only the bandwidth of the first crystal and—provided that the second crystal fulfils the Bragg condition—will reflect most of that. Therefore, the temperature drift of the second crystal was also ignored in the calculations.

Calculations were performed for selected cases with a one-dimensional FEA with temperature-dependent thermal conduction and heat capacities. Results are compared with analytical approximations without (adiabatic) and with heat conduction with transport coefficients fixed in the middle of the drift range.

## Adiabatic analytical approximation

To get a first assessment on thermal behaviour of the monochromator, thermal transport during the pulse train can neglected. As shown below, time constants for thermal transport are in the range of many microseconds in some cases longer than the pulse trains. On the other hand, it is assumed that heat removal in the 100 milliseconds between pulse trains is “perfect”. This can be justified, since the time-averaged maximum heat load on the first crystal is only around 30 watts (12 keV) and can be easily removed with water or cryogenic cooling and small temperature gradients.

The number of transmitted pulses per train is then given by the ratio of maximum allowed heat $W_{max}$ and the heat deposited $W_{pulse}$ in one pulse.

For incidence angles larger than the critical angle, it is:

$$N_{pulse} = \frac{W_{\max}}{W_{pulse}} = \frac{\pi\, b_{fwhm}^2\, z_{abs}\, \rho_m W_{\max}}{4\ln(2)\, m\, E_{pulse}}, \tag{16}$$

where $z_{abs}$ is the attenuation length in normal incidence, $b_{fhwm}$ the beam size, and $\rho_m$ the mass density. With the beam conditions defined in Equations (3) and (4) on page 29, the number of transmitted pulse is calculated and shown in Figure 44 and Figure 45.

Due to its low X-ray absorption cross section, a diamond monochromator can accept 10 times more pulses than a silicon monochromator. Note that considerations so far are independent of geometry and details of the cooling scheme, as long as the average heat load is removed in between pulse trains.

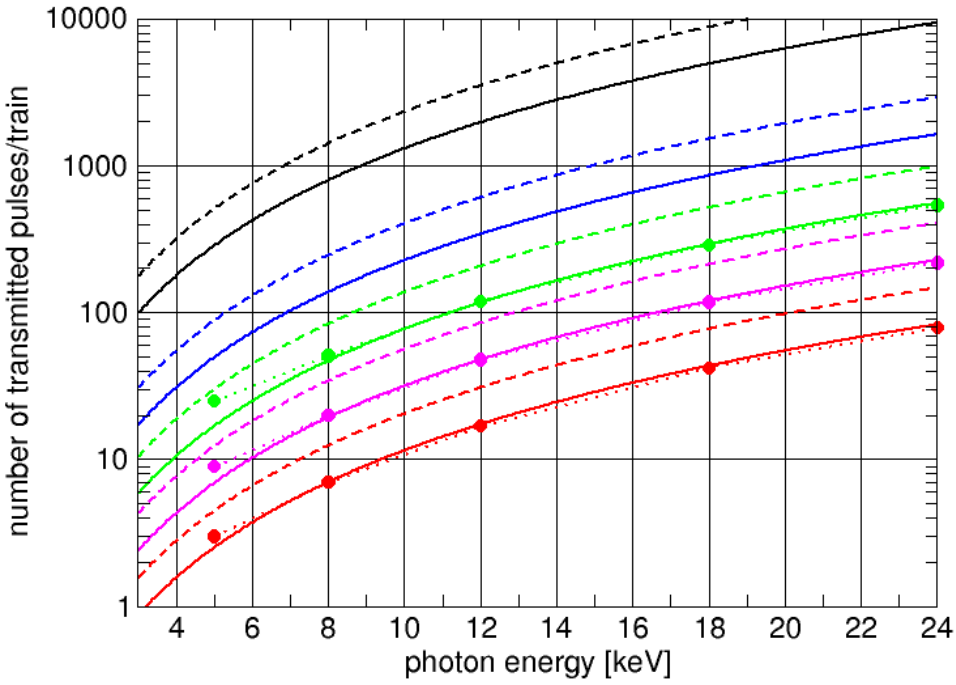


***Figure 44:*** *Transmitted pulses through a Si (111) monochromator at 850 m distance from the sample assuming no heat conduction during a pulse train. The solid lines correspond to 300K, the dashed lines to 100K base temperature. Colour scheme as in Figure 12. Circles are one-dimensional FEA simulations with heat transfer set to zero.*

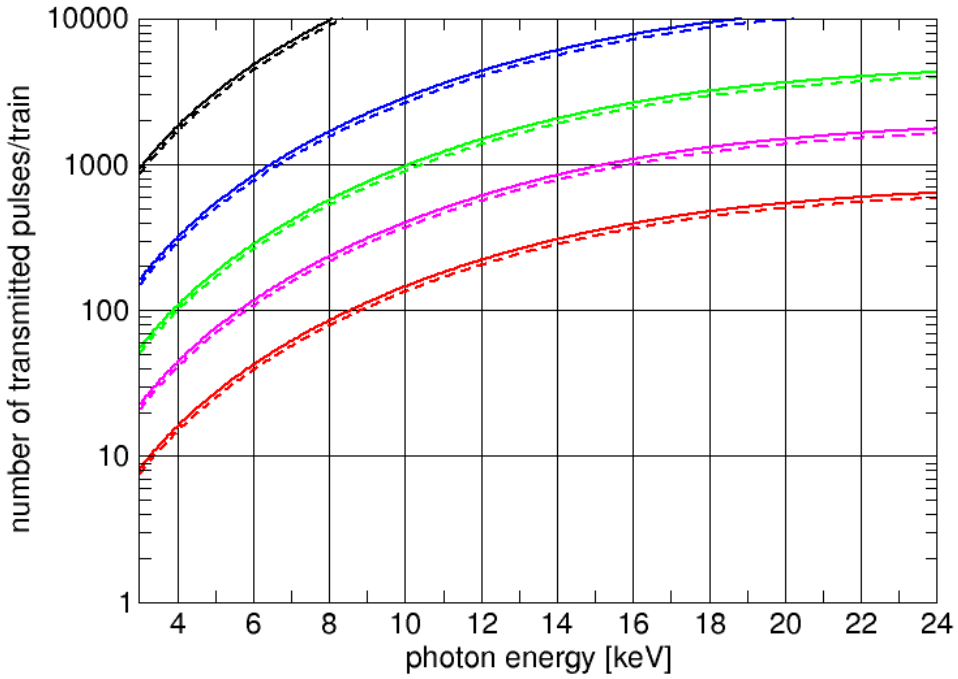


***Figure 45:*** *Transmitted pulses through diamond (111) monochromator without heat conduction during a pulse train. The solid lines correspond to 300 K, the dashed lines to 100 K base temperature. Colour scheme as in Figure 12.*

**Approximation of thermal transport:** One can approximate the thermal transport in one dimension along the strongest thermal gradient. In the case of a silicon Bragg monochromator, the strongest gradient is perpendicular to the surface into the bulk. The important length scale is the absorption length. For diamonds, since crystals are typically thin, the heat as to be removed to the edges of the crystal. The thermal gradient is on the length scale of the beam dimension and points in radial direction.

The decay of the peak temperature of a single Gaussian pulse with one-dimensional decay can be described as:

$$T(t) = T_0 \sqrt{\frac{t_0}{t_0 + t}} \tag{17}$$

with

$$t_0 = \frac{c_p \rho \, z_{abs}^2 \sin^2 \theta}{4\lambda}$$

For silicon, 300 K, $\lambda$ = 163.3 W/mK, $c_p$ = 0.7 J/gK, ρ = 2.33 g/cm$^3$. The characteristic time constant for the temperature decay is $t_0$ and it ranges from 21 ns (3 keV) to 45 µs (24 keV). For energies smaller than 7 keV, $t_0$ reaches the intra-pulse time scale (Si, 300 K) and thermal transport becomes relevant. For a diamond monochromator the term $z^2_{abs} \sin^2\theta$ has to be replaced by a characteristic length scale for the radial gradient (typically around 1 mm for an unfocused beam). With λ = 1 800 W/mK, $c_p$ = 0.51 J/gK, and ρ = 3.52 g/cm$^3$, one obtains 280 µs — too slow for significant heat removal during the pulse train. At 100 K the time constant reduced by to 2.8 µs, making thermal transport much faster. In silicon, the time constant decreases by a factor 20 when going from 300 K to 100 K.

An estimate for the effect of thermal transport can be given by the factor

$$S_{pulse} = \frac{1}{N_{pulse}} \sum_{n=0}^{N\_pulse} \sqrt{\frac{t_0}{t_0 + n \times 0.22\mu s}}, \tag{18}$$

which becomes 1 for large values of $t_0$ and less than 1 otherwise.

The number of pulses within a pulse train that would lead to detuning is then replaced by

$$N_{pulse} \rightarrow N_{pulse} / S_{pulse} \tag{19}$$

Results are shown in Figure 46 and Figure 47. The approximation of the thermal flow above estimates only the deviation from the initial temperature, rather than the complex development of temperature gradients at later times of the pulse train. The diamond Laue monochromator suggested in the European XFEL TDR 2006 [4] has, for example, a plateau in the temperature curve after the initial fast heat-up phase. This behaviour cannot be described in analytical model above, but by FEA methods.

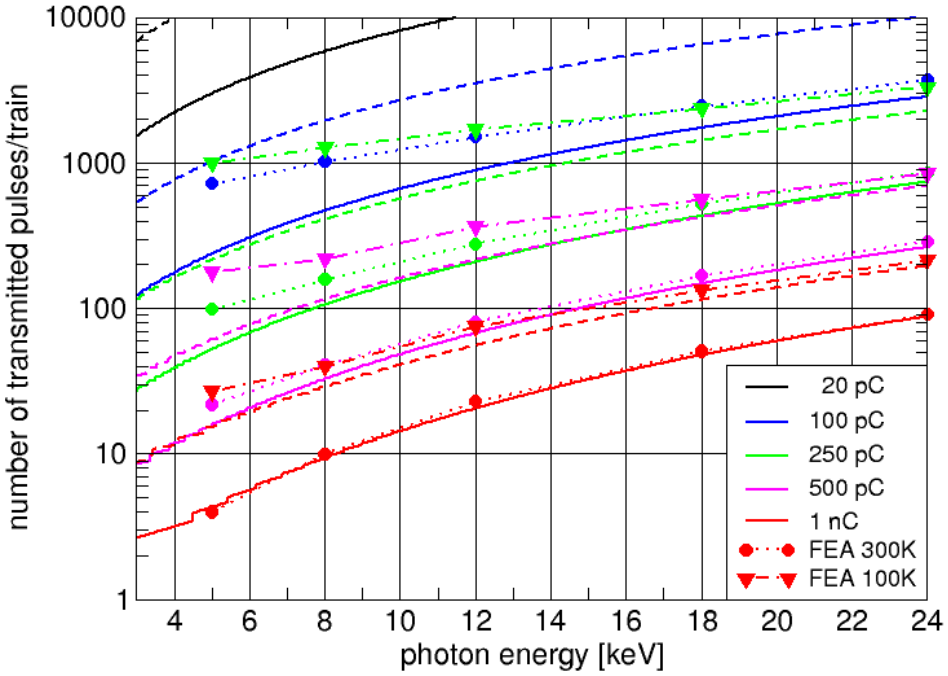


***Figure 46:*** *Number of transmitted pulses through a Si (111) monochromator including heat flow perpendicular to the surface. Solid lines are 300 K, dashed lines 100 K. Dots are FEA results at 300K, triangles FEA at 100 K.*

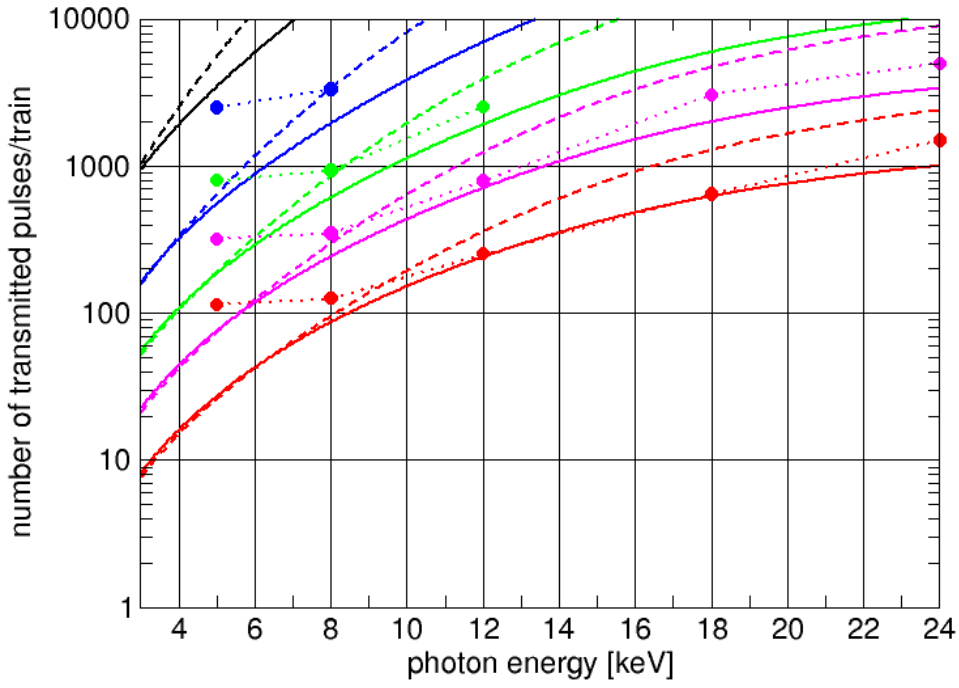


***Figure 47:*** *Number of transmitted photons for diamonds (111) in Laue geometry including radial heat flow. Solid lines are 300 K, dashed lines 100 K calculations.*

## One-dimensional FEA

An IDL code was developed for this analysis [7] that calculates pulse by pulse the heat-up of a monochromator crystal considering the variation of $c_p$ and $\lambda$ with temperature. The validity of the code was cross-checked with ANSYS FEA. The geometrical assumptions are the same as in the analytical model above; however, the FEA allows a time analysis of the temperature.

An example of such a calculation is shown in Figure 48.

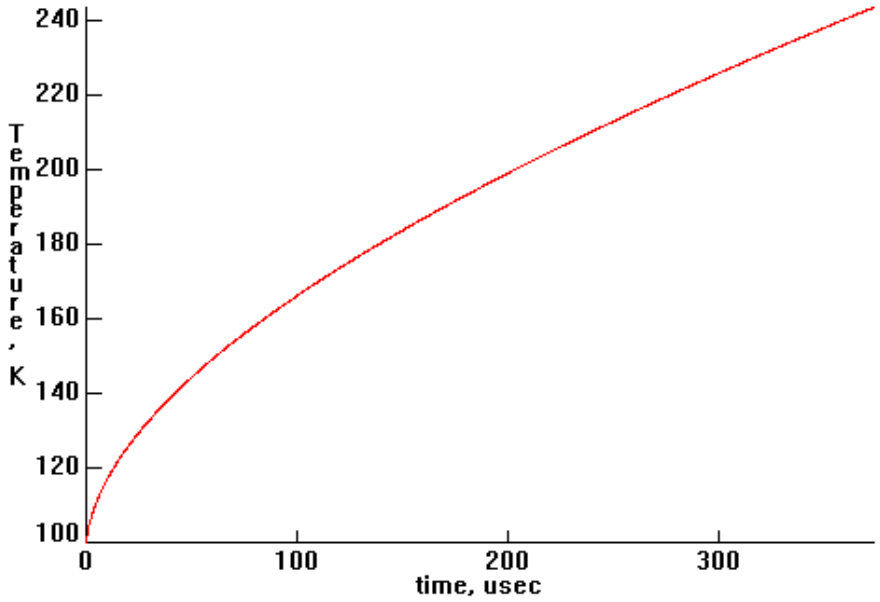


***Figure 48:*** *Example (Si, 100 K, 12 keV, 250 pC, 1 695 pulses) of peak temperature curve done with an IDL program*

Calculations with one-dimensional FEA were done for selected points and are shown in Figure 46 and Figure 47 as symbols.

## Silicon monochromator

A silicon monochromator could be built as a channel-cut to minimize vibrations. To enable high quality polishing for minimizing wavefront distortions, an artificial channel-cut could be used (for example as in a design developed by Argonne National Laboratories).

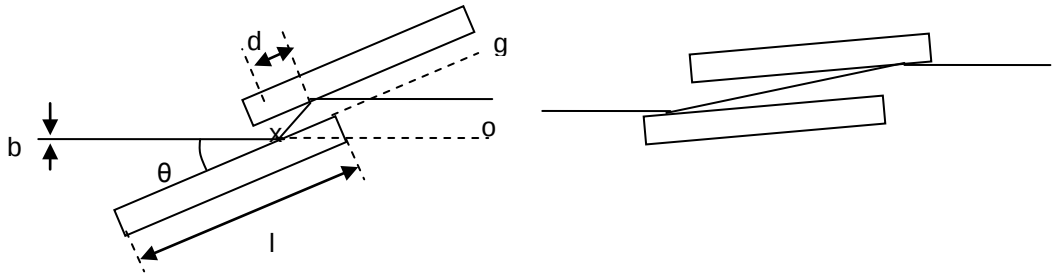


***Figure 49:*** *Channel-cut monochromator.* Left: *Low photon energy.* Right: *High photon energy.*

In the following, the geometrical parameters of a channel-cut as indicated in Figure 49 will be calculated.

The beam offset is

$$\sin 2\theta = \frac{o}{x},\ \sin\theta = \frac{g}{x} \Rightarrow o = 2g\cos\theta ,$$

The offset along the crystal surface:

$$d = \frac{g}{\tan\theta},$$

The minimum gap *g* depends on the maximum beam size and the maximum angle of incidence:

$$g_{\min} = \frac{b_{\max}}{2\cos\theta}$$

The maximum beam size at 3 keV and 850 m distance is 5.7 mm FWHM, 6 sigma = 14.6 mm. With a Bragg angle at 3 keV of 41.2°, the minimum offset would be 9.7 mm. For a minimum energy of 5 keV (3.7 mm FWHM, 6 sigma=9.4 mm, 23.29°) the minimum offset would be 5.2 mm.

The required length, *l,* of the crystals is given by the offset along the crystal for the highest desired photon energy and the footprint of that beam:

$$l_{\min} = \frac{d_{\max} - d_{\min}}{2} + \frac{b_{highE}}{\sin\theta_{\min}} = \frac{g}{2\tan\theta_{\min}} - \frac{g}{2\tan\theta_{\max}} + \frac{b_{highE}}{\sin\theta_{\min}}$$

For an upper energy of 24 keV, this yields (b = 1.15 mm, 6 sigma = 2.94 mm, 4.72°) 89 mm minimum length for 3–24 keV and 62 mm.

For the 3–24 keV channel cut, the offset would vary between 14.6 mm (3 keV) and 19.3 mm (24 keV), and for a reduced 5–24 keV band pass, between 9.55 mm and 10.36 mm.

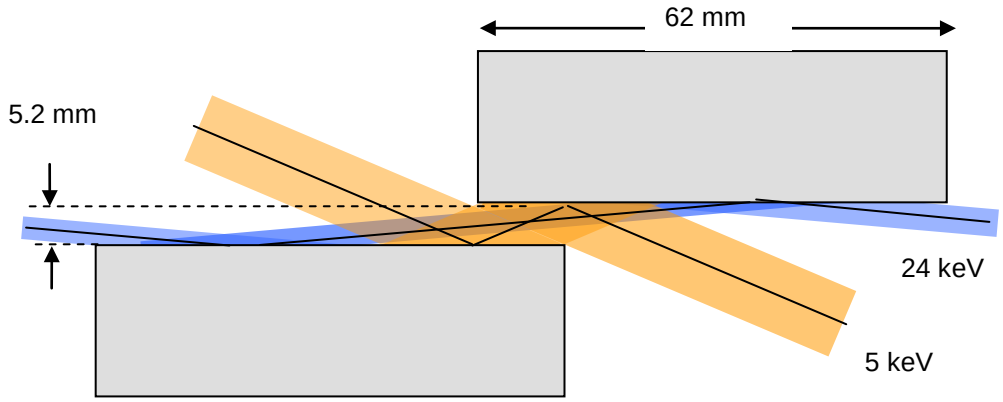


***Figure 50:*** *Conceptual design of Si (111) channel-cut for 5-24 keV*

The following table shows the crystal parameters used in the simulations. Simulations results for the silicon crystal are shown in Figure 44 and Figure 46 as symbols.

***Table 14:*** *Parameters for Si monochromator used in FEA analysis*

| **Si (111)** | **5 keV** | **8 keV** | **12 keV** | **18 keV** | **24 keV** |
|---|---|---|---|---|---|
| Abs. length | 17.8 | 67.9 | 221 | 721 | 1645 |
| Bragg angle | 23.29 | 14.31 | 9.48 | 6.31 | 4.72 |

## Diamond monochromator

A large HPHT-2a diamond could be for example 8 mm x 8 mm large and 0.5 mm thick, which would cover then typically the FWHM of the beam in Bragg geometry. The footprint on the crystal becomes then an ellipse, while the heat flow is still assumed to be radial (see Figure 51 and Figure 52).

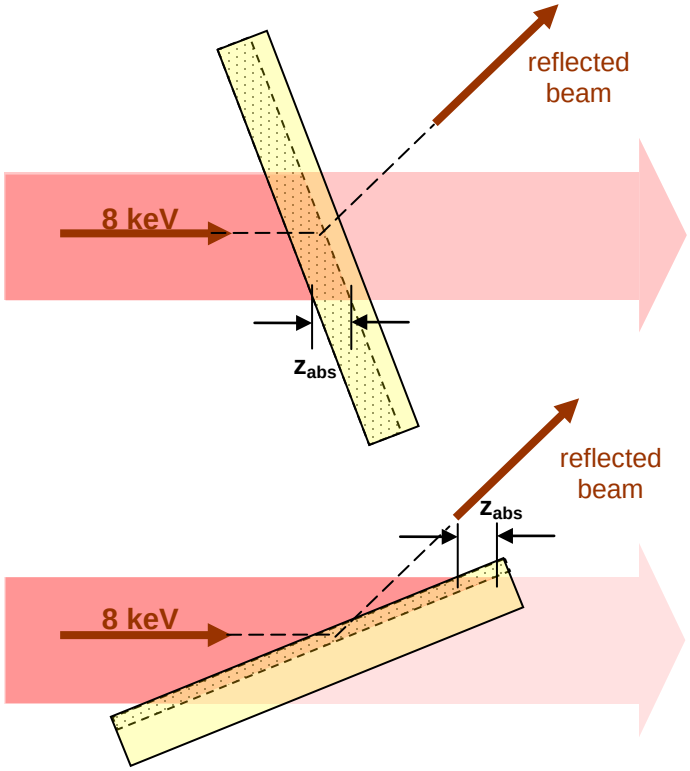


***Figure 51:*** *Diamond crystal in 8 keV beam.* Top: *Laue geometry.* Bottom: *Bragg geometry. The crystal shown in this example is 8 mm long and 1 mm thick.*

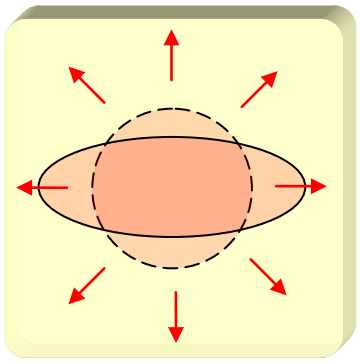

***Figure 52:*** *Diamond crystal, 8 mm x 8 mm, with 8 keV footprint in Bragg geometry (solid line). The dashed line circle shows the footprint assumed in the simulation. The arrows indicate the temperature gradient considered in the FEA.*

Therefore, a one-dimensional simulation is no longer correct; however, here we approximate the situation by setting:

$$\text{Bragg geometry}: \; z_{abs} \rightarrow z_{abs} \sin\theta \,, \quad b_{fwhm} \rightarrow \frac{b_{fwhm}}{\sqrt{\sin\theta}}$$

$$\text{Laue geometry}: \; z_{abs} \rightarrow z_{abs} \cos\theta \,, \quad b_{fwhm} \rightarrow \frac{b_{fwhm}}{\sqrt{\cos\theta}}$$

The beam parameters and crystal settings used for simulations are shown in Table 15. The FEA simulation results are shown in Figure 47 and in Table 16 and Table 17.

***Table 15:*** *Parameters of a Diamond (111) monochromator used in FEA simulations*

| **Energy** | **3 keV** | **5 keV** | **8 keV** | **12 keV** | **18 keV** | **24 keV** |
|---|---|---|---|---|---|---|
| Beam size fwhm | 5.44 mm | 3.52 mm | 2.36 mm | 1.67 mm | 1.19 mm | 0.92 mm |
| Absorption length | 33.5 µm | 158 µm | 653 µm | 2069 µm | 5359 µm | 8613 µm |
| 6 sigma | 13.86 mm | 8.97 mm | 6.01 mm | 4.25 mm | 3.03 mm | 2.34 mm |
| Bragg angle | -- | 37.01° | 22.10° | 14.52° | 9.62° | 7.20° |
| Footprint fwhm | -- | 5.8 mm | 6.2 mm | 6.7 mm | 7.1 mm | 7.3 mm |
| footprint 6 sigma | -- | 14.9 mm | 16.0 mm | 17.2 mm | 18.1 mm | 18.6 mm |

***Table 16****: FEA results on a Diamond (111) monochromator in Laue geometry. The crystal was in all simulations 500 micron thick. In intra-bunch spacing was 200 ns.*

| **C(111)** | **5 keV** | **8 keV** | **12 keV** | **18 keV** | **24 keV** |
|---|---|---|---|---|---|
| 1 nC | 115 | 127 | 255 | 648 | 1510 |
| 500 pC | 322 | 352 | 796 | 3 061 | 5 019 |
| 250 pC | 802 | 939 | 2 549 | | |
| 100 pC | 2 517 | 3 356 | | | |

***Table 17:*** *FEA results on Diamond (111) monochromator in Bragg geometry, 500 micron thick*

| **C(111)** | **5 keV** | **8 keV** | **12 keV** | **18 keV** | **24 keV** |
|---|---|---|---|---|---|
| 1 nC | 151 | 201 | 326 | 558 | 739 |
| 500 pC | 421 | 564 | 936 | 1 690 | 2 361 |
| 250 pC | 1 049 | 1 433 | 2 488 | | |
| 100 pC | 3 290 | 4 757 | | | |

A water-cooled Diamond monochromator in Bragg geometry would provide according to the FEA > 1 000 pulses up to 250 pC bunch charges. A crystal thickness > 500 micron would improve the pulse throughput for low energies.

For higher energies, the Laue geometry transmits more pulses. The crystal should be at least 8 mm long to cover the FWHM of the beam.

### Laue geometry

For the diamond Laue monochromator, a position more upstream in the beamline could be feasible, since the radial thermal flow does not change so dramatically with beam size as in the Bragg case. A major disadvantage is that the efficiency oscillates with photon energies on the keV scale due to Pendlelösung effects (Figure 53). This effect is less pronounced at high X-ray energies, and it could become a usable device experiments with spontaneous radiation (Figure 54). In that case, the monochromator has to be positioned before the beam collimator, so that the beam offset would be done by this monochromator instead of the offset mirrors (see Figure 4 in the conceptual of SASE2).

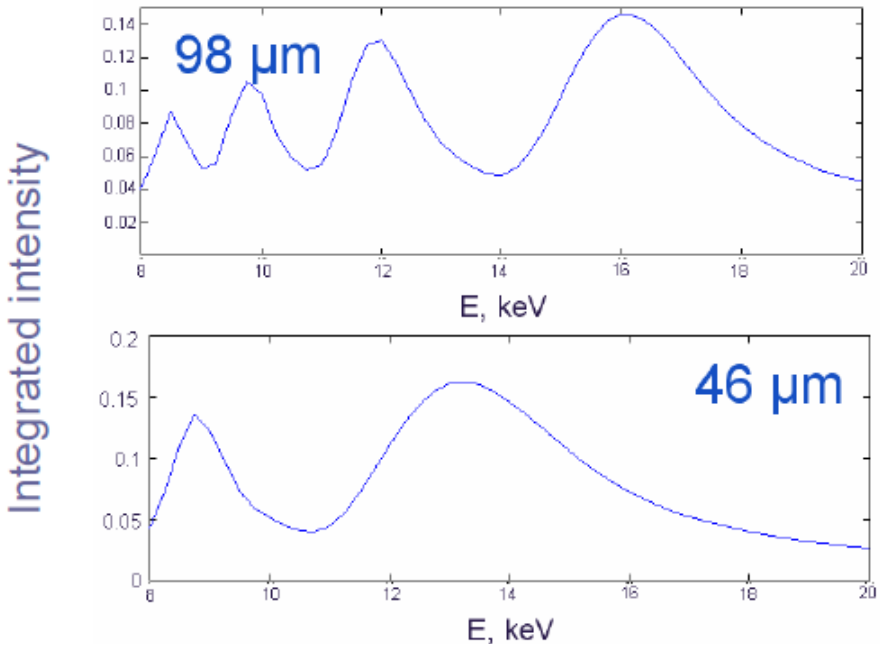


***Figure 53**: Intensity oscillations of a double Laue monochromator as a function of energy, for diamond crystal thicknesses of 98 μm and 46 μm, (220) reflection, monochromator at 500 m from the source. The integrated intensity was calculated by the width of Laue reflection, $\Delta E / E = |\chi_h| / \sin^2 \theta_B$, and normalized on the incident intensity. The Gaussian beam with constant waist size 70.5 μm FWHM was used to model beam divergences within the photon energy range. The monochromator efficiency (peak reflectivity) is 92% at 12.4 keV and 60% at 8 keV.*

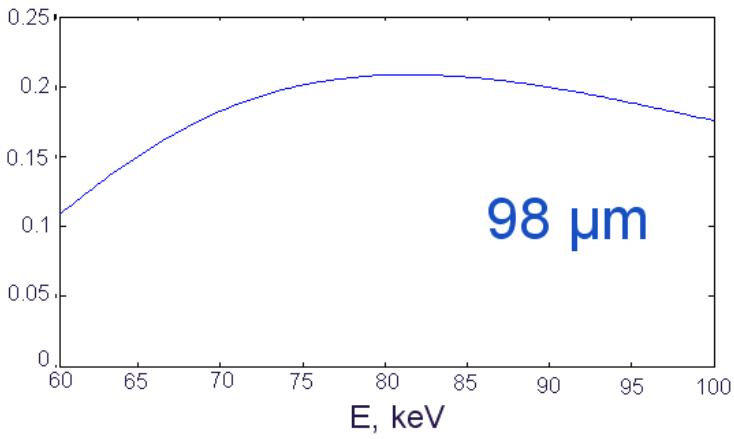


***Figure 54:** Intensity of Laue monochromator at high X-ray energies*

## Conclusion

The silicon monochromator operated at 100 K provides a solution with > 1 000 pulses per train for bunch charges up to 250 pC. For experiments that require short pulses of 30 fs and less, this could be an attractive solution. For higher bunch charges, one could for example widen the beam in the horizontal, but then the problem of refocusing becomes more severe. A water-cooled diamond monochromator shows in the simulations a similar pulse transmission. One attractive feature is that a diamond is—in contrast to any silicon mono—basically indestructible, at least in the unfocused beam. Crucial would be the availability of large and also thick diamond plates. The bandwidth of a diamond monochromator is a factor of 2 below the silicon (111), leading to a better resolution but also to less photons per pulse due to the reduced bandpass. The throughput of a water cooled diamond is similar to a 100 K silicon monochromator in the range of > 1 000 pulses per train.

The influence of heat bumps on the beam properties has still to be evaluated by FEA and beam propagation codes.

# KB mirrors

One of the challenges for focusing optics at the European XFEL is the large beam dimension in the experiment hall. While the beam can be prefocused or collimated in the horizontal direction with the offset or distribution mirrors, the vertical beam dimension cannot be manipulated. One possible solution for the hard X-ray range is the use of collimating CRL lenses, which is discussed in “Compound refractive lenses”. However, today it is not clear how well these lenses will work over many hundred meters with coherent beams. Below 5 keV, losses due to absorption and limitations due to heat load will become an issue. For hard X-rays, a pre-collimated beam will limit the number of transmitted pulses by a monochromator.

In this section, we assume the natural beam size enters the experiment areas and is then micro-focused be a KB system to a minimal focus size. As for the offset and distribution mirrors, we limit our considerations to 800 mm long mirrors, which we believe are feasible in the required highest possible optical quality.

### Hard X-ray beamlines

Similar to the concept of the offset mirrors, the idea is to adjust the incidence angle to the desired photon energy. In this way one can obtain a maximum transmitted beam cross section with a limited mirror length. For hard X-rays, the angle can be chosen close to the critical angle (Figure 55).

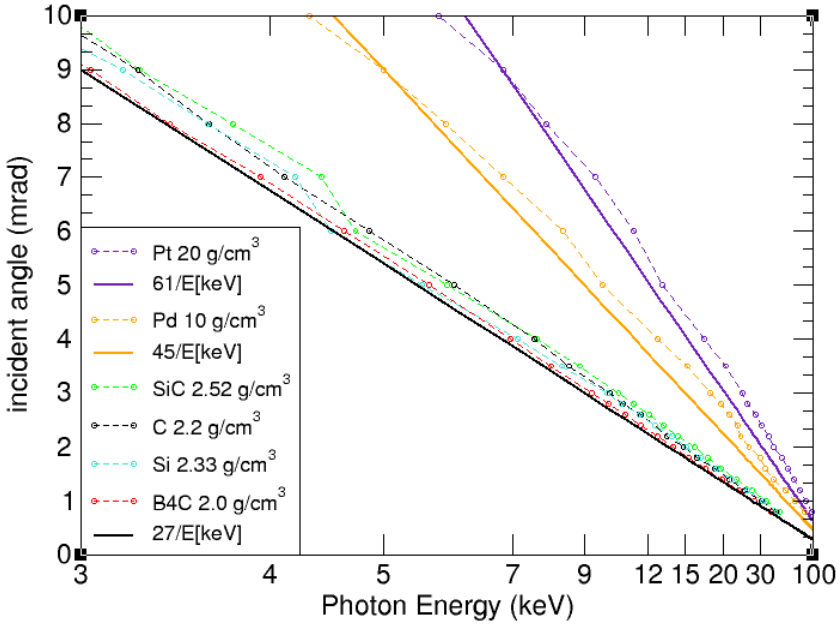


***Figure 55:*** *Critical angle for different materials*

Therefore, assuming the baseline approximations for divergence and incidence angles in the "Hard X-ray range" section of Chapter 5, "SASE beam properties", one can calculate required mirror lengths (*s = 4 sigma, C coating*) from

$$l_{mirror} = \frac{s\ D_{source}\ \delta\theta_{FWHM}}{2\sqrt{2\ln 2}\sin\theta}$$

$$\delta\theta_{fwhm}[\mu rad] = \frac{\left(17.2 - 6.4\sqrt{Q[nC]}\right)}{E[keV]^{085}} = \frac{16.3}{E[keV]^{0.85}}$$

$$\theta[\mathrm{mrad}] = \frac{27}{E[keV]} \quad \text{(for carbon coating)}$$

$$l_{mirror}[mm] = \frac{s\ D_{source}\ 16.3E}{2\sqrt{2\ln 2}\ 27\,E^{0.85}} = K\ D_{source}[m]\ E[keV]^{0.15}$$

with $K$ = 1.025 (C-coating), $K$ = 0.615 (Pd-coating), $K$ = 0.454 (Pt-coating).

For a KB setup at SASE1 with $D_{source}$ = 900 m, the required mirror lengths are shown in Table 18.

***Table 18**: Minimum mirror length (mm) for a vertical KB mirror that covers 4σ of the beam in the experimental hall for different coatings.*

| | 3 keV | 8 keV | 12 keV | 18 keV | 24 keV |
|---|---|---|---|---|---|
| C coating | 1 087 | 1 260 | 1 339 | 1 423 | 1 485 |
| Pd coating | 652 | 756 | 803 | 853 | 891 |
| Pt coating | 481 | 558 | 593 | 630 | 658 |

If one assumes a maximum feasible mirror length of 800 mm, it turns out that the KB mirrors have to be metal-coated. As in the discussion for the offset mirrors, the mirror lengths shown in Table 18 assume a retuning of reflection angles for all energies; otherwise, part of beam will be cut for lower energies or higher energies will not be reflected because the incidence angle is below the critical angle.

A possible conceptual layout for a KB system is shown in Figure 56. Two metal-coated 800 mm long mirrors are used in the vertical and the horizontal direction. The horizontal KB mirror is closer to the sample to get a better demagnification of the intermediate focus for the branch beamlines.

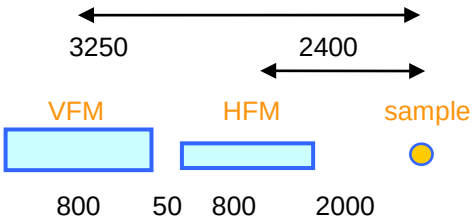


***Figure 56:** Possible layout for a KB mirror system. Distances are shown in mm.*

The smallest possible geometrical focus without slope errors in this configuration is about 110 nm (FWHM) in the horizontal and 150 nm in the vertical direction. With minimal slope errors assumed of 20 nrad rms for all beamline mirrors, the focus would reach about 250 nm in both directions. For the KB mirrors, which are likely to have adjustable bending radii, larger slope errors between 0.1–1.0 µrad are more realistic to assume. In this case the minimal focus from these mirrors would be in the range of 1–10 µm.

### Transmission and single shot damage

As pointed out above, an 800 mm long carbon coated KB mirror would be too short to transmit efficiently the beam (Figure 57).

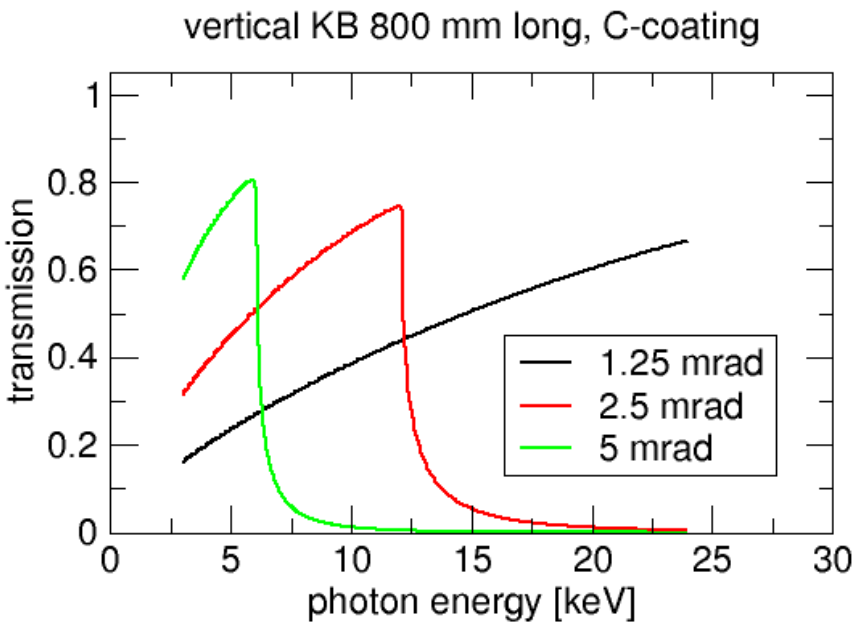


***Figure 57:*** *Transmission of 800 mm long C-coated vertical KB mirror*

For metal-coated KB mirrors, the transmission curves look much better (Figure 58 and Figure 59); however, for Pt-coated mirrors the L-absorption edges around 13 keV exclude the medium energy range.

Total transmissions and single shot damage potential are shown in Figure 60 and Figure 61. A reasonable working range with one setting of mirrors is about 5 keV wide. For the distribution mirrors (and also offset mirrors—not shown) the deposited energy per atom is below one 1 meV. The Pd-coated mirrors receive up to 10 meV per pulse; however, the effect of photo-electron cooling will reduce these numbers.

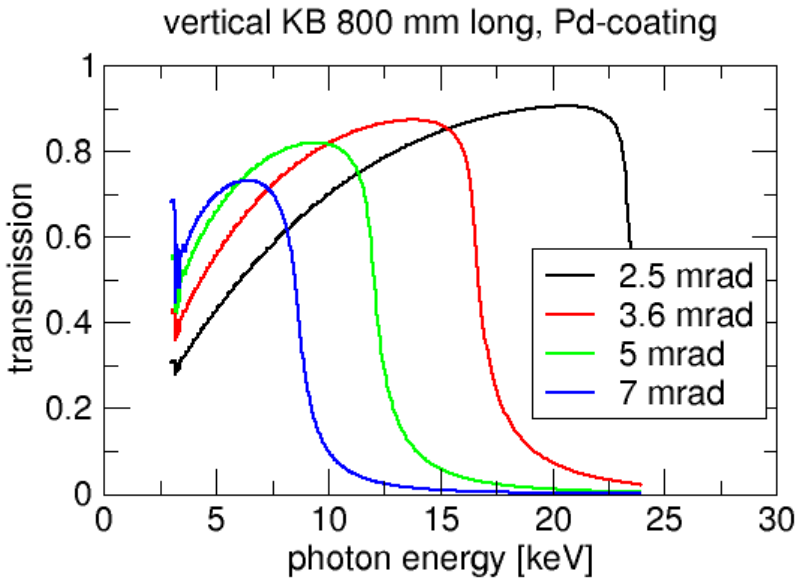


***Figure 58:*** *Transmission of vertical Pd-coated mirror*

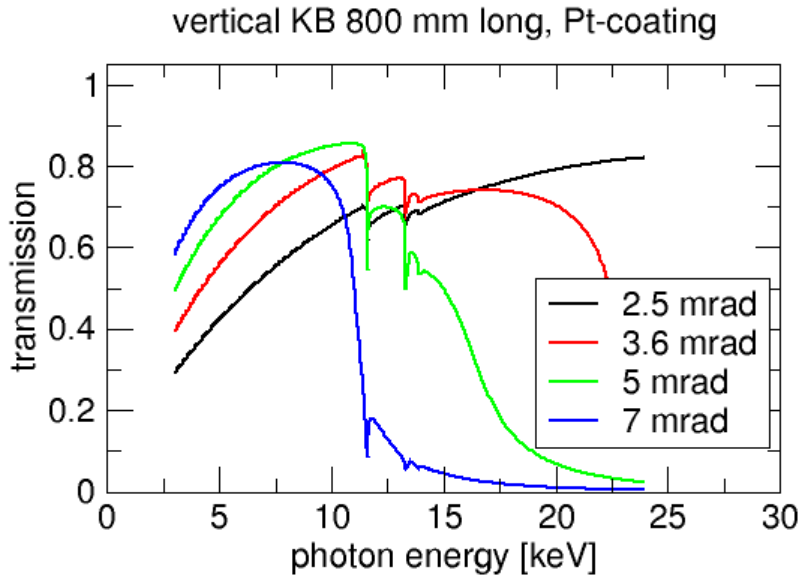


***Figure 59:*** *Transmission of vertical Pt-coated mirror*

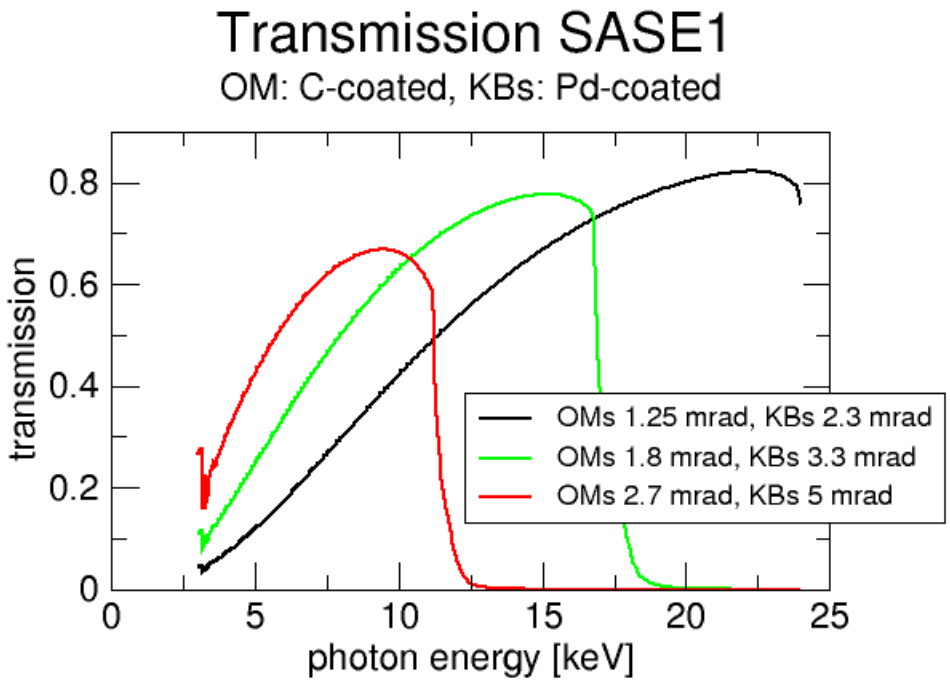


***Figure 60:*** *Total transmission for two C-coated offset mirrors and a Pd-coated KB pair. Three combinations of incidence angles are shown.*

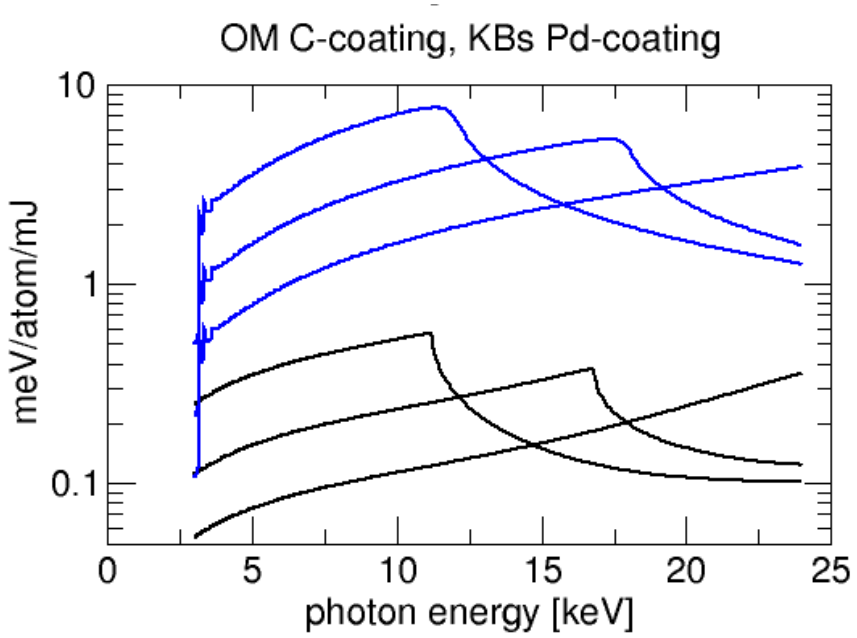


***Figure 61:*** *Deposited energy per atom for the offset and the KB mirrors in the above example. The black lines are for the offset mirrors, the blue lines for the Pd-coated KB mirrors.*

## Soft X-ray beamlines

Similar to the concept in Figure 56, a KB system is now investigated for the soft X-ray beamlines. In contrast to the hard X-ray beamlines, where the use of monochromators is in conflict with the concept of early beam collimation, at the soft X-ray beamlines, a prefocusing with offset or distribution mirrors can be used to control the horizontal beam size at the experiments. For SCS and also for SQS2, the beam will have an intermediate focus close to the end of the tunnel in order to match the footprint on the PGM or distribution mirrors. In this case, the horizontal beam size at the experiment will be also much smaller than the vertical size, which will lead to constraints from the single shot damage. Due to the much closer source point, the geometrical demagnification will limit the achievable horizontal focal size. Since the floor plan for experiments is not fixed yet, it is here assumed here that the horizontal KB mirror will be 20 m downstream of the intermediate focus. Metallic coating cannot be used except for Ni around the C-edge at low pulse energies. Therefore, the coating is assumed to be amorphous carbon, boron, or $B_4C$.

With geometrical setting as in Figure 56, the minimum geometrical focus size would be between 300 and 500 nm, depending on the photon source size for different energies. At SQS, the theoretical limit would be similar as in the horizontal direction, however, by collimating the beam at the second offset mirror, the horizontal KB mirror could be made shorter and brought closer to the sample to obtain a minimal focal size. For SCS and SQS2 at 20 distance from the intermediate focus and 2.4 m distance to the sample, the horizontal geometrical minimum focus size is 3–5 µm. In particular for SCS, this horizontal beam size would widen if the exit slit is opened to allow more flux. Due to the smaller beam size, a 300 mm long mirror would be sufficient in the horizontal direction for SCS and SQS2.

Similar to the hard X-ray case, slope errors between 0.1–1 µrad on the soft X-ray KB mirrors would increase the focal size by 1–10 microns.

## Transmission and single shot damage

In the following, figures the transmission through the vertical KB mirror alone (Figure 62), the horizontal mirror alone (Figure 63), and the two KB mirrors, including two offset mirrors (Figure 64), are shown. At the vertical KB, incidence angles larger than 15 mrad do not increase the throughput at low energies since the larger beam acceptance is compensated by a smaller reflectivity. A similar effect is observed for the offset mirrors above 9 mrad. Therefore, for energies up to 2 keV, the offset and KB mirrors can be run efficiently at a single angle setting shown in Figure 64. For higher energies, the vertical KB mirror would have to change the incidence angle to 9 mrad. In Figure 65, the transmission at low energies with different coatings and incidence angles is shown.

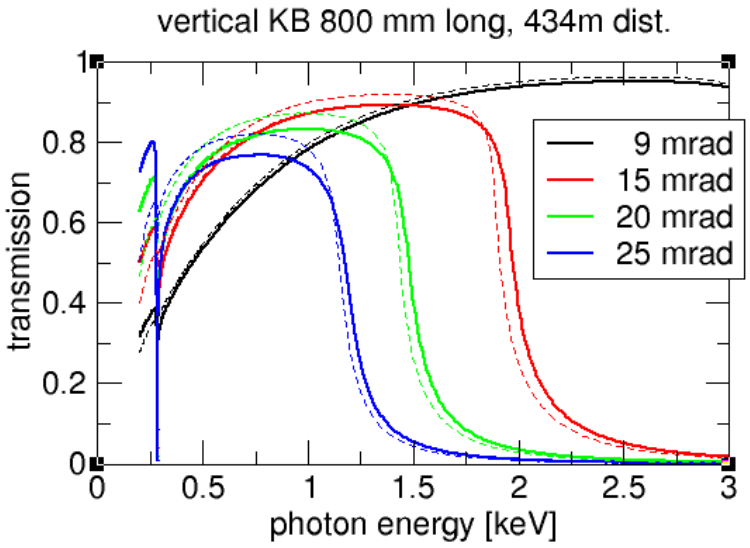


***Figure 62:*** *Transmission of 800 mm long vertical KB mirror alone for different incidence angles. The solid lines are for C coating, the dashed lines for $B_4C$ coating.*

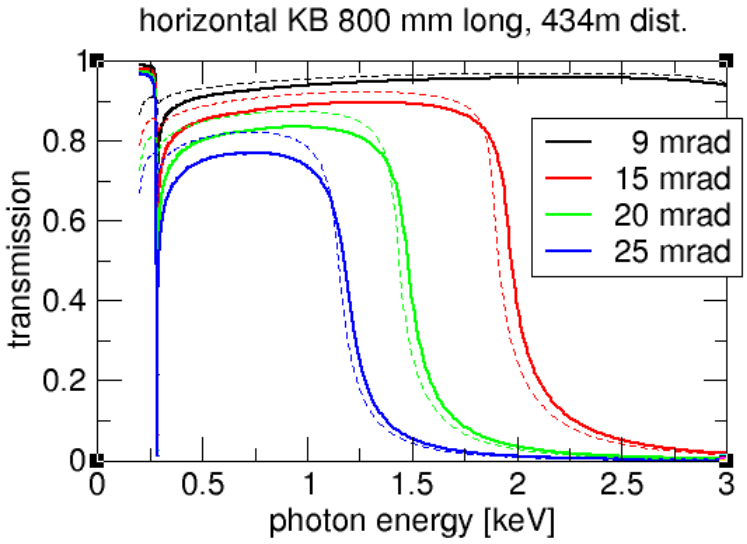


***Figure 63:*** *Transmission of horizontal KB mirror alone. The assumption is that geometrical cut-off can be avoided by prefocusing by the second offset mirror. Only reflectivity reduces transmission.*

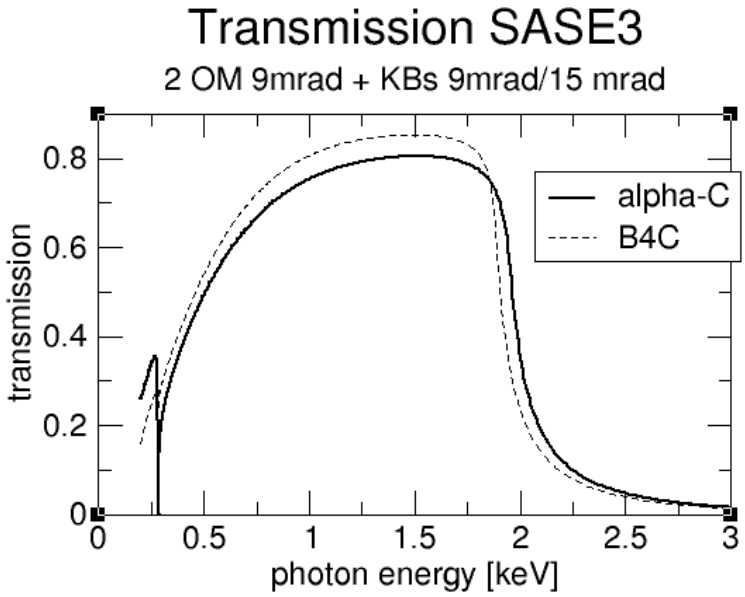


***Figure 64****: Total transmission of two offset mirrors at 9 mrad, a vertical KB at 15 mrad, and a horizontal KB at 9 mrad. The solid line indicates C coating, the dashed line $B_4C$ coating for all mirrors. Roughness was not included in these calculations.*

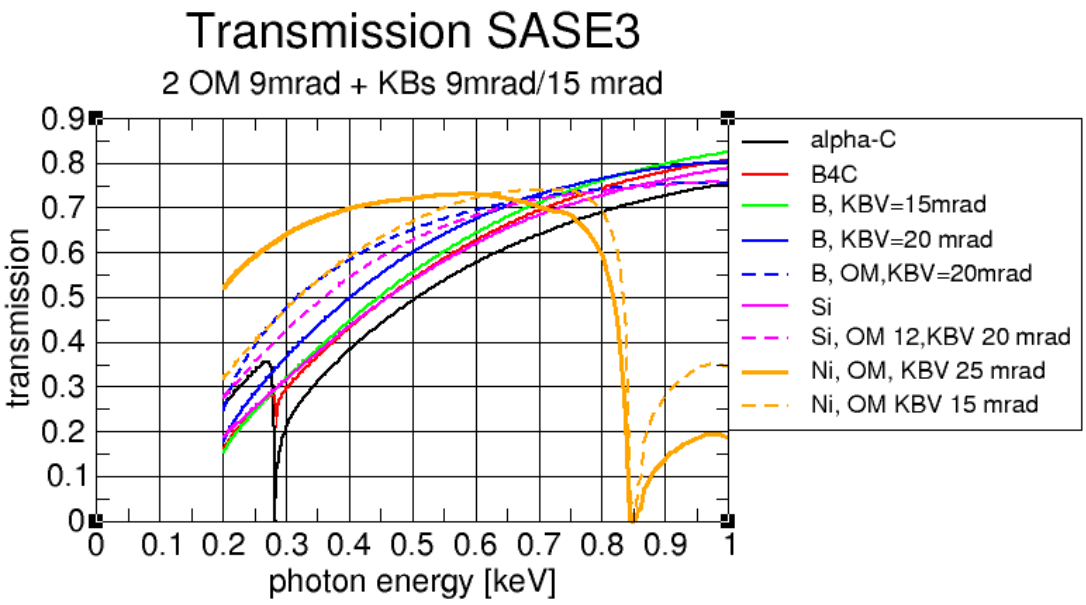


***Figure 65:*** *Total transmission for low energies with different coating and incidence angles. Nickel coating on all mirrors would increase the efficiency below 500 eV, but would be limited to low pulse energies.*

For calculating the damage potential of the FEL beam for the optics, the lower calculated beam divergence in Equation (1) was used. The method for calculating the damage is explained in Appendix A, “Damage calculations”. All deposited energies were calculated in meV per atom and per 1 mJ pulse energy. For 10 mJ pulses, for example, the values have to be multiplied therefore by 10. It is currently not precisely known, how much energy per atom can be absorbed before permanent damage occurs. For high melting solids, an upper boundary is about 1 eV, which corresponds to bulk melting. For thin layers, damage of carbon has been observed for 100 meV/atom in a single shot. Considering also fatigue effects, we currently guess the damage threshold to be around 30 meV/atom for thin layers of carbon; however, this value might be different under real conditions.

In the damage calculations below, all transmissions of upstream elements are set to one for sake of simplicity. Heat transport by photoelectrons is not considered here, but should lower deposited energies a bit for the higher photon energies.

As shown in Figure 66, offset mirrors and distribution mirror at 9 mrad will receive below 4 meV/(atom mJ), from which we conclude that operation up to 10 mJ per pulse should be possible. As long as the beam is divergent or collimated (solid or dashed lines), the situation is similar for the two KB mirrors. For the situation with an intermediate focus near the tunnel end (dotted lines, SCS zero order beam, and SQS2), the deposited energies are more than 10 times higher, because the horizontal beam size is by that amount smaller. In this situation, the maximal energy per pulse has to be restricted to 1 mJ. For SQS2, one option to avoid this limitation would be to bend the distribution mirror strongly convex to -3.5 km or position the intermediate focus in front of the distribution mirror to restore the natural beam size in the experimental station. Another option would be to use a toroidal mirror with a small grazing incidence angle.

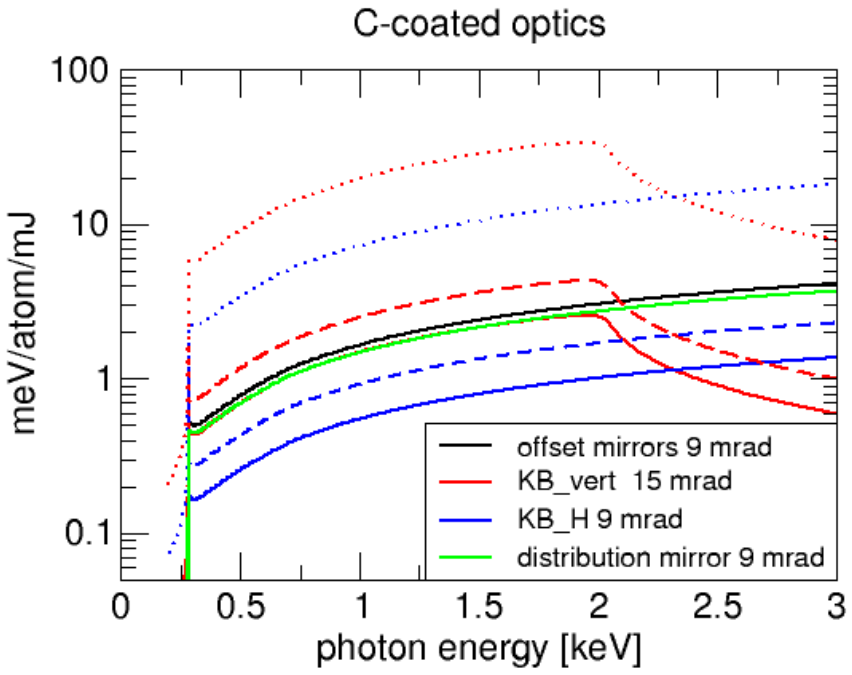


***Figure 66:*** *Single-shot damage potential on carbon coated SASE3 mirrors for pulse energies of 1 mJ. The dashed lines represent the KB mirrors, when the beam is collimated at the offset mirror. The dotted lines show the case of intermediate focus at the end of the tunnel.*

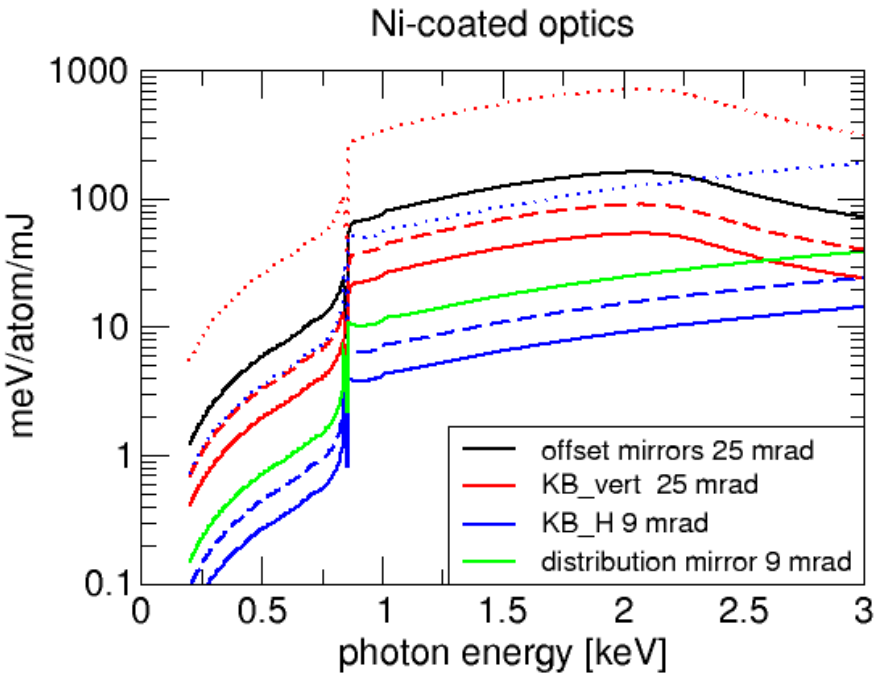


***Figure 67:*** *Single-shot damage potential for nickel-coated optics and steeper incidence angles. Dashed and dotted lines as above.*

## Conclusion

We have shown that—with certain compromises regarding the throughput—it is possible to use large KB mirrors (800 mm long) as micro-focusing optics on all beamlines. However, to collect the large vertical beam size at SASE1 and SASE2, metallic coating is required, which is a factor of 10 closer to the single damage threshold than carbon coating. If one would like to explore also the possibility of prefocusing for example by CRLs, it might be a good idea to add a strip of diamond-like carbon coating on each KB mirror, if technically feasible. As for the distribution mirrors, angular re-adjustment of the incidence angles for different energies seem necessary, which has to be taken into account in the design of the instrument.

At SASE3, also the vertical beam size is the limiting factor. Due to the required steeper angle of the vertical KB mirror, single shot damage can become an issue for high pulse energies. The coating of SASE3 mirrors with boron instead of carbon is one option which is currently being explored. The damage resistance it is similar as carbon; however, it would offer the capability to work exactly at the carbon edge.

An option to improve performance or flexibility would be to increase the mirror lengths. The high quality profile error derived for the offset and distribution mirrors is for the KB mirrors only necessary, if conditions close to the diffraction limit are targeted. If focusing requirements can be more relaxed, one could use, for example, 1.2 m long KB mirrors and increase either tunability or damage tolerance.

On the other hand, if focusing of 100 nm or better is desired, the concept of adjusting the incidence angle might be a problem since it implies changing the curvature of the mirrors. With fixed radius (and probably shorter) very high-quality KB mirrors, a pre-collimation of the beam will be required. For the optimization, it would become then crucial to have better data on damage thresholds of different coating under grazing incidence geometry for the desired energy range. In particular for hard X-rays, a higher radiation tolerance due to electron-cooling effects can be speculated.

## Compound refractive lenses

Compound refractive lenses (CRLs) are used at Synchrotron and XFEL sources for focusing of hard X-rays. Their advantages are in-line geometry (no beam deflection), ease of use and alignment, and insensitivity to angular vibrations. Disadvantages are the chromaticity, a significant small angle scattering background (Be CRLs), and limited apertures or small transmissions with large beams. Their potential use for the European XFEL is investigated in this section.

One way in which CRLs could be used is in the upstream part of the beamlines as a collimating element or focusing element with very long focal length (Figure 68). A horizontal lens could collimate or focus the beam towards the distribution mirror, so that an active bending of the second offset mirror would be no longer required. If the lens is focusing in the vertical direction, it could be used to reduce beam sizes in the experiment hall, which would increase the performance of KB mirrors at the sample.

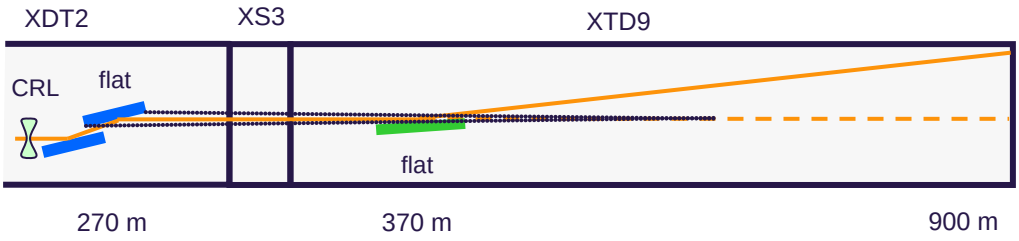


***Figure 68:*** *Beam offset and distribution scheme. Prefocusing is done by a Be CRL. No active mirror bending would be required.*

Since the focusing is very weak, only one lens would be need for a particular energy. For example, at 10 keV a single Be lens with 1.24 mm bending radius would be required to collimate the beam (Figure 69). The effective aperture of the lens is 1.6 mm and the beam size at this position for 10 keV only 0.6 mm; the transmission is very close to one (assuming 50 µm thick intermediate walls as for all calculations below).

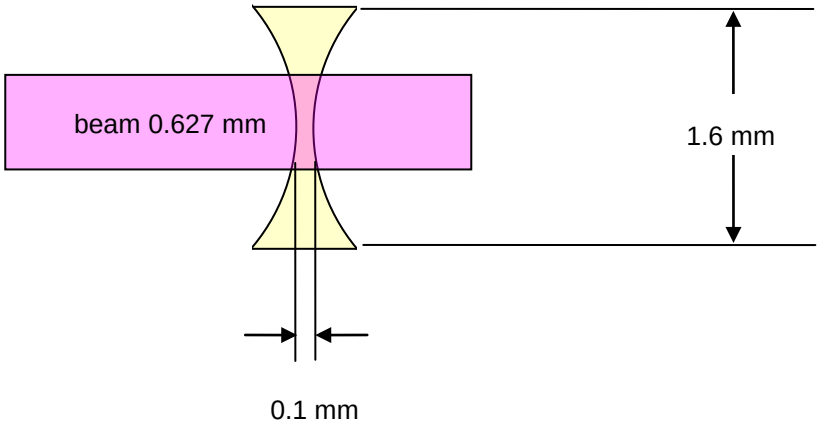


***Figure 69:*** *Sketch of a Be lens for collimation of a 10 keV beam 250 eV downstream of the source point R = 1.24 mm.*

The parameters and number of such lenses can be optimized and calculated precisely for every photon energy and focusing distance [8], [9], and [10]. Figure 70 shows the optimized transmission, when the focal point is assumed to be in the experiment station. For energies up to 5 keV, a single lens was

assumed for all energies; for higher energies, the number of lenses is varying between one at 250 m to 5–20 at 860 m and more lenses for distances closer to the sample. The more upstream the lens is positioned, the higher the transmission. For energies below 6 keV, the transmission drops significantly because the absorption in the beryllium increases. Also, after 860 m from the source point, the transmission decreases sharply, in part because the increased beam size, but more significantly because more and more lenses are needed to achieve a focus at the sample position, here assumed at 910 m (see also inset of Figure 70). Therefore, a micro-focusing setup with Be CRL lenses close to the sample location without any pre-collimation of the beam will be quite inefficient.

In Figure 71 the corresponding calculations are shown for diamond based lenses. The results are qualitatively the same, but the efficiencies are lower due to the higher photo-absorption.

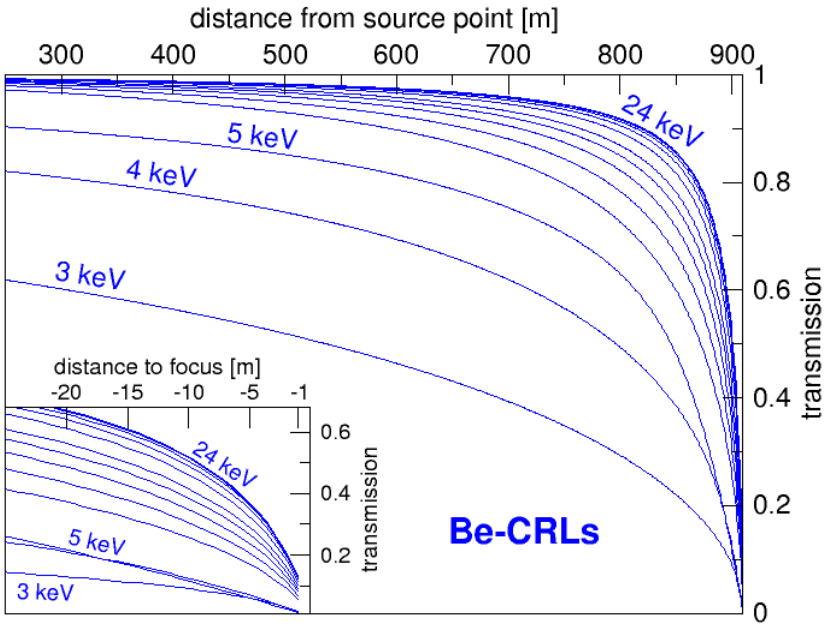


***Figure 70:*** *Maximum throughput for Be CRLs focusing to sample position at 910 m. Up to 5 keV calculations were done for a single lens.*

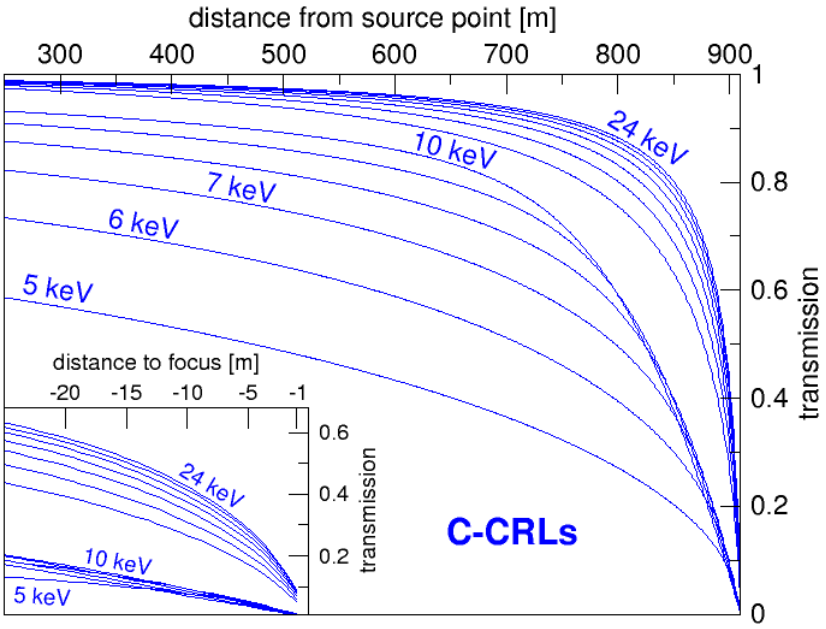


***Figure 71:*** *Maximum throughput for C CRLs. Up to 10 keV, calculations were done for a single lens.*

Another important question concerns the tunability of the lenses or lens arrays. For the upstream position (250m), the required radii of single Be lenses are shown in Figure 72 for two different cases: focusing to the experiment station (black) and collimation of the beam (red).

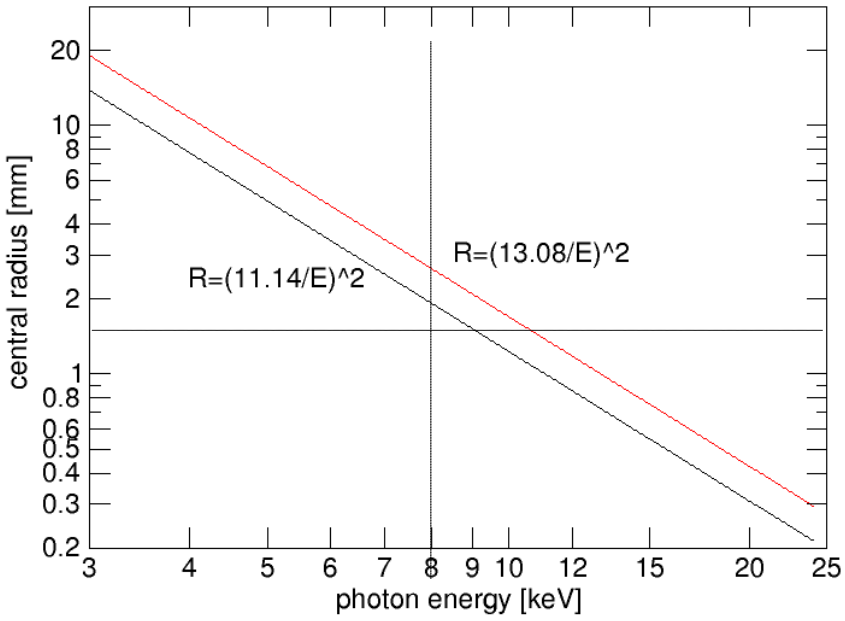


***Figure 72:*** *Radii of Be lenses with a single element 250 m downstream of the source. The radii in the upper curve are collimating the beam; the lower radii focus the beam to the experiment hall. The dotted lines indicate a 2 mm radius lens.*

For 10 keV, the geometrically limited focus would be around 130 µm, the collimated beam around 600 µm. Because of distortions in the lens and the offset mirrors, the difference is likely to be much smaller. Therefore, it is assumed here that one lens would be sufficient to cover the corresponding energy range between focusing and collimation condition.

With that assumption the bandwidth of a single lens can be estimated from Figure 72 as

$$\frac{\Delta E}{E} = 17\,\%$$

Below 8 keV, the radii of required lenses exceed 2 mm, which will be very difficult to achieve for manufacturing reasons. The range between 8 and 24 keV could be then covered with seven individual lenses with radii between 0.3 and 2 mm or even less, if lens combinations are used for the higher energies.

If a lens array is positioned 50 m before the focusing position (behind the monochromator) 5–20 lenses with similar radii of around 1.5 mm are required.

In this configuration, best foci between 4 and 50 µm can be expected at the sample location, depending on the quality of the lenses. The transmission should be around 65% for 8 keV and up to 80% for higher energies.

## Heat load considerations

The heat deposited in a CRL in one X-ray pulse will not be removed during the pulse train, but rather in the time between pulse trains. The reason is that the thermal gradient will be only in radial direction following the beam profile. The characteristic time constant for thermal transport is

$$t_0 = \frac{c_p \rho \, b_{hwhm}^2}{4\lambda}$$

with $\rho$ = 1.84 g/cm³, $cp$ = 1.82 J/gK, $\lambda$ = 2.01 W/cmK, $b$ = 0.1 cm the time constant $t_0$ = 4 ms, longer than the pulse train of 0.6 ms.

Since beryllium starts to soften around 500°C, the maximum acceptable temperature increase during one pulse train is chosen here to be 300 K (80 meV/atom). With all absorbed heat remaining in the Be during the pulse train, the maximum number of acceptable pulses of 1 mJ is shown in Figure 73. The red area shows the 250 m position for high and low beam divergences and the blue area the corresponding values for the position at 860 m from the source. If one limits the range to above 8 keV, damage through heat-load effects might occur for pulse trains longer than 1 000 pulses or higher than 1J integrated pulse train energy. Well-designed water cooling is required to remove the heat in between pulse trains. At 860 m, the Be CRLs are in safer operation conditions however, focusing onto the lenses by the offset or distribution mirrors has to be avoided.

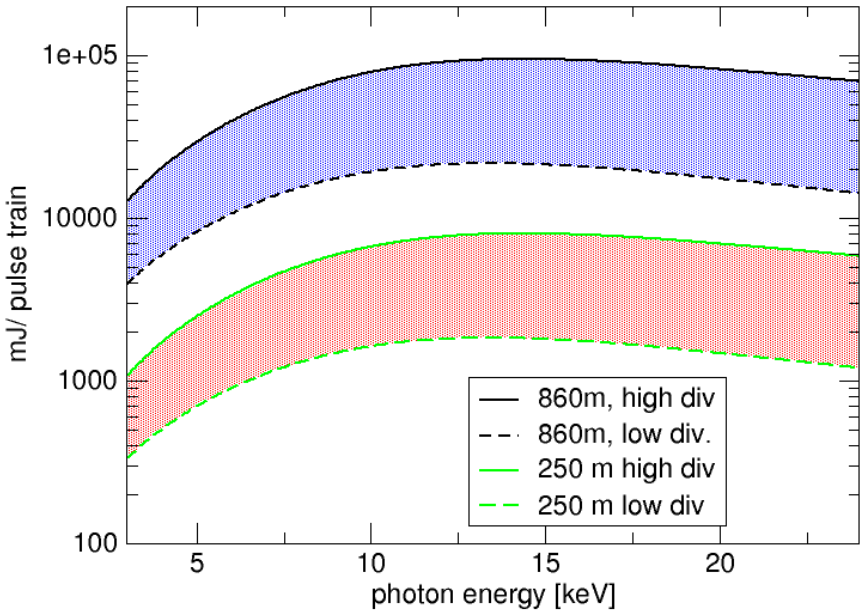


***Figure 73:*** *Tolerable pulses per train for a Be lens at 860m (blue) and 250m (red). The solid curves were calculated using the upper curve in Figure 1 and the dashed curves refer to the lower divergence approximation. The thermal energy per atom will be 80 meV after the calculated number of pulses.*

## Conclusion

Be CRLs seem to be an attractive solutions for photon energies > 8 keV, either close to the source (250 m) or 50 m in front of the sample (860 m). They offer in particular the possibility of beam collimation in the vertical direction, which is not possible by the horizontally reflecting mirrors. With the current design parameters of the machine it is likely to damage the Be CRLs at the 250 m position with pulse trains of more than 1J integrated energy.

A collimation before a monochromator would reduce the number of transmitted pulses through the monochromator, so the use of lenses has to be evaluated for each experiment.

# 7 Wavefront simulations

The first—and mandatory, for safety reasons—optical elements of the photon transport system are offset mirrors.

The following factors have impact on wavefront quality [11]:

- For a given incidence angle, the mirrors are too short to accept the full XFEL footprint, which leads to diffraction on mirror edges. How strong the effect is depends on the wavelength, the angular divergence, and the ratio between source-to-mirror and mirror-to-experiment-station distances.
- Residual height errors, that is, deviation of the mirror surface from the ideal shape.

The impact of diffraction on mirror edges can be estimated with Fresnel number for the aperture

$$w = L \sin\theta_{inc} = m_\sigma \sigma \approx m_\sigma (z_1 \delta\theta_{fwhm})/2.35$$

$$NF = w^2/(4\lambda z)$$

where $L$ is the mirror length, $\theta_{inc}$ is incidence angle, $\sigma$ is sigma rms of the beam at the mirror position, $z = z_1 z_2/(z_1+z_2)$, $z_1$, $z_2$ distance from the source to the mirror and from mirror to the station correspondingly. The diffraction effect is noticeable for footprints of $4\sigma$ or less. If NF~1, the intensity distribution will be a Fresnel diffraction pattern with well-pronounced minima and maxima, whereas NF<<1 corresponds to Fraunhofer (far field) diffraction, and NF>>1 corresponds to the region of geometrical shadow. For SASE1 and SASE2 wavelengths and the optical layout, a 4 $\sigma$ beam footprint always correspond to Fresnel diffraction region (Figure 74).

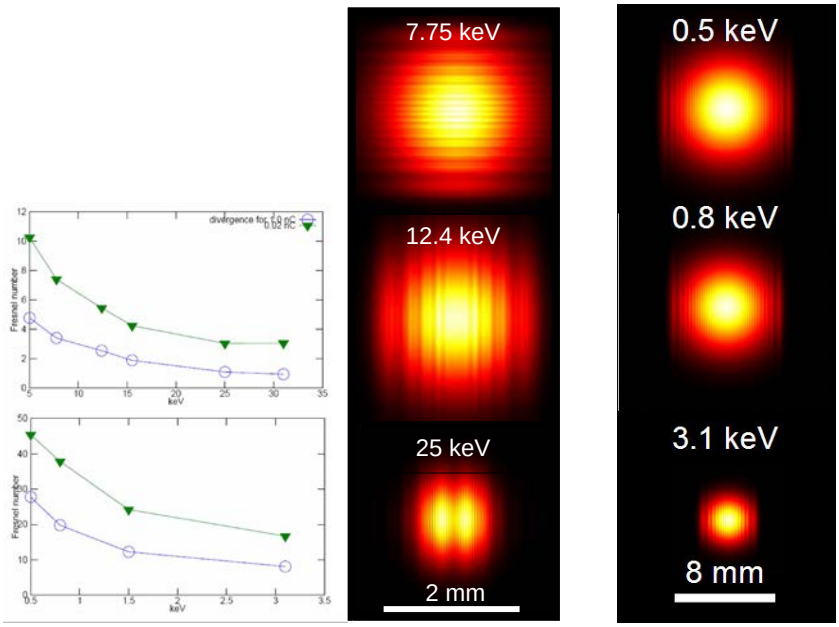


***Figure 74:*** Left: *Fresnel number for a 4σ footprint on the offset mirrors.* Right: *Wave front propagation simulations of the diffraction on the 4σ aperture at the experiment station distance for SASE1 (left) and SASE3 (right). The angular divergence corresponds to 0.02 nC bunch charge.*

Acceptable peak to valley (PV) height errors can be defined from Marechal criteria [12], taking into account the maximal optical path difference $2h_{pv} \sin \theta_{inc}$:

$$n = \lambda/(2h_{pv} \sin \theta_{inc}), \quad n \geq 14$$

Table 19 and Table 20 show the wavefront distortions from profile errors according to the Marechal criteria for different operation conditions at SASE1–3.

***Table 19:*** *Footprint and wavefront distortions for assumed profile error 2 nm PV and 800 mm mirror length at SASE1 and SASE2*

| Photon-energy [keV] | $\theta_{inc}$ [mrad] | FP* | WF dist. | $\theta_{inc}$ [mrad] | FP* | WF dist. | θinc [mrad] | FP* | WF dist. |
|---|---|---|---|---|---|---|---|---|---|
| 5 | 2.5 | 4σ | λ/16 | 2.8 | 4.5σ | λ/14.5 | 3.8 | 6σ | λ/11 |
| 8 | 1.7 | 4σ | λ/15.6 | 1.9 | 4.5σ | λ/14 | 2.6 | 6σ | λ/10 |
| 12.4 | 1.2 | 4σ | λ/14 | 1.3 | 4.5σ | λ/12.5 | 1.8 | 6σ | λ/9.5 |
| 15.5 | 0.9 | 4σ | λ/14 | 1 | 4.5σ | λ/12 | 1.4 | 6σ | λ/9.5 |
| 25 | 0.77 | 5σ | λ/10 | 0.92 | 6σ | λ/9 | 1.2 | 8σ | λ/6.7 |
| 30 | 0.7 | 5σ | λ/11 | 0.83 | 6σ | λ/8 | 1.1 | 8σ | λ/6 |

* **FP**=footprint. Divergences are calculated for the bunch charge 0.02 nC

***Table 20:*** *Footprint and wavefront distortions for assumed profile error 3 nm PV and 800 mm mirror length at SASE3*

| Photon-energy [keV] | $\theta_{inc}$ [mrad] | FP* | WF dist. | $\theta_{inc}$ [mrad] | FP* | WF dist. | $\theta_{inc}$ [mrad] | FP* | WF dist. |
|---|---|---|---|---|---|---|---|---|---|
| 0.3 | 9 | 2σ | λ/74 | 15 | 3.3σ | λ/44 | 20 | 4.5σ | λ/33 |
| 0.5 | 9 | 3σ | λ/46 | 15 | 5σ | λ/28 | 20 | 6.7σ | λ/20 |
| 0.8 | 9 | 3.8σ | λ/20 | 15 | 6.4σ | λ/16 | 20 | 8.3σ | λ/8 |
| 1.5 | 6 | 4.6σ | λ/22 | 9 | 7σ | λ/16 | | | |
| 3.1 | 6 | 6.5σ | λ/12 | 9 | 12σ | λ/8 | | | |

* **FP**=footprint. Divergences are calculated for the bunch charge 0.02 nC

Full-scale simulations of wavefront propagation were carried out in the framework of Fourier optics, with software PHASE [13] and SRW [14].

Height error profiles similar to metrology data [15] were modelled using the formula

$$h(x) = \frac{1}{N_{sampl}} \sum_{j}^{N_{sampl}} a_j \sin(2\pi\, x / t_j - \varphi_j)$$

where $x$ is a coordinate at mirror surface along propagation direction, $N_{sampl}$ is the sampling rate, $a_j$ is a random amplitude of $j$-th spatial frequency $t_j$, in the range of [$\sigma_{min}$, $\sigma_{max}$], and $\varphi_j$ is a random phase. The one-dimensional power spectrum density (PSD) of modelled surfaces where similar to metrology data.

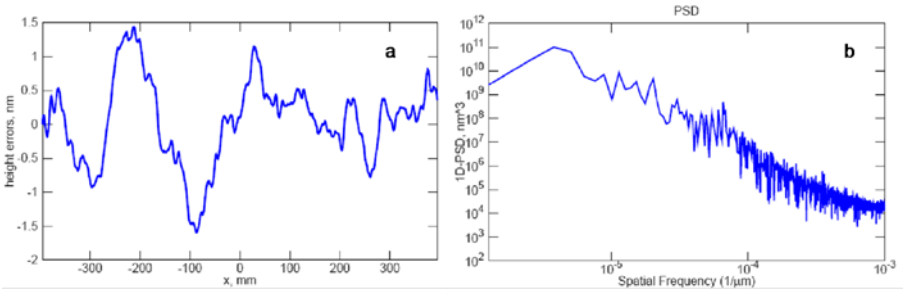


***Figure 75:*** *(a) One of the residual height error profiles for a 800 mm long mirror which were used in wave front propagation simulations. (b) One-dimensional power spectral density corresponding to the profile.*

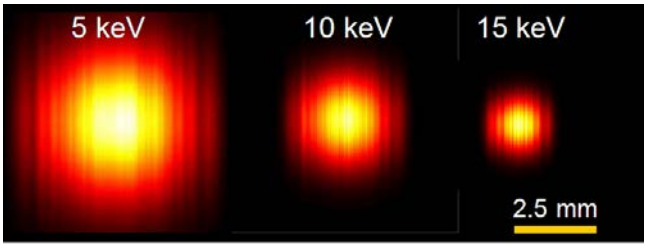


***Figure 76:*** *Wavefront propagation calculations for the centre beamlines of SASE1 and SASE2.The footprint on the 800 mm long mirrors is 4.5 σ and the assumed profile error is 2 nm PV.*

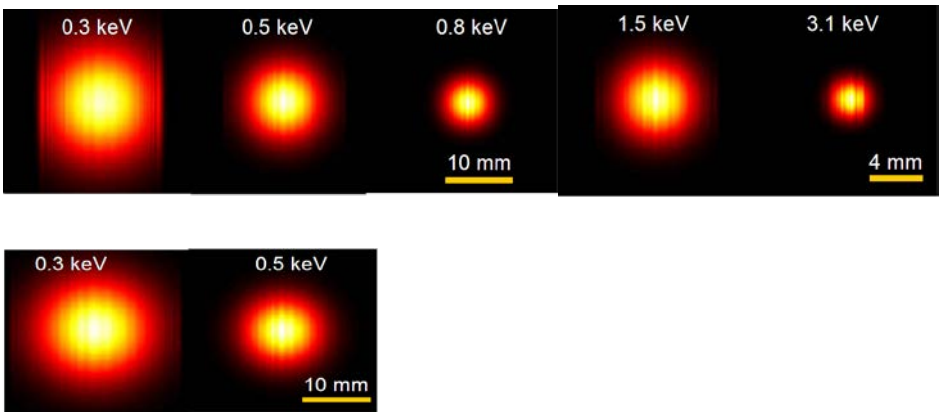


***Figure 77:*** *Wavefront propagation calculations for centre SQS beamline of SASE3. The assumed profile error is 3 nm PV.* Upper row: *The incidence angle on 800 mm long mirrors varies from 6 mrad for 1.5 and 3.1 keV, to 15 mrad for 0.3–0.8 keV photon energy.* Lower row: *Incidence angle is 20 mrad.*

## Conclusion

The mirror length of 800 mm is sufficient to optimize the offset mirror incidence angle for acceptable wavefront distortions for all beamlines. Wavefront simulations show that height errors should not exceed 2 nm PV for SASE1 and SASE2 (3–20 keV) and 3 nm PV for SASE3 (0.8–3 keV). Above 20 keV, the sensitivity increases. For longer wavelengths at SASE3, height errors of this magnitude become less relevant and they have only a minor impact on intensity distribution at experimental station. For SASE1 and SASE2 mirrors, the beam footprint should be ideally larger than 4.5 sigma. For SASE3, acceptable beam profiles can be achieved even down to 3.5 sigma footprint for energies lower than 0.5 keV. In this case a micro-focused beam would show small side maxima.

# 8 Concluding remarks

The conceptual design presented here relies on several novel X-ray optical components that are, in part, well beyond state of the art and have to be developed:

- Offset and distribution mirrors with 0.8 m length and a profile error of 2 nm PV, corresponding to about 20 nrad slope error. These mirrors have to be water-cooled and the bending has to be controlled to 10 nm accuracy or better.
- Gratings of 480 mm length with extremely small profile error.
- KB mirrors with 0.8 m length with extremely small profile error, bendable and water-cooled.
- Vibration-free, cryogenically cooled artificial channel-cut monochromators.

The first two items are maybe the most critical. If 800 mm long mirrors prove impossible to manufacture or control to this precision, the fallback solution would be the use of 500 mm long mirrors. The major loss in beamline performance would be the need for more often retuning of mirror angles when changing the energy. For the distribution mirrors, it would mean larger foci for the branch beamlines and less control over beam sizes. Very important remains, however, the need for a low-vibration reliable mechanics (see also Appendix D, “Vibrations”) that can position these mirrors and a control of the bending, preferably with some relative in-situ measurement capability.

If long gratings prove impossible to make, one could use 200 mm long gratings, which are currently commercially available from two vendors. This would reduce the resolution of the soft X-ray monochromator and the maximum pulse energy that can be transmitted.

For micro-focusing of hard X-rays, there are several options besides KB mirrors: CRLs, whose performance is being currently studied at LCLS and are likely to improve over the next years in material quality and available radii. Diamond-based zone plates were recently tested successfully at LCLS and gave close to 100 nm spot sizes. An R&D programme for diamond-based zone plates is currently being carried out by the KTH Stockholm as an in-kind contribution for the European XFEL. A combination of these optics could provide improved focusing capabilities in a two-step process.

A promising alternative to the monochromators presented here is the idea of seeding the FEL with a diamond monochromator inside the undulator [16]. Because the seeding happens early in the SASE process, intensities at the diamond crystal are only 1% of the intensities discussed here, however, on a smaller spot size. The beamlines would be fully compatible with such a seeding scheme, and even the monochromators would perform better, because most X-rays would be reflected instead of being absorbed in the first crystal. In such a scenario, the monochromators could be still useful for cleaning up the tails of the seeded FEL beam.

Also the after-burner concept that is currently under discussion for providing circularly polarized beams for SASE3 is compatible with the beam transport design. If the polarized light is generated as a second harmonic, part of the fundamental could be suppressed by the gas attenuator. In this way, the monochromator could be protected against the high pulse energies in the SASE fundamental and higher pulse energies for the polarized light become possible.

# A Damage calculations

An important question is, whether a particular X-ray optic can survive the high X-ray peak power during a single pulse [17]. A critical threshold for the occurrence of single shot damage is reached when the local energy density in the material exceeds the melting [18] [19] [20]. Above this threshold the material will ablate and, at sufficient higher energy densities, phenomena like plasma formation or non-thermal melting can occur. This situation is typically present in a micron-sized focus of the FEL beam. The peak energy concentration in all X-ray optics discussed here has to stay significantly below the melting threshold.

A rough estimate for the melting threshold $W_{melt}$ per atom can be obtained by

$$W_{melt} \approx 3k_B T_{melt}, \tag{20}$$

yielding for example 1 eV/atom for diamond, 0.7 eV/atom for $B_4C$ and 0.4 eV/atom for silicon. Since the heat capacity is here approximated in the high temperature limit and the initial thermal energy is neglected, these values can be considered as upper estimates. Also, the precise value might depend on photon energy, pulse duration, incidence angle, and sample morphology.

The volume, over which the pulse energy is initially distributed, is given by the footprint of the beam (beam cross section $b_{fwhm}$) on the optical element and the penetration depths perpendicular to the surface $d$:

$$W_{atom} = \frac{4\ln 2\ (1-R) W_{pulse}\, m\, \sin\theta}{\pi\, b_{fwhm}^2\, d\, \rho_m} \tag{21}$$

Equation (21) is normalized such that $W_{atom}$ describes the maximum energy per atom with mass $m$, corresponding to a spot in the center of a Gaussian beam.

The penetration depths *d* and the reflectivity *R* are given by

$$d = \frac{\lambda \varsigma}{4\pi\beta}, \tag{22}$$

$$R = \frac{\varsigma^2 \left(\sin\theta - \varsigma\right)^2 + \beta^2}{\varsigma^2 \left(\sin\theta + \varsigma\right)^2 + \beta^2} \tag{23}$$

with

$$\varsigma = \sqrt{0.5\left(\sin^2\theta - 2\delta + \sqrt{(\sin^2\theta - 2\delta)^2 + 4\beta^2}\right)} \tag{24}$$

and $\delta$ and $\beta$ are real and complex parts of the index of refraction *n*

$$n = 1 - \delta - i\beta$$

A plot of the $W_{atom}$ in Figure 78 shows that the relative dose per atom is a constant at high incidence angles, has a maximum at the critical angle, and reduces significantly at smaller angles. Above the critical angle, the variation in size of the beam footprint is compensated by the variation of the perpendicular penetration depth, which is in that case simply the photo absorption depth times the sine of the incidence angle. Below the critical angle, the penetration depth remains almost constant, so the increase of the footprint and the reflectivity lead to a sharp decrease of the dose at low angles. In this regime, an even further decrease of the dose was observed due to transport of energy through fast photo-electrons [19], which is however neglected in Equation (21).

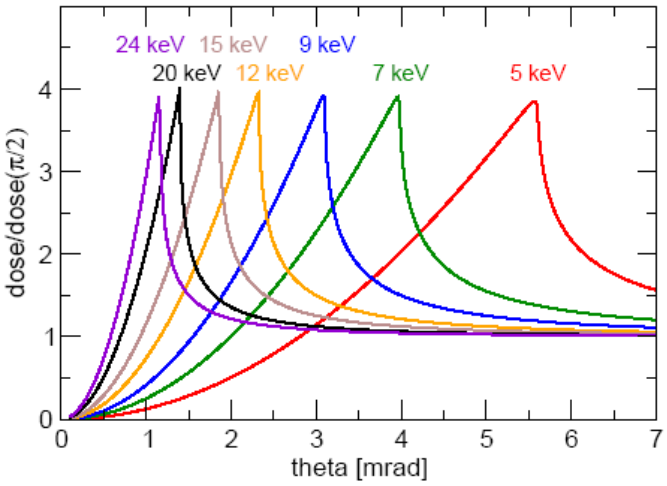


***Figure 78:*** *Dose per atom relative to normal incidence values versus incidence angle. Calculations were done for $B_4C$ coating.*

# B FEA on first offset mirror

The first mirrors in the beamlines are exposed not only to the FEL beam but also to the high-energy spontaneous (background) radiation. The background radiation is absorbed completely in the mirror substrate and therefore generates heat where it is absorbed. Thermal expansion of the heated volume introduces a bimetallic effect to the mirror substrate, since the backside of the mirror is colder than the front. Finite element analyses were conducted for the first mirrors in the SASE1 and SASE2 beamlines to investigate the thermal and structural behaviour of the substrate under background radiation.

Assumptions for the calculations are 17.5 GeV linac energy and 6.6 keV photon energy at fully closed undulator gap. The average power of the background radiation is assumed here to be 6.13 W behind the spontaneous radiation apertures, which is equal to the power absorbed in the substrate. In a first step, the averaged power is applied without time pattern to receive a heat profile and deformation for the “equilibrium state”. In the second step, the power is scaled and applied only during 0.3 ms at 10 Hz repetition, to simulate pulse trains of 1 350 pulses/train, which corresponds to the limitation from the electron dumps in this operation mode. Heat profiles and deformation of the substrate at the end of the pulse train are then compared to the average values.

Simulated was a 50 x 50 x 800 mm silicon substrate. The heating power is distributed to 64% within a thin layer covering the length of the mirror, 36% is applied to a half cylindrical volume around that layer to simulate heat generation by Compton radiation. The penetration depth of 160 µm was calculated by a Monte Carlo simulation code (Penelope). The cylindrical volume has a radius of 21.3 mm and stretches along the thin layer (see Figure 79).

The mirror is cooled from the top and bottom side. The cooling area on both sides is 10mm wide and stretches along the sides of the mirror at a distance of 5 mm from the reflecting surface. Cooling temperature is 295.15 K and the convection coefficient is 5 x $10^4$ W/$m^2$K. The heat load of the reflected FEL beam and radiation from the mirror to ambient have only a small influence on the thermodynamics and are neglected here for sake of simplicity of the model.

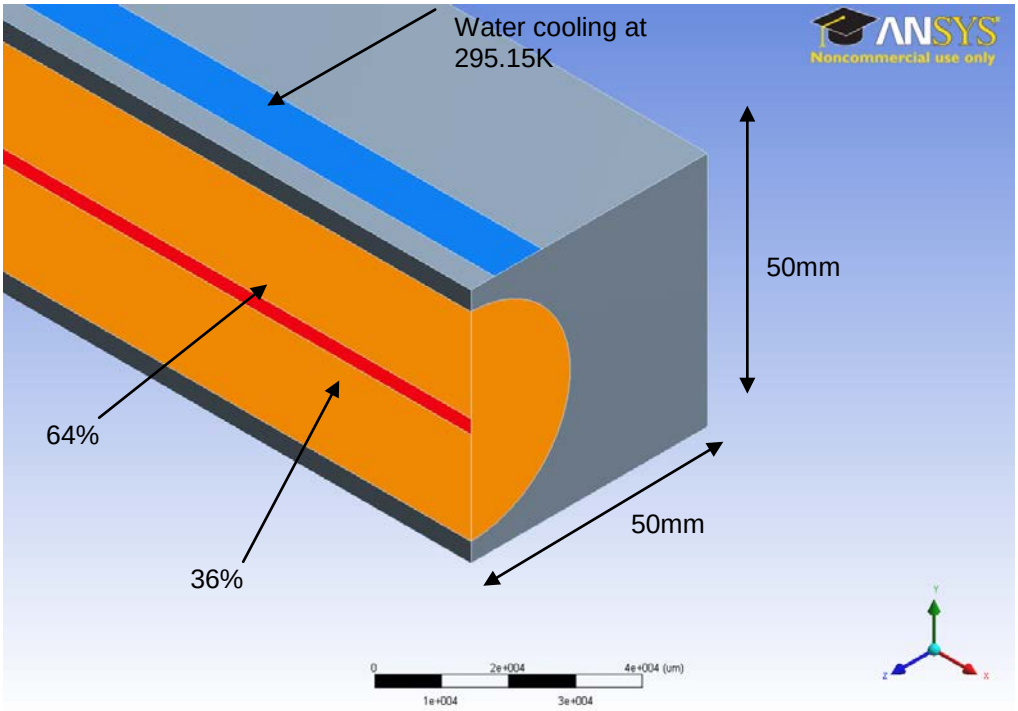


***Figure 79:*** *Three-dimensional heat deposition model*

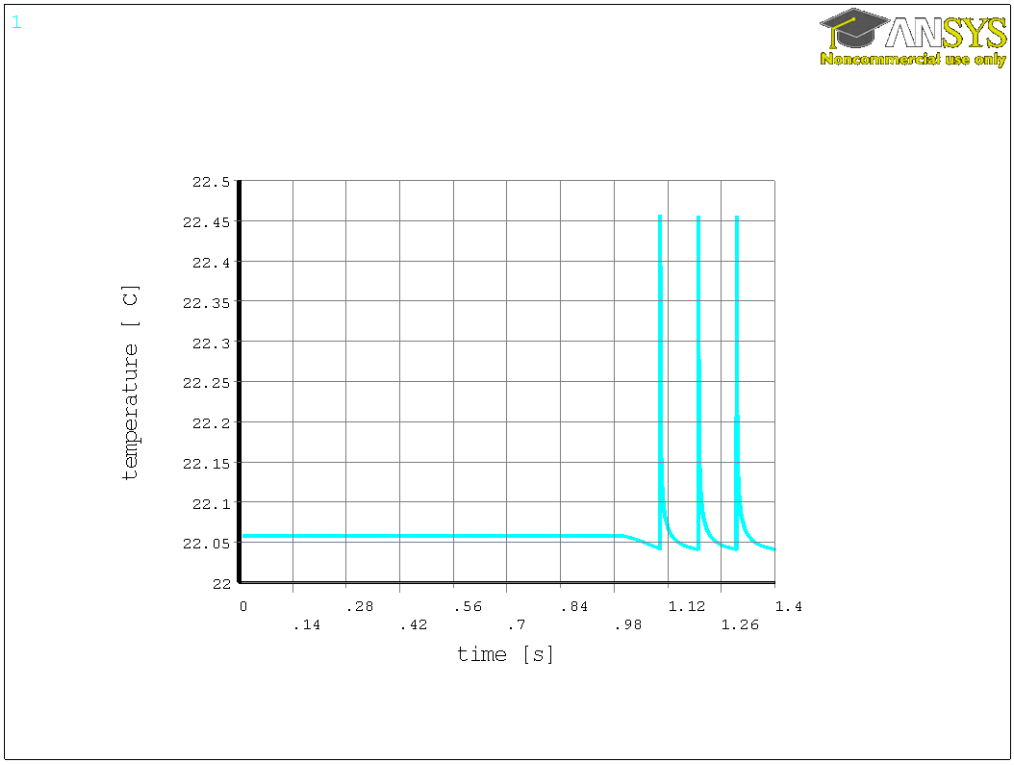


***Figure 80:*** *Time evolution of peak temperature. First, an average heat load is applied, then three pulse trains.*

The calculations show that, at the given energies, water cooling at room temperature is sufficient. The temperature on the mirror surface is only slightly above room temperature. Also, the results show that the implementation of an initial averaged heat load leads to temperature oscillations of the following three pulse trains around an equilibrium state. Regarding the pulsed heat load, the difference of < 0.5 K cannot be compensated by cooling at these temperatures.

For the structural simulation, an idealized mounting is used in order to obtain accurate numbers on the deformation due to the thermal effects. Gravity is also not included.

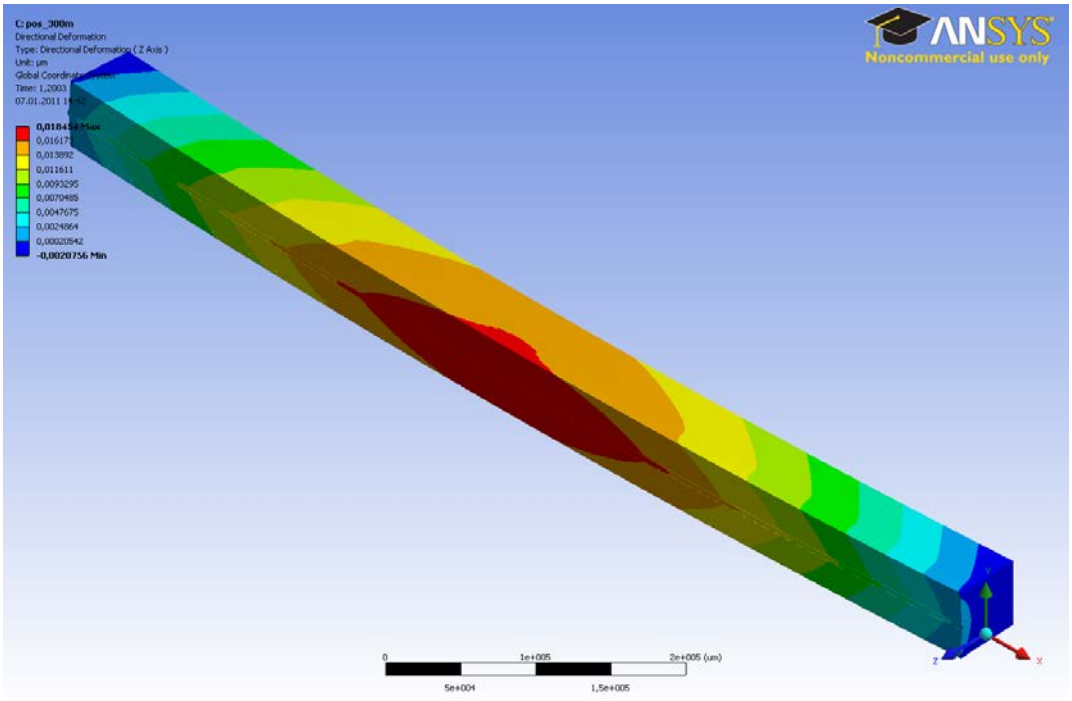


***Figure 81:*** *Deformation in the Z direction at the end of one pulse train. The maximum displacement in Z is 18.454 nm*

The most important figure for the structural analyses is the displacement of the reflecting surface in Z direction as it directly influences the direction and quality of the beam. The calculations show that the mirror surface deforms deformation is parabolic for the averaged heat load as well as for the pulsed heat load. Figure 81 shows the displacement of the material at the end of a pulse train. It appears that the deformation is decreasing from the volume with the largest heat deposition towards the rest of the substrate. This is due to the large amount of energy deposited in the small volume in very short time. The heat diffuses quite fast (see Figure 80) and the deformation profile becomes smoother. Note that the figure only shows the deformation in Z direction and does not reflect the expansion in length, which is much higher.

Figure 82 shows the deformation in the middle of the reflecting surface along the mirror. The difference between displacement for average heat load and after the pulse train is only 2.7 nm at the maximum.

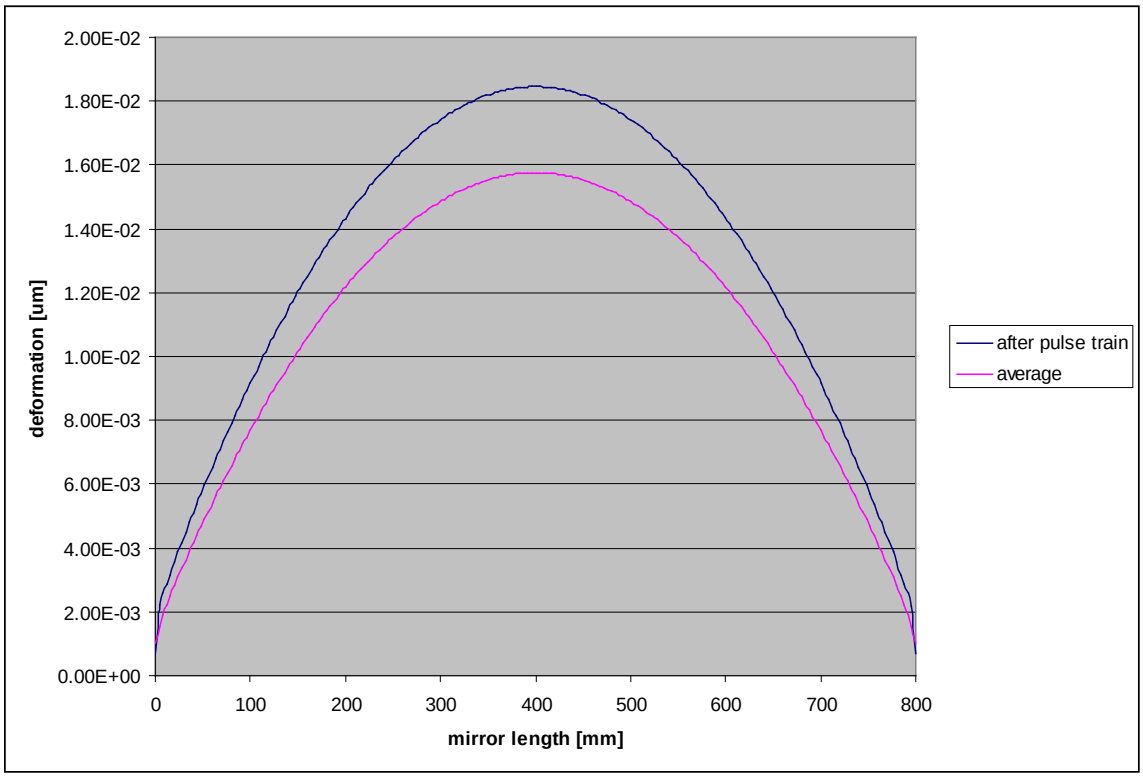


***Figure 82:*** *Comparison between average displacement and at the end of a pulse train. The maximum difference is 2.7 nm.*

Further investigation of the mirror behaviour should take into account a more realistic mounting and cooling, the influence of the FEL beam and thermal radiation from the mirror. Also fatigue effects between mirror coating and substrate should be investigated.

Simulations on different incidence angles, mirror geometries, and for other energies have also been conducted are documented in the following reports:

- *Simulation of different mirror positions for SASE1*
  http://edmsdirect.desy.de/edmsdirect/file.jsp?edmsid=1981121
- *Comparison of symmetric and single-side cooling*
  http://edmsdirect.desy.de/edmsdirect/file.jsp?edmsid=1964541
- *Mirror cooling and geometry for SASE3*
  http://edmsdirect.desy.de/edmsdirect/file.jsp?edmsid=2029231

# C Suppression of higher harmonics

The pulse energy of higher harmonics compared to the fundamental is about 1% for the third harmonic and 0.03% for the fifth harmonic [4]. However, the higher harmonic content can become very disturbing, for example, as background in a crystallography experiment or when the fundamental is strongly attenuated.

One benefit of the adjustable offset mirrors in the presented conceptual design is that the incidence angles can be optimized to suppress the higher harmonics. In fact, for the hard X-ray beamlines, the tunability $E_{max}/E_{min}$ is less than 3 (see Table 2 and Table 6 on page 19), therefore the third harmonic is suppressed in a typical beamline setting. An optimized attenuation can be achieved by aligning the offset mirrors to the critical angle for a particular energy. This can be achieved for $E_{photon}$ > 7.5 keV for SASE1 and SASE2 and $E_{photon}$ > 1 keV for the SASE3. The reflectivity curve for one mirror is shown in Figure 83.

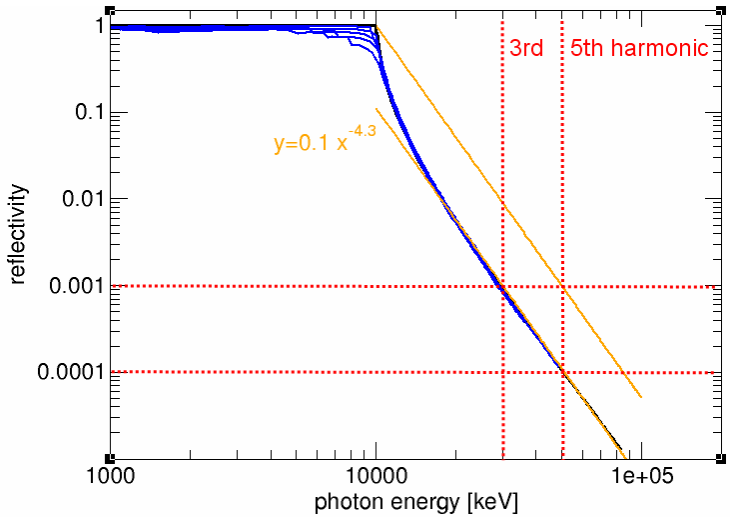


***Figure 83:*** *Suppression of higher harmonics by a single mirror. The blue and black curves represent calculated reflectivity curves with B4C and Pt coating with critical energies between 6 and 80 keV. All curves were scaled in this figure to the critical energy of 10 keV. The suppression of the third harmonic is the $10^{-3}$ and of the fifth harmonic $10^{-4}$.*

The maximum achievable suppression by two offset mirror is therefore $10^{-6}$ for the third harmonic.

# D Vibrations

Crucial to the conceptual design are offset and distribution mirrors positioned up to 700 m before the experiment hall. The pointing stability of these mirrors is a concern: For example, vibration amplitudes of 1 µrad rms would lead to beam motions in the experimental hall of 2.8 mm—the full beam size for 8 keV at SASE2. On the other hand, a monochromator crystal close to the experiment vibrating with the same angular amplitude would have less impact on the beam position at the experiment, but the apparent source position for subsequent optics would vibrate with 2.8 mm PV and strongly effect the positional stability of the focus for example of a KB micro-focusing system.

In this appendix, a simple analytical method is introduced to compare vibration effects for optical elements at different positions in a beamline.

## Ground vibration spectrum

Vibration measurement at site of the European XFEL were conducted by the DESY vibration group before the start of the construction and are shown in Figure 84 and the derived displacement in nm in Figure 85. The average rms displacement >1 Hz was measured to be 38.7 nm, which is an average value among other facilities: ESRF: 71.6 nm, APS: 10.5 nm, BNL: 87.8 nm, LCLS: 4.8 nm, and Spring8: 2nm [21]. The noise > 1 Hz stems from cultural noise and falls off for high frequencies ~ $1/f^4$. Angular vibrations can be estimated as 4 nrad rms for >1Hz [22].

Since the radiation is delivered at the European XFEL in pulse trains, it is sampling the vibrations at the following frequencies: < 1 Hz to 5 Hz, 10 Hz, 1.6 kHz to 4.5 MHz, 10–1 000 THz. Because of the $1/f^4$ dependence, displacements and angular vibrations at 1 kHz will be eight orders of magnitude smaller than at 10 Hz and therefore well below the 1 nm, 1 nrad scale of the X-ray optics. An immediate consequence is that ground vibrations are irrelevant for pulse trains. The beamline appears frozen during the

maximum 600 µs of the pulse train. However, by the time the next pulse train arrives, all beamline components will experience ground vibrations corresponding to the 10 Hz maximum in Figure 84.

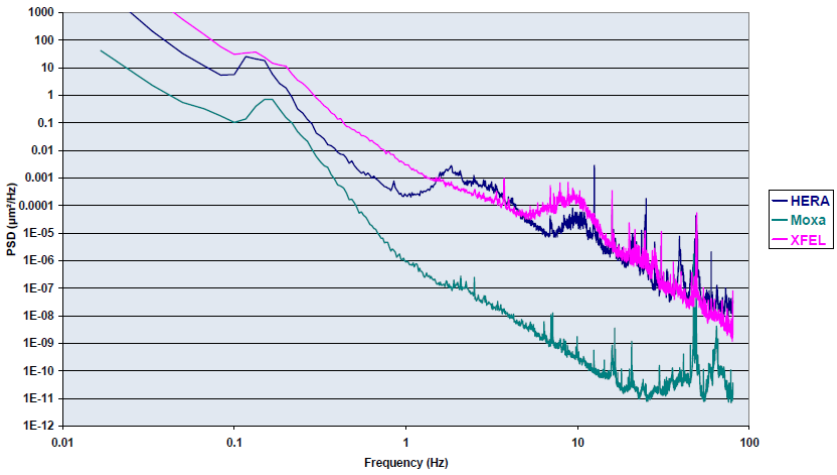


***Figure 84:*** *Power spectral density of vertical ground motion at the XFEL site and in the HERA tunnel at DESY. The green curve shows as a reference an extremely quiet location [23].*

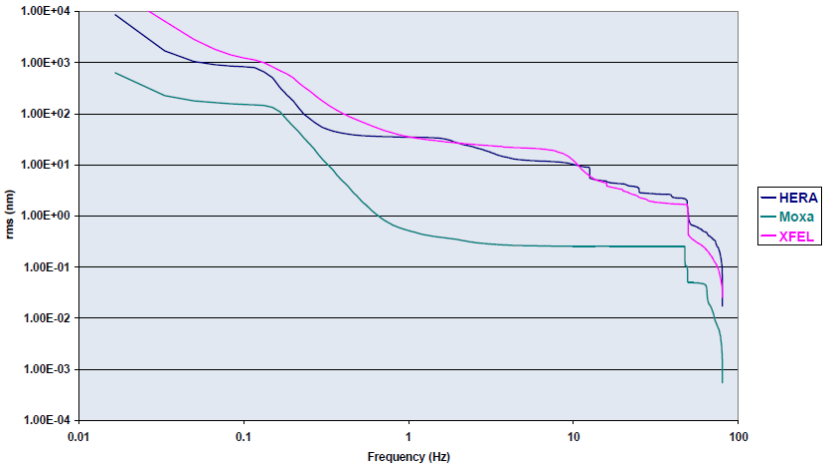


***Figure 85:*** *Integrated power spectral density versus cut frequency at f > 1Hz [23]*

## Beamline vibrations

Beamline vibrations will be visible on the < 10 Hz frequency scale. To quantify the amount of vibration that each component contributes, we assume here an idealized nano-focusing setup at the end of the branch beamline of SASE1 that will reach a geometrically limited spot size 1 m after the optics. Only

horizontal vibrations in angle and position will be considered. A schematic view is shown in Figure 86.

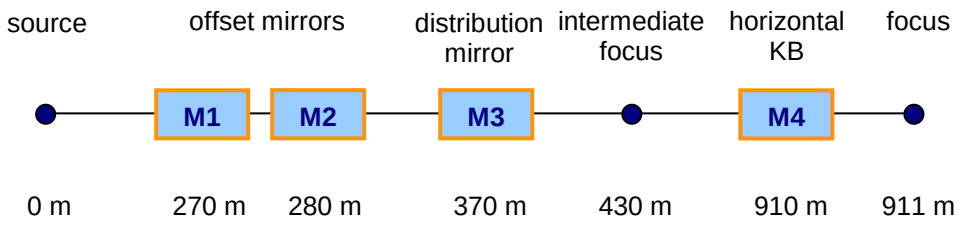


***Figure 86:*** *Schematics of setup for vibration analysis*

For the vibration analysis, after each optical element a real or virtual source is calculated that combines all vibrational motions of the previous elements in translational motions of the new source. A generic optical element with the relevant motions is shown schematically in Figure 87.

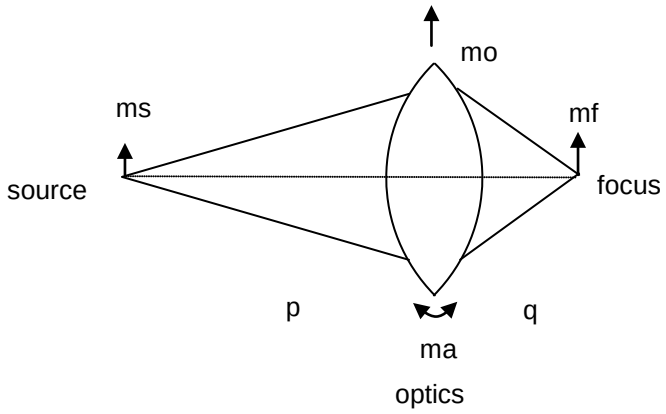


***Figure 87****: Generic optical element with motion of source, optics, and image*

For a defocusing or flat mirror, *q* would become negative.

A translation of the source $m_s$ causes a translation of the focus $m_f$:

$$m_f = -\frac{q}{p} m_s$$

For mirrors one can show that a lateral translation of the optics leads to:

$$m_f = \left(1 - \frac{q}{p}\right) m_o$$

And finally, for angular motions of a mirror:

$$m_f = 2qm_a$$

The total motion of source can be then added by the sum of the squares:

$$m_f = \sqrt{\left(\frac{q}{p} m_s\right)^2 + \left(\frac{p-q}{p} m_o\right)^2 + (2qm_a)^2}$$

For the following optical element, $m_f$ of the previous element is used as $m_s$ and the same analysis is repeated. In this approach the source is thought to radiate in all directions; therefore, a change of the propagation direction by vibrational motion does not occur.

It is now assumed that at each optical element experiences a lateral vibration of 100 nm rms and an angular vibration of 10 nrad rms.

**Example 1:** Vibration analysis of SASE 1 branch beamline with flat offset and distribution mirrors.

$m_o$ = 100 nm (assumed ground vibration at the optics for 10 Hz)

$m_a$ = 10 nrad

$m_{s0}$ = 0 (no source point fluctuation from electron beam)

M1: $p$ = 270 m, $q$ = -270m

M2: $p$ = 280 m, $q$ = -280m

M3: $p$ = 370 m, $q$ = -370m

M4: $p$ = 910 m, $q$ = 1 m

$$m_{f1} = \sqrt{(m_{s0})^2 + (2 \times 100nm)^2 + (2 \times 270 \times 10nrad)^2} = 5.40 \mu m$$

With the first three mirrors considered:

$$m_{f3} = \sqrt{3(2\times 100nm)^2 + (2\times 270\times 10nrad)^2 + (2\times 280\times 10nrad)^2 + (2\times 370\times 10nrad)^2} = 10.74\,\mu m$$

and including the last KB mirror:

$$m_{f4} = \sqrt{\left(\frac{1}{910}10.74\mu m\right)^2 + \left(\frac{909}{910}0.1\mu m\right)^2 + (2\times 1m\times 10nrad)^2} = 103nm$$

Note, that this motion of the focus is entirely dominated by the translational vibration of the horizontal KB mirror of 100 nm. However, by putting the KB optics and the sample on the same stiff support, one could couple these two motions, so that only the relative motion and the motion of the upstream source would matter. If this is also true for the angular vibrations of the last mirror, then only half of this angular vibration would be visible at the sample location.

In an ideal stiff KB+sample setup one would get therefore:

$$m_{f4} = \sqrt{\left(\frac{1}{910}10.74\mu m\right)^2 + (1m\times 10\,nrad)^2} = 15.4\,nm$$

The motion of the focus point depends in this case mostly on the angular vibrations of the mirrors and their distances to the source or focus. This rms value has to be compared to the size of the diffraction limited focus after the KB mirror in the range of 50–100 nm FWHM.

**Example 2:** Vibration analysis for SASE 1 beamline with intermediate focus

For the low photon energies, the second offset mirror has to focus onto the distribution mirror because the incidence angle of the distribution mirror cannot be adjusted like the offset mirrors.

It is then

M1: p = 270 m, q = -270 m

M2: $p$ = 28 m, $q$ = 150 m (focusing)

M3: $p$ = -60 m, $q$ = 60 m (flat)

M4: $p$ = 480 m, $q$ = 1 m

$$m_{f1} = \sqrt{(2\times 100\,nm)^2 + (2\times 270\times 10\,nrad)^2} = 5.40\,\mu m$$

$$m_{f2} = \sqrt{\left(\frac{150}{280}5.40\mu m\right)^2 + \left(\frac{280-150}{280}0.1\mu m\right)^2 + (2\times 150\times 10\,nrad)^2} = 4.16\mu m$$

$$m_{f3} = \sqrt{(4.16\mu m)^2 + (2\times 0.1\mu m)^2 + (2\times 60m\times 10nrad)^2} = 4.33\mu m$$

$$m_{f4} = \sqrt{\left(\frac{1}{480}4.33\mu m\right)^2 + (1\times 1m\times 10nrad)^2} = 13.4\,nm$$

The individual contributions from each element motion can be separated by setting in the above equations all other motions to zero. The total vibration amplitude at the location of the nano-focus adds then up as the sum of the squares of individual contribution. The breakdown into single contributions for the two examples above is shown in Table 21.

***Table 21:*** *Breakdown of total vibrational motion at SASE1 branch beamline into individual components*

| **Element, position** | | **M1 270 m** | **M2 280 m** | **M3 370 m** | **M4 910 m** | **Total 911 m** |
|---|---|---|---|---|---|---|
| Example 1 flat mirrors | Angular | 5.93 nm | 6.15 nm | 8.13 nm | 10 nm | 15.4 nm |
| | Translational | 0.2 nm | 0.2 nm | 0.2 nm | 0 (stiff mount) | |
| Example 2 intermediate focus | Angular | 6.02 nm | 6.25 nm | 2.5 nm | 10 nm | 13.4 nm |
| | Translational | 0.22 nm | 0.4nm | 0.4 nm | 0 (stiff mount) | |

In example 2, the sensitivity to angular motions of the distribution mirror M3 decreases, because it is closer to the source than in Example 1. The validity of the presented approach was also cross-checked for selected cases with the beamline simulation software Shadow.

## Conclusion

The angular vibrations are far more critical than translational vibrations, which could be a factor of 10 higher in this example (1µm rms) before they reach the impact level of the assumed 10 nrad angular vibrations. For angular vibrations, 10 nrad seems to start impacting the focus quality; however, profile errors of mirrors were neglected in this consideration. The 2 nm PV profile error specification demanded from wavefront optics corresponds to about 20 nrad slope error on the relevant length scales. There will be a “smearing” of the beam on this level; therefore, we think a specification of 20 nrad rms angular vibration level for the mirrors compared to the ground is a reasonable R&D goal for the design of the mirror chambers.

Correlated vibrations were only assumed in the experimental area so far. However, a correlated motion for example of two channel-cut crystals together will *not* introduce vibrations of the apparent source position. A similar argument could be made for a double mirror system: With a speed of sound in the floor around the double mirror system of around 1500 m/s, a 10 Hz seismic wave would have 150 m wavelength. If mirrors are positioned less than λ/4 close together, they start vibrating in phase and the impact of

vibrations would reduce (provided the chambers have both the same transfer functions). Therefore, a reduction of the minimum offset at the offset mirrors as suggested in the “Bremsstrahlung collimator” section of Chapter 6, “Beamline components”, would allow positioning them closer together and therefore reducing vibrations. For monochromators, the use of channel-cuts or artificial channel-cut will produce better vibration levels than two crystals on individual mounts.

Apart from seismic vibrations, which have a natural cut-off above 100 Hz, another source of vibrations could be the excitation of eigenfrequencies of the optics by the beam or external acoustical noise. Eigenfrequencies of mirror substrates and silicon crystals range from 5 kHz to several 100 kHz and should be considered in the design of these components.

One important result of this section is that seismic vibrations are not relevant on time scales of one pulse train, but will be only visible for frequencies <10 Hz. These time scales start to overlap with consideration of long term drifts discussed in Appendix E, “Ground diffusion effects”.

# E Ground diffusion effects

In this appendix, the expected stability of beamline components with respect to the beam is estimated from the so-called “ATL law”. Criteria for the initial survey and alignment accuracy of X-ray components can be inferred from the expected motion from within one week to one year.

The ATL law is used to describe “space-time ground diffusion” of accelerators empirically over long distances:

$\sigma^2 = A\ T\ L$

where $A$ is a constant, $T$ the time, and $L$ the considered length. Empirical values for $A$ are $10^{-17}$ m/sec for noisy ground, $A = 10^{-19}$ m/sec for quite ground, and $A = 4\text{ -}20 \times 10^{-18}$ m/sec measured at HERA.

For a 1 km long beamline, one would expect with e.g. $A = 2 \times 10^{-17}$:

σ = 42 µm/day  110 µm /week  0.8 mm/year.

This diffusion rate coincides roughly with value estimated for the annual tunnel deformation and motion due to changes in ground water level (0.8 mm horizontal and 0.4 mm vertical deformation, 1 mm change of centre position). In the following, we will therefore use the **$A = 2 \times 10^{-17}$ m/sec**; however, one can keep in mind that under quiet conditions, σ could be a factor of 10 lower.

As an example, the schematic layout of the SASE1 beamline is given below:

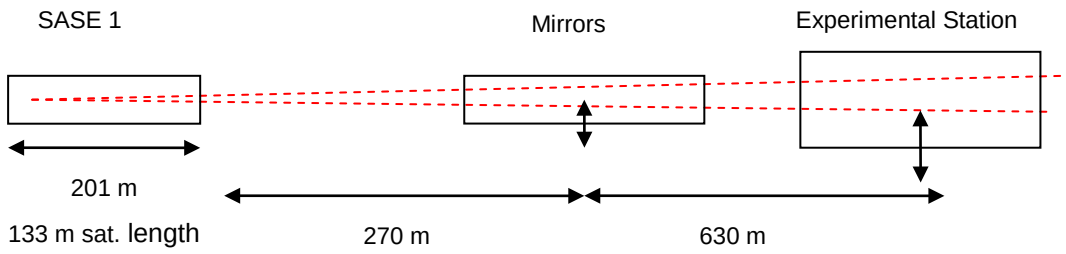


First, the beam stability at the exit of the undulator is estimated. If one assumes the 133 m long lasing part of the undulator drifts as one unit, one gets for the beam motion at the end of the undulator:

Translation: σ = 7.6 µm/ day 20 µm/ week 0.14 mm/ year

Angle: σ' = 0.11 µrad/ day 0.3 µrad/ week 2.2 µrad/ year

Along the beamline one has to consider two motions: The motion of beamline components with the tunnel diffusion and the beam motion, which originates in the ground diffusion of the undulator region. A measure for the requirements for the initial survey is the combined annual drift. At different distances along the beamline one gets:

***Table 22:*** *Expected ground diffusion at SASE1 beamline*

| | **0 m undulator end** | **270 m first mirrors** | **370 m distribution mirror** | **900 m station** |
|---|---|---|---|---|
| Ground diffusion d/w/y [µm] | 0/ 0/ 0 | 22/ 57/ 412 | 25/ 67/ 482 | 40/ 104/ 753 |
| Beam motion d/w/y [µm] | 7.6/ 20/ 144 | 34/92/660 | 42/112/812 | 103/271/1963 |
| Ground + beam motion [µm] | 7.6/ 20/ 144 | 40/ 108/ 910 | 49/ 130/ 944 | 110/ 290/ 2102 |

**Conclusion**: At the end of the photon beamlines, the theoretical beam through the undulator axis will likely move on the scale of mm per year with respect to the buildings. The dominating contribution is the angular motion of the undulators; however, ground diffusions of the photon tunnels are of a similar magnitude. Therefore, a permanent monitoring of ground diffusions just in the photon tunnels would not be enough to predict the apparent beam motions. Instead, a system of X-ray beam position monitors (XBPMs) in slow feedback loops should be used to keep the beamline optics system aligned. A beam motion of more than 100 µm per day in the experiment hall is not acceptable for most experiments. Therefore, an XBPM should be installed at the beginning of each experiment on the floor of the experiment hall. The beam will be steered by motions of mirrors or monochromator crystals to always the same position on the XBPM.

Since the drift goes with the square root of time, one can extrapolate the expected drift of 100 µm/day to 100 nm / 0.1 s in between pulse trains. It should be noted that the initial assumption of the constant *A* corresponds to a “noisy ground” and could be lower in reality.

# F Abbreviations and acronyms

| | |
|---|---|
| **ATL-law** | Empirical relation describing long-term ground motion. |
| **BS** | bremsstrahlung |
| **C monochromator** | Monochromator operating with diamond single crystals. |
| **CRL** | compound refractive lens. Can be used similar like an optical lens to focus or collimate X-rays. Chromatic focusing device. |
| **eV** | electron volts. |
| **FWHM** | full width at half maximum = 2.354 σ |
| **FEA** | Finite Element Analysis |
| **FEE** | front-end enclosure. Hutch with beam transport system at LCLS. |
| **FEL** | free-electron laser |
| **FXE** | Femtosecond X-ray Experiments scientific instrument |
| **GeV** | Giga electron volts. Used as unit for accelerator energy |
| **HED** | High Energy Density matter scientific instrument |
| **I0 monitor** | Intensity monitor |
| **KB mirrors** | Kirkpatrick-Baez focusing scheme with two perpendicular focusing mirrors. Achromatic. |
| **keV** | kilo-electron-volts. Used as unit for photon energy. |
| **K monochromator** | Monochromator to analyse spontaneous radiation from one or more undulator modules. |
| **LCLS** | X-ray laser facility at SLAC, USA. |
| **MCP** | multi-channel plate |
| **MID** | Materials Imaging and Dynamics scientific experiment. |
| **nC** | nano-Coulomb. Used as unit for electron bunch charge. |
| **pC** | pico-Coulomb. Used as unit for electron bunch charge. |
| **PES** | photo-electron spectrometer |
| **PGM** | plain grating monochromator |
| **PSD** | position sensitive detector |
| **RP** | resolving power of soft X-ray mono |
| **SASE** | self-amplified spontaneous emission. Process of generating X-ray laser radiation in undulators. |
| **SASE1,2,3** | Photon beam transport systems behind the corresponding undulators. |

| | |
|---|---|
| **SCS** | Spectroscopy and Coherent Scattering scientific instrument |
| **Si monochromator** | Monochromator operating with silicon single crystals. |
| **SPB** | Single Particles, Clusters, and Biomolecules scientific instrument. |
| **SQS** | Small Quantum Systems scientific instrument. |
| **SR** | Spontaneous radiation (corresponds to synchrotron radiation at storage rings). |
| **SRA** | Spontaneous radiation aperture (corresponds to white beam slit at storage rings) |
| **ST0 station** | Small diagnostics station in the LCLS undulator hall. |
| **sigma, σ** | Gaussian distribution parameter of photon beam size. |
| **VLS grating** | variable line spacing grating |
| **XBPM** | Gas-based X-ray beam position monitor. |
| **XGMD** | Gas-based X-ray intensity monitor. |
| **XHEP** | Experiment hall. |
| **XTD2, XTD1, XTD4** | Undulator tunnels for SASE1, SASE2, and SASE3 |
| **XS3, XS1** | Shaft buildings for SASE1 and SASE2 |
| **XTD9, XTD6, XTD10** | photon tunnels SASE1, SASE2, and SASE3 |

# G References


[1] Th. Tschentscher: “Layout of the X-ray Systems of the European XFEL”, in preparation (2011)

[2] M. Yurkov et al.: “Calculations of SASE beam parameters with FAST code” (February 2011)

[3] P. Emma et al.: Nature Photonics, DIO:10:1038/NPHOTON.2010.176 (2010)

[4] M. Altarelli et al. (ed.): “The European X-ray free-electron laser Technical Design Report”, DESY 2006-091 (2006)

[5] H. Sinn, S. Dastjani-Farahani, I. Freijo-Martin, G. Galasso, J. Gaudin, L. Samoylova, A. Trapp, F. Yang: “Design of photon beamlines at the European XFEL”, FEL2010 proceedings, THOCI1 (2010) http://srv-fel-0.maxlab.lu.se/TOC/THOCI1.PDF

[6] R. Reininger, R. de Castro: Nucl. Instr. Meth., A 538, 760 (2005)

[7] H. Sinn: “Heat load estimates for XFEL beamline optics”, HASYLAB Annual Report 2007

[8] P. Elleaume: Nucl. Instrum. and Meth in Phys. Research A, 412 (1998) 483–506

[9] A. Snigirev, V. Kohn, I. Snigireva, A. Souvorov, B. Lengeler: “Focusing High Energy X-rays by Compound Refractive Lenses”, Applied Optics, 37 (1998) 653–662

[10] Lengeler et al.: “Imaging by parabolic refractive lenses in the hard X-ray range”. J Synchrotron Radiat, 6 (1999) 1153–1167

[11] G. Geloni, E. Saldin, L. Samoylova, E. Schneidmiller, H. Sinn, Th. Tschentscher, M. Yurkov: “Coherence properties of the European XFEL”, New J. Phys., 12 (2010)

[12] M. Born, E. Wolf: *Principles of Optics*, 6th edition, Pergamon Press, Oxford (1980)

[13] J. Bahrdt: “Wavefront tracking within the stationary phase approximation”, Physical Review Special Topics, 10 (2007) 060701(15)

[14] O. Chubar, P. Elleaume: Proceedings of EPAC-98 (1998), 1177

[15] L. Samoylova et al.: Proc. SPIE, 7360 (2009) 7360–11

[16] G. Geloni, V. Kocharyan, E. Saldin: “A simple method for controlling the line width of SASE X-ray FELs”, Red Report (2010), DESY 10-053 http://arxiv.org/abs/1004.4067

[17] This section is an excerpt from reference [5], except that the error in equation (24) was corrected.

[18] S.P. Hau-Riege, R.A. London, A. Graf, S.L. Baker, R. Soufli, R. Sobierajski, T. Burian, J. Chalupsky, L. Juha, J. Gaudin, J. Krzywinski, S. Moeller, M. Messerschmidt, J. Bozek, C. Bostedt: "Interaction of short x-ray pulses with low-Z x-ray optics materials at the LCLS free-electron laser", Opt. Express 18 (2010) 23, 23933

[19] J. Chalupsky, V. Hajkova, V. Altapova, T. Burian, A.J. Gleeson, L. Juha, M. Jurek, H. Sinn, M. Stormer, R. Sobierajski, K. Tiedtke, S. Toleikis, T. Tschentscher, L. Vysin, H. Wabnitz, J. Gaudin: "Damage of amorphous carbon induced by soft x-ray femtosecond pulses above and below the critical angle", Appl. Phys. Lett. 95 (2009) 3, 031111

[20] Sh. Dastjani Farahani, H. Sinn, T. Tschentscher, J. Gaudin, J. Chalupsky, T. Burian, V. Hajkoya, L. Juha, A.J. Gleeson, M. Störmer, R. Sobierajski, M. Jurek, D. Klinger, K. Tiedtke, S.Toleikis, H. Wabnitz, H. Chapman: "Damage threshold of amorphous carbon mirror for 177 eV FEL radiation", NIMA in press (2011)

[21] W. Bialowons, R. Amirikas, A. Bertolini, D. Kruecker: "Measurement of Ground Motion in Various Sites", EUROTeV Report 2006-033 http://vibration.desy.de/documents/papers/

[22] W. Bialowons, private communications, 2010

[23] Figures were obtained from http://vibration.desy.de

# Acknowledgements

This report was written by Harald Sinn, Jérôme Gaudin, Liubov Samoylova, Antje Trapp, and Germano Galasso, with contributions from Fan Yang, Nicole Kohlstrunk, Martin Dommach, Idoia Freijo, Shafagh Dastjani Farahani, Vladimir Bushuev, Mark Khenkin, and Jan Grünert.

We would like to thank the members of the Beamline Advisory and Review Team for careful evaluation of the CDR document and constructive input during the review: Christian Schroer, Edgar Weckert, John Arthur, Rolf Follath, Timm Weitkamp, Aymeric Robert, Horst Schulte-Schrepping, and Ray Barrett. We would also like to thank the following people for fruitful discussions and contributing ideas: Frank Siewert, Johannes Bahrdt, Oleg Choubar, Riccardo Signorato, Tino Noll, Franceso Sette, Jacek Krzywisnky, Michael Rowen, Jim Welch, Alke Meents, Wilhelm Bialowons, Hermann Franz, Jerry Hastings, Thomas Tschentscher, and all colleagues from European XFEL involved in the conceptual design review process and numerous discussions related to it. Many thanks to Kurt Ament for providing the document template and for proofreading the manuscript.